DnaB and DciA: Mechanisms of Helicase Loading and Translocation on ssDNA

*°[1,2]Nicholas Gao, *[4]Daniele Mazzoletti, [1]Adele Peng, [5]Paul Dominic B. Olinares, §[4]Castrese Morrone, ^[4]Andrea Garavaglia, [1]Nourelhoda Gouda, [1]Serge Tsoy, [1]Albert Mendoza, [1]Ahammad Chowdhury, [1,4]Antonio Cerullo, [1]Hrutvik Bhavsar, [4]Franca Rossi, [4]Menico Rizzi, [5]Brian T, Chait, #[4]Riccardo Miggiano, and #[1,2,3,4]David Jeruzalmi

[1]Department of Chemistry and Biochemistry, City College of New York, New York, NY 10031, USA.

Ph.D. Programs in Biochemistry[2], Biology[3], and Chemistry[4], The Graduate Center of the City University of New York, New York, NY 10016, USA.

[4]Department of Pharmaceutical Sciences, University of Piemonte Orientale, Novara, 28100, Italy

[5]Laboratory for Mass Spectrometry and Gaseous Ion Chemistry, The Rockefeller University, New York, New York 10065, USA

#For correspondence: dj@ccny.cuny.edu or riccardo.miggiano@uniupo.it

*These authors contributed equally.

°Present address: Mirimus Inc, 760 Parkside Ave, Brooklyn, NY 11226, USA

§Present address: Telethon Institute of Genetics and Medicine (TIGEM) Via Campi Flegrei, 34 80078 Pozzuoli (NA) Italy.

^Present address: Department of Pharmaceutical Science (DISFARM), University of Milan, Milan, 20133 Italy

Abstract

Replicative helicases are assembled on chromosomes by helicase loaders before initiation of DNA replication. Here, we investigate mechanisms used by the bacterial DnaB replicative helicase and the DciA helicase loader. In the present structure of the DnaB-ssDNA•ATPγS complex, the amino-terminal (NTD) tier, previously found as an open spiral in a GDP•AlF_4 complex, was observed to adopt a closed planar arrangement. Further, the DnaB subunit at the top of the carboxy-terminal spiral (CTD) tier is displaced by ~25 Å between the two forms. We suggest that remodeling the NTD layer between closed planar and open spiral configurations and migration of two distinct CTDs to the top of the DnaB spiral, which is repeated three times, mediates hand-over-hand translocation. Although DciA loaders from *Vibrio cholerae* and *Mycobacterium tuberculosis* feature an inverted domain arrangement, they use Lasso domains to contact DnaB near the Docking-Linker-Helix interface. Up to three copies of Vc-DciA bind to Vc-DnaB and suppress its ATPase activity during loading onto physiological DNA substrates. Our data suggest that DciA loads DnaB onto DNA using the ring-opening mechanism.

Introduction

Replisomes in all domains of life rely on replicative helicases to melt chromosomal DNA into single-stranded templates for DNA replication[1–6]. Replicative helicases feature a toroidal ensemble comprised of six protein subunits and a topologically closed central chamber into which the active entity admits one strand of DNA while the second strand is excluded. DnaB leverages the energy of ATP binding and hydrolysis to translocate along single-stranded DNA (ssDNA) in its central chamber. Assembly of DnaB on ssDNA requires distinct mechanisms and factors (Figure 1).

In bacteria, replicative helicases are members of the DnaB family[7–20] (henceforth: DnaB). The physiological assembly (reviewed in[21–27]) presents as a homohexamer, with two tiers (termed the amino-terminal domain (NTD) and the carboxy-terminal domain (CTD)) that each circumscribes a central channel through which ssDNA will traverse. A short linker helix (LH) element connects each NTD and CTD; the LH packs against a neighboring CTD's docking helix (DH) in the complete hexamer. The finding that the translocating form of DnaB adopts a right-handed spiral configuration implied a hand-over-hand mechanism to explain translocation on ssDNA. Translocation occurs akin to how a human uses two hands to climb a rope, except that DnaB has six hands. Translocation initiates via ATP hydrolysis on a DnaB subunit at the bottom of the spiral (in the pose in Figure 2). This subunit peels away from its partner and from ssDNA[10,24,28,29], migrates to the top of the spiral, docks onto a DnaB subunit via its β-hairpin arginine finger, and binds ssDNA position 3' from the original location, further translocation occurs via progressive subunit migrations to the top of the DnaB

spiral[10]. Crucial support for the hand-over-hand model emerged from a series of structures of the DnaB-family helicase Gp4 from T4[24,29].

Studies utilizing bacteria and phage have uncovered several helicase loaders and their interactions with the cognate DnaB helicase. These include *Escherichia coli* (*E. coli)* DnaC[30], bacteriophage λP[31], bacteriophage SPP1 G39P[32,33], *Bacillus subtilis* DnaI[34], T4 gene 59[35], and phage P2 B[36]. Surprisingly, the genomes of most bacteria lack orthologs of these well-studied loaders. Instead, most bacteria employ members of the structurally, and perhaps mechanistically, distinct DciA or DopE families[37–41]. Although the amino acid sequences of bacterial helicase loaders diverge significantly, they appear to mediate conserved mechanisms during helicase loading[11,12,14,16,19,36,42–48]. Loaders display a conserved overall architecture: a globular domain adjacent to an intrinsically disordered segment that often features an alpha helix at a terminus, termed the Lasso/grappling hook. Related arrangements can also be inferred for *B. subtilis* SPP1 phage G39P[49], *B. subtilis* DnaI[16,50–52], and *E. coli* phage T4 gp59[53] helicase loaders. The DciA helicase loaders are organized around a type II K homology domain (KH) with Lasso elements at either the amino or carboxy terminus of a particular ortholog or both[12,14,40,41,54].

Cells apply three broad strategies to load hexameric helicases onto nucleic acid substrates: ring-opening, ring-forming, and ring-closing[22,55,56] (Figure 1 and Supplementary Information). Although much is known about many bacterial loaders[11,12,14,16,19,36,42–46], relatively little is known about DciA helicase loaders and the mechanisms they implement during helicase loading. DciA orthologs from

Vibrio cholerae (Vc), *Mycobacterium tuberculosis* (Mt), and *Caulobacter crescentus* (Cc) are all essential proteins[37,42,57,58], and they have been shown to bind to cognate DnaB helicases[12,14,42,57,58]. Component KH and Lasso domains both contact DnaB[12,14,58]. The binding site on DnaB for DciA is proposed to encompass the DH-LH interface[12,14,58]. DciA orthologs bind to DNA[11,58,59], a feature shared with other bacterial loaders[31,35,47,60]. Suppression of DnaB's ATPase activity is a hallmark of the bacterial helicase loaders[43,46,60]; however, Cc DciA has been reported to promote ATP hydrolysis[42]. DciA activates cognate DnaB's DNA unwinding activity by mediating assembly on ssDNA, though the underlying mechanisms have not been established[40,41].

To gain insights into the mechanisms operating during loading of DnaB by the DciA loader and subsequent translocation, we studied orthologs from *Vibrio cholerae* (Vc) and *Mycobacterium tuberculosis* (Mt). The choice of organisms reflects relevance to human disease and a peculiar divergent DciA architecture. The cryogenic electron microscopy (cryo-EM) structure of the Vc-DnaB•ssDNA•ATPγS complex, the end state of helicase loading, implies that cycles of opening/closing of the NTD layer and CTD remodeling are significant features in the mechanism of translocation on ssDNA. We suggest that remodeling of the NTD layer and distinct migrations of two subunits to the top of the DnaB spiral, repeated three times, mediates hand-over-hand translocation. Native mass spectrometry (nMS) indicates that DnaB is a hexamer and that the stoichiometry of the Vc-DnaB-DciA-ssDNA complex is 6:3:1. Vc-DciA features a KH domain at its amino terminus and a disordered segment (Lasso) at its carboxy

terminus; by contrast, in Mt-DciA, this arrangement is inverted[12,40,41,54,58]. Multiple binding experiments show that the Lasso segment specifies most of the binding energy in the interaction with DnaB in both orthologs. Furthermore, Vc- and Mt-DciA bind to cognate DnaB at the interface between the docking helix (DH) and linker helix (LH) on adjacent subunits. Vc-DciA suppresses the intrinsic ATPase activity of DnaB. We show that Vc-DciA loads DnaB onto ssDNA and activates unwinding. Overall, our data suggests that DciA is likely a ring-opening helicase loader.

Results

Cryo-EM Structure of Vc-DnaB Bound to ssDNA and ATPγS

To understand the loading of the DnaB helicase by DciA, we applied cryogenic electron microscopy (cryo-EM) to Vc-DnaB helicase bound to ATPγS, Vc-DciA, and ssDNA derived from the Vc-OriC-I replication origin. In assembling the complex, we relied on results from our nMS study (below). Cryo-EM analysis (Table 1, Supplementary Methods, Supplementary Figures 1 and 2) produced a 3.37 Å structure of hexameric Vc-DnaB bound to ATPγS and complexed to a 22-nucleotide ssDNA molecule (Figures 2 and 3 and Supplementary Figure 3). The resolution of the EM density corresponding to one of the chains (chain A) was of lower resolution than that of other chains. Notwithstanding the fourfold excess of Vc-DciA in the sample submitted to cryo-EM, our maps failed to show any density corresponding to the loader. Our efforts likely recovered the end-state structure of the Vc-DnaB-ssDNA complex after DciA-mediated loading or self-threading.

Compared to the Bst-DnaB-ssDNA complex, determined with GDP•AlF_4 (PDB: 4ESV[10]), the ATPγS form of the Vc-DnaB-ssDNA complex presents a

distinct configuration with several significant changes (Figures 2 and 3). Both share the trimer of dimers and pseudo-sixfold architecture of the NTD and CTD tiers in extant structures (Figures 2 and 3). With diameters of ~55 Å and ~25 Å, the NTD and CTD layers in the Vc-ATPγS form are dilated and constricted[8], respectively. However, the NTD from the Vc-ATPγS structure adopts a closed triangular planar and symmetric arrangement (Figure 3), resembling the NTD from other structures (PDB: 2R5U[61], Root Mean Square Deviation (RMSD) = 2.6 Å; PDB: 7T20[62], RMSD = 1.7 Å). This configuration differs from the open spiral in the GDP•AlF_4 form of the Bst-DnaB-ssDNA complex[10]. As with other DnaB structures, the Vc-NTD assembles around weak (head-to-head) and strong interfaces (tail-to-tail), defined based on the buried surface area[7]; the NTD tier in the Bst structure is breached on the weak head-to-head interface. In both nucleotide forms, the constricted CTD tier is arranged as a closed spiral; however, the spirals are distinct. The six DnaB subunits in the Vc-and Bst structures are labeled A-F-E-D-C-B around the spiral; the breach in the CTD spiral lies between chains A and B, which are at the bottom and top of the spiral (as in the pose in Figures 2 and 3), respectively. Five of the six subunits of each structure (PDB: 4ESV: resid 181:441 and chain A, C, D, E, and F on Vc-DnaB: resid 204:441 and chain B, C, D, E, and F) chains could be superimposed with an RMSD of 1.7 Å (1016 Cα atoms). The most significant difference in CTD configurations is the distinct position occupied by Vc-DnaB chain A, which maps to chain B in the Bst 4ESV structure; we address this change in greater detail below. We also note that in the Vc ATPγS form, chain A is located further away from its neighbors (distances to chain B: ~39.6 Å, to chain

F: ~34.6 Å) than the average distance separating the remaining four subunits to their neighbors (Chains C, D, E, and F: ~33.4 Å). By contrast, in Bst 4ESV, Chain A is distant from one immediate neighbor (distance between chains B and A: 41.6 Å), while other chains display a distance of 32.5 Å to their neighbors. Lastly, in the Vc-ATPγS complex, the six Linker Helices (LH) occupy three positions relative to the NTD and CTD. The LH elements of chains B, C, D, and E occupy one position (LH1), with chains A (LH2) and F (LH3) diverging from this position by rotations/displacements of ~29.6°/12.3 Å and ~16.5°/~7.1Å, respectively. In the Bst 4ESV GDP•AlF_4 complex, the LH elements occupy two positions, one by chains B, C, D, E, and F (LH1), and a second position (LH4) by chain A (Supplementary Figure 4).

ssDNA in the complex traces a spiral path that passes through the internal chamber of Vc-DnaB (Figures 2 and 3). 12 of the 22 ssDNA nucleotides are bound to subunits of the Vc-DnaB hexamer; the remaining 10 are outside the DnaB perimeter (Supplementary Figure 5). In contrast to the GDP•AlF_4 4ESV structure where each subunit contacts ssDNA, only five DnaB subunits in the current Vc-structure make contacts (less than 4.0 Å); chain A does not contact ssDNA. An inventory of protein-DNA contacts reveals the involvement of seven Vc-DnaB residues, though not every contact is made by each subunit (Supplementary Table 2 and Supplementary Figure 6).

Six ATPγS/Mg^{2+} complexes are found at composite catalytic centers formed between adjacent Vc-DnaB subunits, wherein the Walker A/P-loop and Walker B motifs are provided by one subunit and the β-hairpin arginine finger by a second

(Figure 2 and Supplementary Figure 7). In four nucleotide sites (chain F-E, E-D, D-C, and C-B), the β-hairpin/arginine finger makes a close approach to nucleotide on a neighboring subunit, with distances between the P-loop lysine (K234) and the arginine (R439) finger residues of ~11.3 Å. The corresponding distance at the A-F subunit interface is slightly longer (~11.9 Å), and the arginine finger has shifted by ~3 Å relative to other subunits. The β-hairpin/arginine finger at the nucleotide site that lines the breach (B-A) exhibits a considerably longer (~24.5 Å) distance. In the Bst GDP•AlF_4 complex, 5/6 sites (Chains A-F, F-E, E-D, D-C, and C-B) feature an average P-loop lysine (K216) to arginine (R420) finger distance of ~11.44; the chain B-A site, which lines the breach, distance is considerably longer at 32.81 Å.

Taken together, the significant changes between the GDP•AlF_4 and ATPγS forms of DnaB, including distinct NTD configurations, the offset of a single DnaB CTD, and diversity in LH element conformations in sequential subunits around the ring, imply that our structure has captured a distinct intermediate in the translocation reaction.

Remodeling of the NTD and CTD Tiers Accompany Translocation

To gain insights into the distinct ATPγS form of DnaB and its place in the translocation reaction, we compared it against the Bst GDP•AlF_4[10] entity (Figure 3) and a series of DNA complexes (PDB: 6N7I, 6N7S, 6N7T, and 6N7V) of the DnaB-family helicase Gp4 from phage T4[24,29] (Comparisons to the Vc-DnaB structures appears in the Supplementary Information). Aligning the Vc-ATPγS and Bst GDP•AlF_4 structures by superimposing 5/6 CTDs (RMSD: 1.7 Å, a similar alignment could be obtained by aligning on the ssDNA (RMSD: 0.64 Å) reveals

that Vc chain A, excluded from the alignment, is displaced by 25 Å and rotated by ~22° relative to the corresponding subunit in 4ESV (Chain B). Similar displacements/rotations are seen in the HelF subunits in the 6N7T and 6N7V DnaB-family Gp4 helicase structures, shifting positions by ~24 Å and ~13°[24,29]. Further, the DnaB alignment juxtaposes all the components of the NTD layer save for the chains at the top (4ESV: chain A) and bottom (4ESV: chain B) of the Bst spiral. These two chains are offset owing to the distinct planar vs. spiral configurations adopted by the Vc ATPγS and Bst GDP•AlF_4 complexes. Unexpectedly, the breaches in the two structures do not align (Figure 3). Instead, they are offset by one subunit.

Given the distinct states captured by each structure, we reasoned that the Vc ATPγS structure might precede the transition state Bst complex in the DNA translocation reaction coordinate. Ordering the structures in this way specifies a direction for the observed structural changes. Accordingly, the NTD of chain F and chain E in the Vc ATPγS complex will transition from the closed triangular planar configuration to the open spiral of the GDP•AlF_4 complex (mapped to 4ESV chains: A and F); concomitantly, the CTD of Vc-chain A will move upward (as in the pose in Figure 3) to assume the configuration seen in chain B of 4ESV (Supplementary Movie 1). With the migration of the Vc chain A CTD to the position specified in the 4ESV structure, the breach in the CTD spiral moves counterclockwise by one subunit. The LH element moves from the LH2 to the LH4 position in 4ESV chain A. Several lines of evidence in the Vc ATPγS complex support the proposal that the chain A CTD migrates (Figure 3). First, the arginine finger/β-hairpin element

on chain F has peeled away by ~3 Å, relative to its position in chains B, C, D, and E, from the P-loop on chain A (Figure 2C). Second, chain A is farther away from its neighbors than any other DnaB subunit. Third, chain A makes no contact with ssDNA. Lastly, of all the CTDs, the EM density for chain A is the weakest. Together, these findings point to the chain A CTD as disengaged from DnaB and ssDNA and poised to transition.

Due to the NTD layer's asymmetry, the next subunit's motion, chain F, must follow a different trajectory. We propose that on ATP hydrolysis, chain F, now located at the bottom of the spiral, will also peel away from DNA and migrate upwards to a new binding site on ssDNA. In contrast to the motion of chain A, which results in the opening of the NTD layer, the motion of chain F CTD must be accompanied by the closure of the NTD ring from the open spiral to the closed planar configuration; this motion will also result in the adjustment of the position of the LH element, from the LH3 position to the LH1. Together, these two changes re-establish the NTD configuration in the Vc ATPγS structure. Applying the above to chains E and D first and then to chains C and B allows each DnaB subunit to complete a catalytic cycle of ATP hydrolysis amid translocation on ssDNA. These findings highlight the importance of opening and closing the NTD layer, which had previously been suggested to specify the direction of unwinding[63] in the translocation reaction.

Oligomeric State and Stoichiometry of Vc-DnaB, DciA, ssDNA complexes

Next, we used high-resolution native mass spectrometry (nMS) to determine the oligomeric states and the stoichiometry of complexes in the DnaB-DciA system assembled from purified proteins (Supplementary Figure 8). We first

investigated the oligomeric states of DnaB complexes from Vc, *E. coli,* and *B. subtilis* (Supplementary Figure 9A). nMS experiments on Mt-DnaB, with and without a SUMO tag, did not meet our quality control requirements and are not reported here. nMS analysis showed that Vc and *E. coli* DnaB helicases are hexameric, whereas *B. subtilis* DnaC is monomeric (Supplementary Figure 9A), as determined in previous studies[34,64–66]. We observed a sizeable population of lower oligomeric states for Ec and Vc-DnaB ($DnaB_5$, $DnaB_4$, $DnaB_3$, and $DnaB_2$) in samples without Mg•ATP. The addition of a small amount of ATP (10 μM ATP for a 10 μM DnaB monomer sample) before nMS analysis yielded a predominant peak for the hexameric DnaB with minimal subcomplexes (Supplementary Figure 9A), indicating that ATP stabilizes the DnaB hexamer as previously suggested for the *E. coli* ortholog[67,68]. All subsequent nMS experiments with DnaB-containing samples include 10 μM ATP and 0.5 mM magnesium acetate before nMS analysis. Close-up inspection of the nMS spectrum for the Vc-DnaB sample incubated with Mg•ATP showed a peak distribution corresponding to several Mg•ADP-bound states, indicating ATP binding and hydrolysis (Supplementary Figures 9B and 9C).

Next, we examined the complexes between Vc-DnaB, Vc-DciA, and ssDNA derived from the OriC-I chromosomal origin. Our nMS analysis showed that Vc-DciA is monomeric (Supplementary Figure 10). Incubation of 10 μM (as monomer) Vc-DnaB with 7 μM full-length Vc-DciA, in the absence of ssDNA, revealed that the DnaB hexamer bound 1 – 2 copies of DciA, with small amounts of a third copy (Figure 4A). We attempted to analyze samples with higher relative amounts of DciA (> 10:7 DnaB: DciA) but encountered significant disassembly of Vc-DnaB

complexes with Vc-DciA upon initiation of electrospray during nMS analysis (Supplementary Figure 11). Stoichiometries of 6:3 or 6:6 for the Vc-DnaB-Vc-DciA complex have been estimated from small angle X-ray scattering, and the X-ray crystal structure [12,14]

DnaB accepts ssDNA into its central chamber, the basis for the so-termed fork DNA unwinding assay[12,42,69]. Accordingly, we found that Vc-DnaB alone could bind OriC-I-derived ssDNA (Figure 4B). nMS analysis of a mixture comprising Vc-DnaB, Vc-DciA, and the ssDNA showed that up to three copies of Vc-DciA could associate with ssDNA-bound DnaB (Figure 4B). Interestingly, there is a marked increase in the relative peak intensity for the 6:3 DnaB:DciA assembly when ssDNA is bound compared to the ssDNA-free sample, suggesting that ssDNA association promotes the formation or stabilization of this higher-order ensemble (Figure 4B).

We also investigated the binding of specific Vc-DciA domains to Vc-DnaB. We used limited proteolysis with nMS readout to validate the predicted arrangement of the KH and Lasso domains in Vc-DciA (Supplementary Information and Supplementary Figure 12). nMS analysis of Vc-DnaB titrated with increasing concentrations of the Lasso domain of DciA showed a progressive increase in the number bound to the DnaB hexamer with 1 – 4 copies bound when both proteins are present at equimolar amounts to 2 – 6 copies bound at four-fold excess of DciA-Lasso (Supplementary Figure 13A). In contrast, only one copy of the DciA KH domain was found associated with $DnaB_6$ at ~10% relative peak intensity even at six-fold molar excess, indicating that the KH domain of DciA weakly binds to

DnaB (Supplementary Figure 13B). Incubation of Vc-DnaB with the two separate DciA domains at the highest concentrations studied did not change the maximum number of bound copies observed (i.e., one and six for the DciA KH and Lasso domains, respectively, Supplementary Figure 13B). Contrary to what was observed with DnaB and full-length DciA, no DnaB helicase disassembly was observed during the electrospray nMS analysis when either or both DciA domains were used in excess. Moreover, the distribution of DnaB:DciA-KH assemblies did not change (1 – 4 copies of DciA-KH remained bound to $DnaB_6$ at equimolar amounts of both proteins) in the absence or presence of ssDNA (Supplementary Figure 14).

Our nMS experiments revealed the stoichiometry of the isolated Vc-DnaB helicase and its complex with DciA and OriC-I-derived ssDNA; both estimates are crucial to deciphering the loading mechanism. The hexameric nature of Vc-DnaB implies that it is a closed protein ring and that the DciA helicase loader is likely a ring-breaker. The 6:3:1 stoichiometry of the Vc-DnaB-DciA-ssDNA complex suggests that although six DciA binding sites may exist on DnaB, only three are used; this value will be crucial to understanding how the DnaB:DciA will interact with other factors during replication initiation.

Vc and Mt-DciA Bind to Cognate DnaB Helicases with High Affinity

Next, we used orthogonal approaches to show that DciA binds to cognate DnaB and that the DciA binding is likely near the DH—LH interface (Figure 5). First, we conducted so-termed NiNTA ‘pull-down’ experiments to examine the binding between full-length and truncated constructs of DciA and DnaB (Figures 5A and 5B and Supplementary Figures 15 and 16). Full-length DciA (Vc and Mt)

binds to full-length cognate DnaB. Vc and Mt DnaB constructs that span the LH and CTD domains also retain binding to full-length cognate DciA (a shorter construct spanning the CTD could not be expressed). No other DnaB construct (NTD or NTD-LH) showed binding to full-length cognate DciA. Parallel experiments with constituent KH (Vc: 1:98; Mt: 1:89) and Lasso domains (Vc: 98:157; Mt: 90:189)) revealed that both bound to full-length cognate DnaB, although Vc-DciA KH domain bound weakly. Remarkably, although the KH and Lasso domain architecture of the Vc and Mt homologs of DciA exhibit is inverted, each Lasso domain binds to the cognate construct, including the LH-CTD domains of DnaB. No other truncated DnaB construct (NTD or NTD-LH) showed any interaction with either the KH or Lasso domains. These data point to the LH interface as a strong candidate for part of the DciA binding site, with another part comprised of the CTD itself.

Next, we applied surface plasmon resonance (SPR) to quantify the interaction between DnaB and DciA. We immobilized full-length DciA, the isolated KH, and Lasso domains to the SPR chip, measured on and off rates for cognate full-length DnaB, and extracted dissociation constants (Figures 5C, 5D, 5E, and 5F). As our pull-down binding experiments anticipated, Vc-DnaB bound tightly (K_D = 0.58 nM) to full-length Vc-DciA. We found the isolated Vc Lasso domain bound to DnaB with a K_D = 65 nM, but the KH domain exhibited a weak affinity (K_D = 170 nM). Full-length Mt-DciA and the isolated Lasso and KH domains displayed similar K_Ds to full-length Mt-DnaB (Supplementary Figures 17 and 18). The additional degrees of freedom to engage with Mt-DnaB enjoyed by the Mt Lasso and KH

domains might explain why the truncated constructs bind with higher affinity than full-length.

The binding and SPR data suggest that, even though the Vc and Mt-DciA orthologues feature inverted KH and Lasso architectures, they bind to their cognate DnaB helicase using equivalent domains. Moreover, our data also reveal that the most significant contacts between DciA and DnaB are found at the LH and CTD domains of DnaB and that the Lasso domain is the locus of many of the most significant contacts to cognate DnaB. Given that both *E. coli* DnaC and phage λ P bind at the DH-LH interface of two adjacent DnaB subunits[19,43,44,48], the finding that the LH constitutes the DciA binding establishes this site as a conserved site with significance for DnaB helicase loading.

Suppression of DnaB's ATPase Activity by DciA

One of the hallmarks of a bacterial helicase loader is the suppression of ATPase activity of the cognate helicase[43,46,60]. Our ATPase study first compared the wild-type and the Walker B mutant E259A Vc-DnaB at a single concentration (200 nM); we found robust activity in wild-type Vc-DnaB, which was lost in the mutant (Figure 6B). Next, we measured the influence of full-length and truncated constructs of DciA on the ATPase activity of DnaB. We found that titration of full-length Vc-DciA revealed potent suppression of Vc-DnaB's ATPase activity (untagged DnaB: $IC_{50} \approx 26$ nM, NHis-DnaB: $IC_{50} \approx 26$ nM, Figure 6A). A construct encompassing the Vc KH domain (1:98) exhibited an $IC_{50} \approx 420$ - 1540 mM (Supplementary Figure 19A); the weaker inhibitory constant is congruent with the weak interaction signaled by our nMS study and the NiNTA-based binding studies. Even though we found that the Vc Lasso domain (98:157) binds to full-length Vc-

DnaB, titration revealed no effect on Vc-DnaB's ATPase activity at low DciA concentrations (25 – 400 nM). However, at very high concentrations (800 – 6400 nM) of Vc-DciA, we observed reproducible stimulation (up to 2.5 x) of DnaB's ATPase activity (Supplementary Figure 19B).

Parallel analysis of Mt-DnaB and Mt-DciA unexpectedly revealed that ATPase activity could not be measured reliably and appeared inconsistent even when the concentration was increased fourfold. Our measurements showed that wild-type and Walker B mutant E257A Mt-DnaB exhibited similar catalytic rates (Figure 6B); these data suggested that Mt-DnaB was inactive in our hands (Supplementary Figure 20), and, as such, we could not test Mt-DciA for inhibitory activity towards Mt-DnaB.

DciA Loads DnaB on Physiological DNA Bubble Substrates

The nMS binding data and DNA unwinding experiments (Supplementary Information and Supplementary Figures 21, 22, 23, and 24) implicate DciA as a helicase loader since DciA enhances both underlying activities. However, the substrates employed in the above assays (ssDNA, 5' and 3' ssDNA tailed fork) do not permit self-threading into DnaB's central chamber to be distinguished from loading/assembly around ssDNA. Physiologically melted DNA by DnaA at a replication origin has no free termini, and, as such, assembly around ssDNA, rather than threading, is expected to be the predominant form of loading *in vivo*.

To distinguish the DciA-mediated assembly of Vc-DnaB on ssDNA from self-threading, we measured unwinding from the so-termed DNA bubble substrate, which features no free ends, unlike a tailed-fork substrate. Our assay employed DNA molecules #894 and #895 described in reference[42], which we converted into

a FRET-based readout by adding a Cy3 fluorophore at one 5' end and the Iowa Black RQ quencher at the corresponding 3' end (Figure 7). We also measured DnaB loading onto a doubly labeled DNA bubble (Supplementary Information and Supplementary Figure 25, 27C, and 27D).

No fluorescence signal was observed when DciA was omitted (Figure 7, red curve), leading us to conclude that self-threading of ssDNA into DnaB had been suppressed by using the bubble substrate. Titration of full-length Vc-DciA (0.11 to 6400 nM) revealed a 10-fold (~15 to ~150) increase in fluorescence at the highest concentration (6400 nM). The increase in fluorescence strictly depended on ATP since the Vc-DnaB E259A mutant showed no activity (Supplementary Figure 26). Substitution of the two DciA truncations – the NTD KH and the CTD Lasso – for full-length Vc-DciA revealed essentially no loading activity (less than 5%) (Supplementary Figures 27A and 27B).

To better understand Vc-DciA's loading activity, we repeated the above titration without Vc-DnaB. Surprisingly, titration of DciA against the DNA bubble substrate revealed a substantial fluorescence signal (Figure 7B); these data imply that Vc-DciA has a previously undiscovered activity: to unwind dsDNA on its own. This activity did not require ATP. The finding that isolated Vc-DciA produced a fluorescence signal ~66% of that seen in the Vc-DnaB•DciA titration implies significance, though establishing biological relevance will require further experimentation. DciA's apparent unwinding activity is not observed when the DNA bubble is substituted with the fork substrate (Supplementary Figure 24), pointing to a role for DNA structure in this activity.

We subtracted the two signals to separate the unwinding activities of Vc-DnaB•DciA and isolated Vc-DciA (Figure 7C). The calculated signal from Vc-DnaB, when acted upon by Vc-DciA, showed a 25-fold (~5 to ~125 RFU, Figure 7C) increase in fluorescence at the highest concentration (6400 nM) (Figure 7D). These data strongly argue that Vc-DciA is a helicase loader for Vc-DnaB.

The congruence of the DNA unwinding and helicase loading curves during titration with full-length Vc-DciA suggests that, to a large degree, helicase loading rather than threading occurs with full-length DciA in both assays (Figure 7D and Supplementary Figure 21B). On the other hand, dissimilarity in the curves corresponding to the Vc-DciA truncations implies that loading is not retained in either construct or that the observed DNA unwinding activity in the truncated constructs may arise solely from self-threading. Our data establish a helicase-loading biochemical activity for the Vc-DciA protein. Moreover, the finding that loading onto the bubble substrate does not occur absent DciA supports a closed ring configuration for DnaB.

Discussion

Our analyses of the bacterial DciA loader and the DnaB helicase from *Vibrio cholerae* and *Mycobacterium tuberculosis* sheds new light on the underlying helicase-loading and activation pathway (Figure 8). In bacteria, two copies of the DnaB replicative helicase are assembled onto single-stranded DNA introduced into the replication origin by the DnaA initiator protein. It is now clear that most bacteria lack an ortholog for the well-studied DnaC helicase loader; instead, the DciA helicase loader appears likely to be the predominant loading factor [37,40,41]. Vc- and Mt-DciA bind to cognate hexameric DnaB with a low nM K_D. Although

their KH and unstructured Lasso domains feature an inverted organization, the unstructured Lasso segment mediates significant binding energy to the interaction with DnaB. Also, irrespective of the divergent internal organization, an essential part of the DciA binding site lies at the nexus of DnaB's DH and LH elements. Prior studies suggested stoichiometries of 6:3 or 6:6 for the Vc-DnaB-Vc-DciA complex and a binding site at the DH-LH nexus [12,14]. We find up to three copies of Vc-DciA and one copy of replication-origin-derived ssDNA bound to Vc-DnaB. The stoichiometry of the DnaB-DciA system distinguishes it from the *E. coli* DnaB-DnaC and DnaB•λP complexes, which feature 6:6 and 6:5 stoichiometries, respectively[19,43,44,48]. The unwinding activity of DnaB is significantly stimulated by DciA on fork and replication origin-mimicking DNA bubble substrates. The finding that isolated Vc-DnaB is a hexamer under physiological concentrations of ATP (Figure 4) and exhibits essentially no self-loading on the replication-origin mimicking DNA bubble substrate (Figure 7) leads us to conclude that DciA is a ring-opening-type helicase loader.

Our structure of the ATPγS form of the DnaB-ssDNA complex provides new insights into the mechanisms of translocation. The topologically closed NTD and distinctly configured CTD layers distinguish the ATPγS state from a structure previously determined bound to the transition state ATP analog GDP•AlF_4[10] and provide a first view of nucleotide-dependent conformation switching during ssDNA translocation. Our model for ATP-dependent translocation by DnaB extends the hand-over-hand mechanism[10] by integrating cycles of opening/closing of the NTD layer, reconfiguration of the LH element, and dissociation of individual CTDs from

ssDNA and neighboring subunits followed by their migration to the top of the DnaB spiral to new ssDNA binding sites. Migration to the top of the spiral is facilitated by the engagement of its β-hairpin arginine finger with a freshly bound ATP by the DnaB subunit that precedes it at the top of the spiral; ATP binding stabilizes contacts to ssDNA. We suggest that translocation encompasses three identical sub-steps. Each sub-step involves migration of the chain A CTD (or chain E or chain C) with the simultaneous opening of the NTD layer into an open spiral, as seen in the Bst-4ESV structure. In the second step, migration of the next CTD (chain F, chain D, or chain B) in sequence, newly at the bottom of the spiral, is accompanied by the closure of the NTD layer to the triangular planar arrangement seen in the Vc- ATPγS structure. Our model specifies that two DnaB subunits move in sequence and that this program of motion is repeated thrice around the hexamer. Our structure may inform debate on whether the DnaB subunits' motion is sequential, stochastic, or concerted [10,22,28,29,70–74].

To link the significant findings of our work in DciA-mediated loading and subsequent translation by DnaB, we looked to another ring-opener, DnaC, to provide models for other steps in the helicase loading pathway (Figure 8). The configuration of DnaB in the *E. coli* DnaB-DnaC•ssDNA (PDB: 6QEM) complex[19] closely resembles that of the 4ESV GDP•AlF_4 state[10], with a closed spiral CTD and open spiral NTD and contacts to ssDNA by each subunit. Since the 6QEM structure has an unfilled nucleotide site at the top of the spiral (as in the pose in Figure 8), on the departure of the loader, it needs only bind ATP to align with the 4ESV structure and enter the two-DnaB subunit motion (Figure 8E-F) scheme

proposed above. Notably, the departure of the DciA loader produces a DnaB configuration after it has taken the first of the two sequential steps described above (Figure 8D). We suggest that after the eviction of the loader, the subunit at the bottom of the spiral will take the second of these steps to migrate to the top of the spiral (Figure 8E-F). Repetition of the two DnaB subunit sequenced motion around the ring accompanies further translocation along ssDNA. Notably, a crystal structure of the 6:6 Vc-DnaB-Vc-DciA complex implies two distinct DciA binding modes and a closed planar DnaB[14]. Additional studies will be required to sequence this complex in the helicase loading reaction.

An important unanswered question centers on the mechanism of expulsion of DciA from the DnaB-ssDNA complex. The DnaC [19,60,75] and λP [76,77] systems feature biochemical programs to mediate loader dissociation. Our data reveals a tight interaction between helicase and loader (Figure 5) that suppresses DnaB's ATPase activity (Figure 6). Yet, DciA exhibits a dose-dependent stimulation of DnaB's unwinding activity (Figure 7 and Supplementary Figure 21), absent any other factor. These findings suggest that DciA may spontaneously dissociate to relieve inhibition of DnaB's ATPase activity and enable unwinding activities. It is also possible that interactions with other replisome components [25,75,78] could contribute to the eviction of DciA. Future studies will have to clarify this question.

Materials and methods

Plasmids, Protein Expression, Purification, and Biochemistry

Standard techniques[79] were used to develop the 21 protein expression plasmids and express and purify the encoded proteins. Our studies encompassed efforts with full-length and designed truncations of DnaB and DciA from *Vibrio cholerae* and *Mycobacterium tuberculosis*; our collection included histidine and SUMO-tagged constructs. The DnaB constructs included the full-length sequence (Vc: 1-468; Mt: 1-457), the DnaB amino-terminal domain (NTD; Vc: 1-170; Mt:1-170), the DnaB amino-terminal domain fused to the Linker Helix (NTD-LH; Vc: 1-208; Mt:1-278), the Linker helix fused to the DnaB carboxy-terminal domain (CTD; Vc: 208-468; Mt:171-457). The DciA constructs included the complete sequence (Vc: 1-157; Mt: 1-189), the KH domain (Vc: 1-98; Mt: 90-189), and the Lasso domains (Vc: 98-157; Mt 1-89). Notably, the Mt-DnaB gene (1:874) contains an intein (residues 400:815)[61,80,81]; our expression plasmids omitted the intein. To keep the Mt-DnaB numbering consistent with other orthologs that lack inteins, we numbered the sequence from 1-457, where the intein was excluded. The supplementary methods section (Supplementary Methods and Supplementary Tables 3 and 4) provides complete details on the construction of the plasmids, expression, bacterial expression conditions, and purification.

Interactions between DnaB and DciA and their respective truncations were interrogated by mixing and co-lysing bacteria that separately expressed each protein, where only one of the proteins was histidine-tagged. The lysate was passed over NiNTA agarose (QIAGEN), washed of contaminants, and histidine-tagged proteins were eluted. Interactions were scored based on the propensity of

the untagged protein in the experiment to be retained on Ni-NTA agarose (QIAGEN) compared to trials where the histidine-tagged protein was omitted. The supplementary methods section describes the so-termed 'pull-down' experiments more completely.

Surface Plasmon Resonance

Dissociation constants (K_D) were estimated using surface plasmon resonance (SPR) from measurements of the on and off rates between DnaB and DciA. SPR data were acquired using a Biacore X100 instrument (GE Healthcare/Cytiva) and a CM5 sensor chip functionalized with an anti-histidine antibody according to the manufacturer's instructions. All measurements were conducted at 25 °C. Since SPR response is proportional to molecular weight, we chose to immobilize the smaller N-His-DciA (Vc: MW = 18.4 kDa; Mt: MW: 21 kDa) while positioning the much larger DnaB (Vc: MW = 312.3 kDa; Mt: MW: 301.5 kDa), in the mobile phase. DciA was immobilized on the surface of a single channel of the CM5 sensor chip via the interaction between the histidine tag and the anti-histidine antibody. The appropriate ligand density (RL) on the chip was calculated according to the equation: $RL = \left(\frac{ligand\ MW}{analyte\ MW}\right) \times R_{max} \times \left(\frac{1}{S_m}\right)$ where R_{max} is the maximum binding signal, and S_m corresponds to the binding stoichiometry. With the immobilization procedure complete, non-specifically bound proteins were removed by washing with buffer HBS-EP+ (Cytiva), until the resonance signal reached a constant baseline. The reference flow cell provided a control surface for refractive index change and non-specific binding. DnaB solution was injected five times at increasing concentrations over the DciA-functionalized sensor surface in a single-cycle kinetics experiment. A long dissociation phase and a single

regeneration step followed the last sample injection without regeneration between each sample injection.

The interaction between DnaB and DciA was assumed to display 1:1 kinetics; as such, the measured SPR data should display pseudo-first-order kinetics that is described by the following rate equation:

(1) $$\frac{d[LA]}{d[t]} = k_a \cdot [L] \cdot [A] - k_d[LA]$$

where k_a is the association rate constant, which refers to the rate of complex formation (units: $M^{-1}s^{-1}$); the dissociation rate constant k_d describes the stability of the complex, i.e., the fraction of complexes that dissociate in the time frame (units: M). [A] represents the analyte concentration; [LA] is the complex concentration measured directly as R in Resonance Units (RU); [L] is the ligand concentration on the surface.

To enable fitting of the SPR data, equation (1) was modified as follows:

(2) $$\frac{d[R]}{d[t]} = k_a \cdot [C] \cdot [Rmax - R] - k_d[R]$$

where Rmax is the maximum binding capacity, and Rmax-R is the free concentration of the analyte. Rmax and R were extracted from the experimental SPR curves. The fitted data proved estimates for k_d and k_a from which $K_D = k_d/k_a$ was calculated. Experimental binding kinetic data were fit to the '1:1 binding' model implemented in the Biacore X100 Control Software (Cytiva).

Native Mass Spectrometry

DnaB and DciA samples for native mass spectrometry (nMS) were exchanged into 500 mM ammonium acetate, pH 7.5, and 0.01% Tween-20 (nMS buffer) using a Zeba micro spin desalting column with a molecular cutoff of 40 kDa (ThermoFisher Scientific). Complexes containing DnaB and DciA in the above buffer were mixed in defined molar ratios before nMS measurements. To take data in the presence of nucleotide, ATP and magnesium acetate were added to final concentrations of 10 μM and 0.5 mM, respectively.

The list of DNA molecules used in the nMS study appears in Supplementary Table 4. Lyophilized synthesized ssDNAs (IDT) oligonucleotides were brought to 200 μM in HPLC-grade water and diluted to a working concentration of 3 - 6 μM in the above nMS buffer.

An aliquot (3 – 5 μL) of an experimental sample was loaded into a gold-coated quartz capillary tip prepared in-house. The sample was then electrosprayed into an Exactive Plus EMR instrument (Thermo Fisher Scientific) using a modified static nanospray source [82,83]. Spectra were continuously recorded from a single sample-loaded capillary. For analysis of DnaB and DnaB-containing assemblies, the general MS parameters used include spray voltage, 1.2 – 1.3 kV; capillary temperature, 125 – 150 °C; S-lens RF level, 200; resolving power, 8,750 or 17,500 at *m/z* of 200; AGC target, 1 x 10^6; number of micro scans, 5; maximum injection time, 200 ms; in-source dissociation (ISD), 0 – 10 V; injection flatapole, 8 V; interflatapole, 4 V; bent flatapole, 4 V; high energy collision dissociation (HCD), 200 V; ultrahigh vacuum pressure, 5 – 7 × 10^{-10} mbar; total number of scans, 100. For analysis of full-length DciA, the MS parameters are similar as above except for capillary temperature, 100 °C in-source dissociation (ISD), 100 V; injection flatapole, 8 V; interflatapole, 7 V; bent flatapole, 6 V; higher-energy collisional dissociation (HCD), 0 V; ultrahigh vacuum pressure, 1.4 × 10^{-10} mbar. Mass calibration in positive EMR mode was performed using a cesium iodide solution. Raw nMS spectra were visualized using Thermo Xcalibur Qual Browser (version 4.2.47). Data processing and spectra deconvolution was performed using UniDec version 4.2.0 [84,85] with the following general parameters:

background subtraction (if applied), subtract curve, 10; smooth charge distribution, enabled; peak shape function, Gaussian; degree of Softmax distribution (beta parameter): 2 – 20. PDBO measured all mass spectrometric data in the laboratory of BTC.

Limited Proteolysis/Mass Spectrometry

Trypsin and Asp-N were selected for limited proteolysis to probe flexible domains and protease-accessible sites across the full-length DciA (Vc and Mt). DciA orthologs and the two proteases were buffer-exchanged into 500 mM ammonium acetate, 0.01% Tween-20, pH 7.5 using a Zeba micro spin desalting column with a molecular cutoff of 40 kDa. Proteolysis was initiated by mixing DciA with trypsin or AspN at protease-to-DciA molar ratios of 1:100 or 1:500. The sample was then loaded into a conductive emitter and electrosprayed into the nMS instrument.

nMS data from the limited proteolysis reactions were acquired using the following parameters: spray voltage, 1.2 – 1.3 kV; capillary temperature, 125 °C; S-lens RF level, 200; resolving power, 8,750 at m/z of 200; AGC target, 1×10^6; number of microscans, 5; maximum injection time, 200 ms; in-source dissociation (ISD), 200 V; injection flatapole, 8 V; interflatapole, 7 V; bent flatapole, 6 V; higher-energy collisional dissociation (HCD), 0 – 10 V; ultrahigh vacuum pressure, 5 – 7 $\times 10^{-10}$ mbar; total number of scans, 100.

The nMS RAW file for each time course was processed using the MetaUniDec software (v 4.4.1) [84,85]. First, the MS RAW file was converted into a hierarchical data format 5 file (HDF5) using the Automatic Chromatographic

Parsing function with auto import by time setting with a time window of every 0.5 min. This setting averages all the MS scans for every 0.5 min within the chromatogram. The resulting HDF5 was then used for automatic deconvolution to extract mass and intensity information for each species detected. The deconvolution parameters used were m/z range: 500 – 4,000; mass range: 5,000 – 20,000 Da; sample mass every 0.5 Da; peak width FWHM: 0.8 Th; smooth charge state distribution, on; and peak shape function, Gaussian. The resulting time series were then plotted using Microsoft Excel.

ATPase Rate Measurements

An NADH-coupled microplate spectrophotometric assay was used to measure rates of ATP hydrolysis [86,87] by Vc-DnaB and how rates are affected by the presence of our suite of full-length and truncated constructs of Vc-DciA. In all experiments, Vc-DnaB was kept fixed at 200 nM, while titrations of DciA encompassed concentrations between 0 nM and 6400 nM.

NADH oxidation data were recorded in the presence of 2 mM ATP (Gold Biotechnology, Inc. p/n: A-081-1), 2 mM phosphoenolpyruvic acid monopotassium salt (PEP), 0.01 U/μL lactate dehydrogenase (Sigma-Aldrich, L1254), 0.002 U/μL pyruvate kinase (Sigma-Aldrich, p/n: P7768,) and 0.3 mM NADH in the following buffer: 50 mM potassium-HEPES – pH=7.5, 150 mM potassium acetate, and 8 mM magnesium acetate, 5 mM β-mercaptoethanol, and 0.25 mg/mL bovine serum albumin (Sigma-Aldrich p/n: A3912). The above components were combined, save for ATP, into wells of a Corning 96-well Clear Flat Bottom UV-Transparent Microplate (p/n: 3635), and the plate was warmed to 37 °C for 5 minutes. After the quick addition of 2 mM ATP, the plate was inserted into a SpectraMax M5 plate

reader (Molecular Devices), and absorbance data was taken at 340 nm every 30 s over 30 min. Raw data were exported in text format and imported into Microsoft Excel for analysis. Each absorbance curve was manually inspected to identify a 10-minute period during the experiment wherein the slope of the 340 nm absorbance vs time was constant. The values in the above period were divided by the (-)6.22 mM^{-1} cm^{-1} extinction coefficient of NADH and the pathlength in cm calculated by the plate reader to result in the rate of ATP hydrolysis in mM/s; further division by the mg of DnaB in the assay provided the specific activity in mM/s/mg.

FRET-based DNA Strand Displacement Assay

DNA unwinding by DnaB and its stimulation by DciA was measured using a fluorescence resonance energy transfer (FRET) helicase strand displacement assay adapted from. The DNA substrate for the assay was identical to that in reference[20] and termed FRET-DNA-fork-top-strand, FRET-DNA-fork-bottom-strand, and FRET-DNA-fork-capture-oligo. The top strand is labeled with Cy3 at its 5' end; the bottom strand is labeled with the BHQ_2 quencher at its 3' end. The capture oligo is unlabeled (Supplementary Table 4 and Supplementary Figures 21, 22, 23, and 24).

Strand displacement was measured by mixing annealed and fluorescence-quenched substrate at a concentration of 100 nM with 200 nM DnaB and DciA concentrations ranging from 0 mM to 6400 mM. An excess of the capture oligo (400 nM) was included to prevent the reannealing of the fork after strand displacement. FRET data was taken at 37 °C in the following buffer: 20 mM K-HEPES pH = 7.5, 5 mM Mg acetate, 50 mM K-glutamate, 5% glycerol, and 4 mM dithiothreitol (DTT). Reaction components were mixed into wells (volume: 100

1 μL/well) of a Corning black plate (p/n: 3880) with 96 half-area clear flat bottom
2 wells. The working concentration of NaCl in the assay is 50 mM. The reaction
3 was initiated by adding 1 mM ATP to each well; the plate was subsequently
4 inserted in a SpectraMax M5 plate reader (Molecular Devices). FRET signals were
5 recorded for 30 min at 37 °C. To avoid the crosstalk between Cy3's closely spaced
6 excitation and emission signals, an excitation wavelength of 520 nm was used; at
7 this wavelength, excitation is reduced to 50% of its maximal value
8 (https://www.thermofisher.com/us/en/home/life-science/cell-
9 analysis/fluorophores/cy3-dye.html); however, this wavelength does not overlap
10 with the fluorescence emission peak, measured at 570 nm. Relative Fluorescence
11 Unit (RFU) data taken in this way were exported for analysis in Microsoft Excel and
12 GraphPad Prism.

13 **FRET-based Replicative Helicase Loading Assay**

14 To measure helicase loading by DciA, we adapted the unwinding assay
15 described above; instead of a so-termed fork substrate with 5' and 3' unpaired
16 segments, we employed substrates that featured single-stranded 'bubbles' (Figure
17 7 and Supplementary Figures 25, 26, and 27) whose sequences are taken from
18 (#894 and #895, reference[42]). Bubble substrates favor DnaB assembly on ssDNA
19 instead of threading the free end of ssDNA end in the DnaB central chamber. In
20 our first bubble substrate, the top strand (as drawn in Figure 7) was singly labeled
21 at the 5' end with Cy3, and the bottom strand with the Iowa Black RQ quencher
22 (IDT). To account for the possibility that DnaB helicase could, in principle, be
23 loaded for translocation in either direction, we employed a second substrate
24 wherein fluorophore – quencher pairs were installed at both ends of the 'bubble'

(Supplementary Information and Supplementary Figures 25, 27C and 27D); such a substrate could inform on the loading and translocation on both strands and in both directions. As with the strand displacement assay, unlabeled capture strands forestalled the reannealing of the quencher-containing bubble strand.

FRET signals from helicase loading were recorded and analyzed as described for the strand displacement assay.

Sample and Grid Preparation for Single Particle Cryo-EM

To prepare complexes for cryo-EM, untagged Vc-DnaB-FL and Vc-DciA-FL-CHis were diluted in 20 mM HEPES pH = 7.5, 200 mM NaCl, 5 mM MgCl2, 5 mM β-mercaptoethanol, and 5 mM ATPγS to reach a final concentration of 18 μM (DnaB monomer) and 12.7 μM (DciA). A ssDNA oligonucleotide bearing the origin of the replication sequence of *Vibrio cholerae* serotype O1 (Supplementary Table 4, oligo: O1b-Vc-F) was added at a concentration of 5.4 μM. 3 μL of the Vc-DnaB-DciA-ssDNA sample were applied to a Quantifoil UltrAuFoil R1.2/1.3 Au300 grid, previously plasma cleaned with a 3:1 ratio of Ar/O_2 at 15 W for 10 seconds in a Gatan Solarus II glow discharger. Liquid absorption was allowed for 30 seconds at 4 °C and 100% humidity. The sample was then blotted for 4 seconds with a blot force of 4 and plunge-frozen into liquid ethane. The procedure was conducted on a Vitrobot Mark IV (Thermo Fisher). The grid was stored in liquid nitrogen until data collection.

Cryo-EM Data Acquisition

Cryo-EM images were acquired on a Titan Krios (ThermoFisher) operating at 300 keV and fitted with a Gatan K3 direct electron detector. 12,265 movies were collected using Leginon [88,89] at a magnification of 81,000, corresponding to a pixel

size of 0.541 Å/pixel, and at a defocus of -1.57 µm. The total exposure dose was 51.37 e–/Å^2, and the exposure time per movie was 2 seconds. Additionally, 20° and 40° tilted images were collected to mitigate the expected preferred particle orientation that would otherwise compromise the EM reconstruction.

Cryo-EM Image Processing

The 12,265 images measured from the Vc-DnaB-DciA-ssDNA-ATPγS complex were processed using two approaches (Supplementary Figure 1): a) template-based picking using a prior DnaB structure (PDB entry = 7T20[62]) as the initial template, and b) so-termed blob-picking. For facile computing, the blob-picking approach initially targeted 10% of the images, which produced 2.5 million particles that were 2D classified and submitted to *ab initio* reconstruction with C1 symmetry enforced. This reconstruction generated two volumes, C0 and C1 (~123K and ~151K particles), which were judged to be of low quality and influenced our decision not to pursue the blob-picking approach further.

For the PDB structure-based template-picking approach, for computational ease, we selected 100 frames at random, binned them by a factor of ½, and submitted them for motion correction and Contrast Transfer Function (CTF) estimation as implemented in cryoSPARC [90–96]. Unless otherwise indicated, the following steps were performed within cryoSPARC. An EM map was calculated from PDB entry 7T20 in EMAN2[97] and used to derive templates for application to the above 100 images; this procedure netted 92,178 particles. From this collection, 79,820 particles were extracted using a box size of 360 pixels and 2D classification. Subsequently, *ab initio* reconstruction was performed with C1 symmetry, which produced two classes (A0, A1). Class A0 (18.5K particles) was

carried forward to homogeneous refinement, which created an 8.72 Å map (B0). Inspection of Class A1 suggested a lower quality than A0. As such, further processing of Class A1 was not pursued.

The complete data set (12,165 images) was then submitted to motion correction (Fourier crop factor of ½) and CTF estimation using standard settings. These calculations enabled manual curation leveraging ice thickness (0.82-1.1) and CTF fit resolution (2.17-9.98) parameters to eliminate images with low overall resolution. The resulting 11,705 images were submitted to template-based picking using the B0 map; this calculation produced ~4.3 million particles. These particles were extracted as above and submitted to 2D classification and *ab initio* reconstruction using C1 symmetry. The resulting volumes, D0 and D1 (~374K and ~426K particles), were submitted to heterogeneous refinement and produced two volumes, E0 and E1 (~246K and ~553K particles). Inspection of these two volumes implied that the 6.24 Å E1 volume was of higher quality.

Particles from the E1 Class were re-extracted using a box size of 360 pixels, with no Fourier crop, and submitted to non-uniform refinement, which yielded an EM map with a resolution of 3.37 Å (Volume F). This map was further sharpened with DeepEMhancer [98] to produce volume G; this volume embodied our best map and was used for model building (below). Clear density was evident for the protein, nucleic acid, and nucleotides. Indeed, estimates of the local resolution ranged from 2.8 Å to 4.8 Å, with the highest resolution density spanning the DnaB-CTDs (Supplementary Figure 2C). The quality of the protein density was sufficient to

allow unambiguous assignment of side chains to the map. However, no density could be assigned to the DciA loader.

Next, we made several efforts to improve the resolution of Map G in hopes of locating the DciA loader. 3D classification of the particles that generated Map F produced ten classes (group H). Classes H1 and H9 retained the highest number of particles, 82K and 77K, respectively, and showed high similarity to Map G, but with no features that could be assigned to Vc-DciA. Non-uniform refinement was performed on volumes H4 (46K particles) and H6 (59K particles), producing maps at the resolution of 3.76 Å (class I4) and 3.78 Å (class I6). Automatic model building with ModelAngelo [99] on the sharpened map, once again, failed to show any evidence of Vc-DciA. Homogenous refinement of the particles that produced the E1 volume created class K, followed by two consecutive rounds of non-uniform refinements (classes L and M) with different settings, using volume E1 as the input map. This procedure generated Map M, followed by Map N after DeepEMhancer sharpening, with both at resolutions of 3.45 Å. Neither map showed evidence of density better than Map G, let alone proof of the presence of Vc-DciA. Lastly, inspecting the 3D variability analysis of the particles that produced volume F (group J) produced no evidence of conformational changes in the Vc-DnaB-ssDNA complex.

Model Building and Structure Refinement

The DeepEMhancer-sharpened map G was selected to build a molecular model of the Vc-DnaB-ssDNA complex. Map G was submitted to ModelAngelo [99] to construct the initial protein and DNA model. The quality of the resulting model was high, even as it contained numerous chain breaks. Next, we superimposed

the AlphaFold predicted structure of Vc-DnaB, which has been split into its three component domains (N-terminal Domain (NTD, residues 1:170), Linker Helix (LH, residues 171:211) and C-terminal Domain (CTD, residues 212:468)), onto the ModelAngelo created model to create a model of hexameric Vc-DnaB with excellent stereochemistry. The program COOT [100] was used to connect domains belonging to each monomer and to remove the following DnaB residues (chain A, B: 1-21 and 463:468, C-E-F: 1:21 and 464:468, D: 1:22 and 464:468) because of missing map density. Although Vc-DciA was present in a four-fold excess in our cryo-EM sample, we found no EM density that the Vc-DnaB model did not explain. As such, we conclude that Vc-DciA is not present in our reconstruction.

The EM density in Map G revealed an 11-mer ssDNA within the internal chamber of DnaB. This was sufficiently resolved to allow the DNA backbone to be distinguished from the nucleobases; however, it was not so resolved to permit assigning the nucleotide sequence to the map. In many places, purines could be distinguished from pyrimidines; however, we could not unambiguously position the 60-mer ssDNA in our cryo-EM sample. An 11-mer ssDNA molecule (TCCAGATACAC) was constructed in COOT [100,101] and placed in density using its intrinsic real space refine function. In the lower resolution map E1 (6.24 Å), we observed density extending away from DnaB along the axis in which the 11-mer had been built (Supplementary Figure 5). This density quality did not permit the backbone to be resolved from nucleobase. However, model building suggested that an additional 11 nucleobases could explain this density. Since this density provided no unique nucleobase information, we built this segment as polyadenine.

As such, our final model contains a 22-mer of ssDNA. The extra 11 DNA bases visible in Map E1 were refined in COOT against this map. However, the complete 22-mer ssDNA was refined against two distinct maps. ssDNA residues 1-11 were refined against the high-resolution Map G, while residues 12-22 were refined against Map E1. The separately refined ssDNA segments were combined for visualization.

Inspection of the six composite DnaB nucleotide binding sites around the Walker A/P Loop motif (DnaB residues G233, K234, T235) revealed occupancy by six ATPγS molecules, each bound to a magnesium ion.

The Vc-DnaB-ssDNA- ATPγS model was refined with Phenix [102–109]. We used the 'real_space_refine' protocol, encompassing minimization global, morphing, NQH flips, and atomic displacement parameters (ADP). The refinement leveraged three rigid bodies (DnaB residues 1:171, 171:211, 212:468, 501 for each chain; ssDNA 1:11), Ramachandran, and secondary structure restraints. Refinement was carried out against the DeepEMhancer sharpened 3.37 Å density map G. A second round of real-space refinement encompassing minimization global, atomic displacement parameters (adp), NQH flips, with Ramachandran and secondary structure restraints completed the model (Supplementary Table 1). The final model includes Chain A (DnaB residues 22:461), chain B (DnaB residues 22:462), chain D (DnaB residues 23:463), chains C-E-F (DnaB residues 22:463), six ATPγS•Mg^{2+} complexes, one per chain (chains A-B-C-D-E-F residue 501) and ssDNA (chain G, residues 1-22).

Model Analysis and Visualization

Structural analysis and visualization of the Vc-DnaB-ssDNA complex were performed in the CCP4 software package [110], Coot [100,101], the Uppsala software suite [111–114], UCSF-CHIMERA [115], Phenix [102–109], PyMOL [116], Nucplot [117], and as described previously [44]. Distances and angles within and between protein structures were calculated using the PyMol Python scripts titled "pairwise_dist" (https://pymolwiki.org/index.php/Pairwise_distances) and "angle_between_domains" (https://pymolwiki.org/index.php/Angle_between_domains). Molecular graphics and figures were generated using UCSF-CHIMERA[115] and PYMOL [116]. The software used in this study was sourced from the SBGrid Consortium[118].

Data Availability

Coordinates for the EM-derived model of the Vc-DnaB-ssDNA-ATPγS complex are available from the RCSB Protein Data Bank under accession codes 9DLS. Cryo-EM maps are available from the EMBD under the accession code EMD-46984.

Funding

This work was supported by the National Science Foundation (DJ: MCB 1818255), and the Department of Education (NG: PA200A150068). The nMS work is supported by funding from the National Institutes of Health P41 GM109824 and P41 GM103314 to BTC. Some of this work was performed at the Simons Electron Microscopy Center and National Resource for Automated Molecular Microscopy located at the New York Structural Biology Center, supported by grants from the Simons Foundation (SF349247), NYSTAR, and the NIH National Institute of

General Medical Sciences (GM103310) with additional support from Agouron Institute (F00316), NIH (OD019994), and NIH (RR029300).

Acknowledgments

We thank the Jeruzalmi and Miggiano lab members, the City College biophysics group, the CUNY Advanced Science Research Center, and the New York Structural Biology Center for their scientific and technical advice. We also thank Professor Anuradha Janakiraman for excellent scientific discussions and technical assistance.

Conflicts of Interest

The authors have no financial or non-financial conflicts of interest.

1 ## Figures/Figure legends

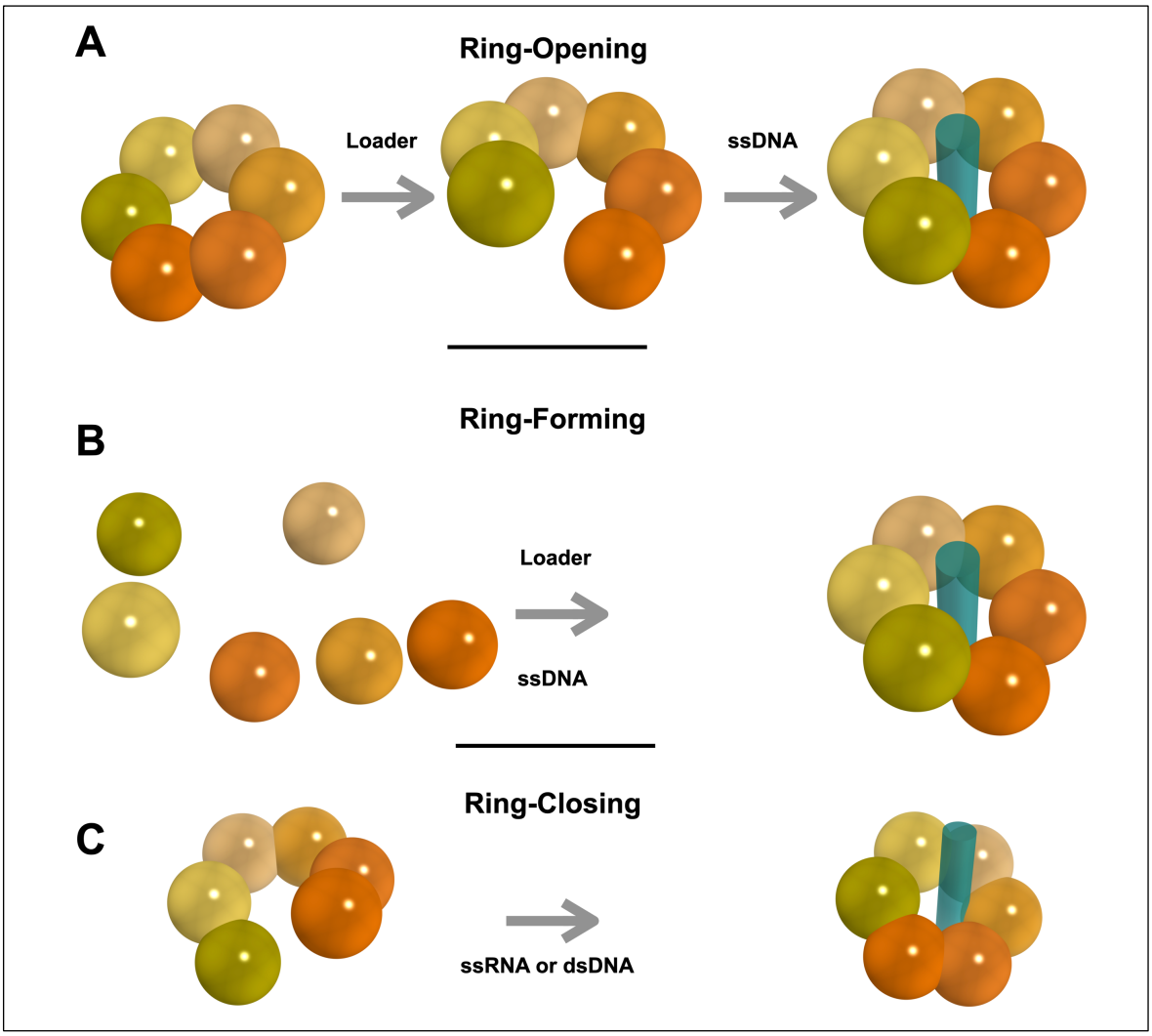

2 **Figure 1. Mechanisms of Helicase Loading.** Strategies used to load hexameric
3 helicases onto nucleic acid substrates are ring-opening, ring-forming, and ring-
4 closing [22,55,56]; the terms refer to the initial state of the helicase. In the ring-opening
5 scheme, closed ring hexamers are opened by helicase loaders and assembled on
6 ssDNA. The hexameric helicase is assembled on ssDNA from monomers in the
7 ring-forming scheme. Entry of the nucleic acid substrate and other factors mediate
8 the ring-closing scheme. Hexameric helicase subunits are represented as spheres
9 in shades of orange. For clarity, only the ATPase domains are shown. Nucleic
10 acid substrates are depicted as deep teal cylinders.

11

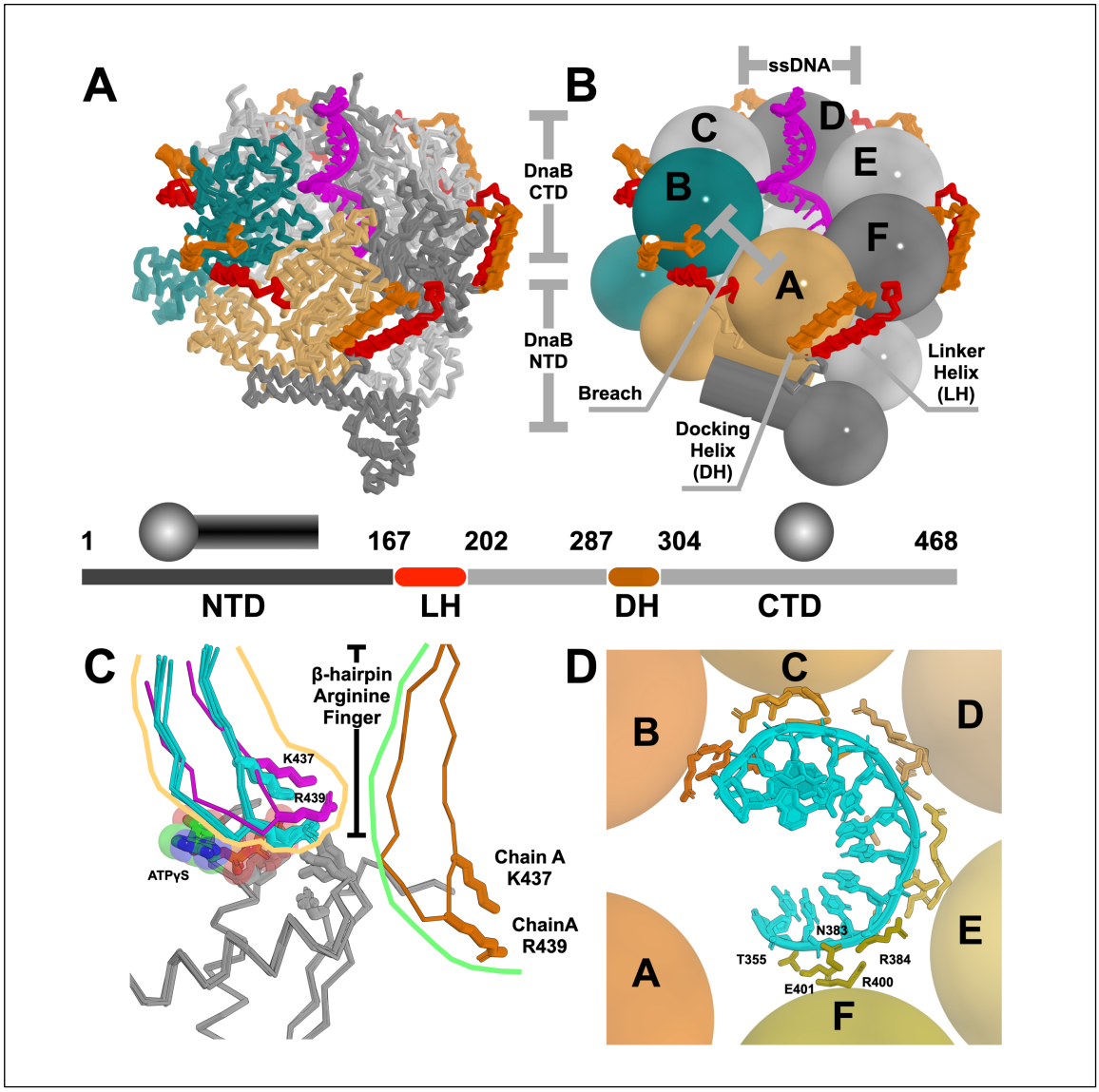

Figure 2. The Vc-DnaB-ssDNA-ATPγS Complex and its Interactions with Nucleotide and ssDNA. The Vc-DnaB-ssDNA-ATPγS is drawn in a ribbon representation (A) or a schematic using a design language wherein the NTDs are depicted as a mushroom shape and the CTDs as spheres. ssDNA, colored in magenta, is depicted in a cartoon and stick representation. The breach in the CTD layer is between chain A (deep teal) and chain B (light orange); other DnaB subunits are colored in alternating shades of gray. The Docking Helix (DH) and the Linker Helix (LH) are depicted as transparent cylinders colored orange and red, respectively. The primary sequence of Vc-DnaB is depicted as a bar, with the salient domain boundaries indicated. C) The six Vc-DnaB CTDs are depicted as

grey ribbons and are superimposed on the complete domain minus the DH element. The β-hairpin arginine fingers from all six adjacent CTDs are shown. Four chains (chains B, C, D, and E, cyan) superimpose closely, while chains F (purple) and A (brown) are found ~3 Å and ~19 Å, respectively, away from the Walker/P-loop lysine. D) Schematic representation of the Vc-DnaB-ssDNA interface. The DnaB CTDs are represented as spheres, labeled by chain, and colored in shades of yellow/orange. The ssDNA is drawn in a cartoon, with a stick representation and colored cyan. The protein side chains from one subunit (chain F) that contact ssDNA are shown in the stick representation, colored by chain as above, and labeled. The complete list of protein-DNA contacts appears in Supplementary Table 2. Additional details on the Vc-DnaB-ssDNA complex can be found in Supplementary Figures 5 and 6.

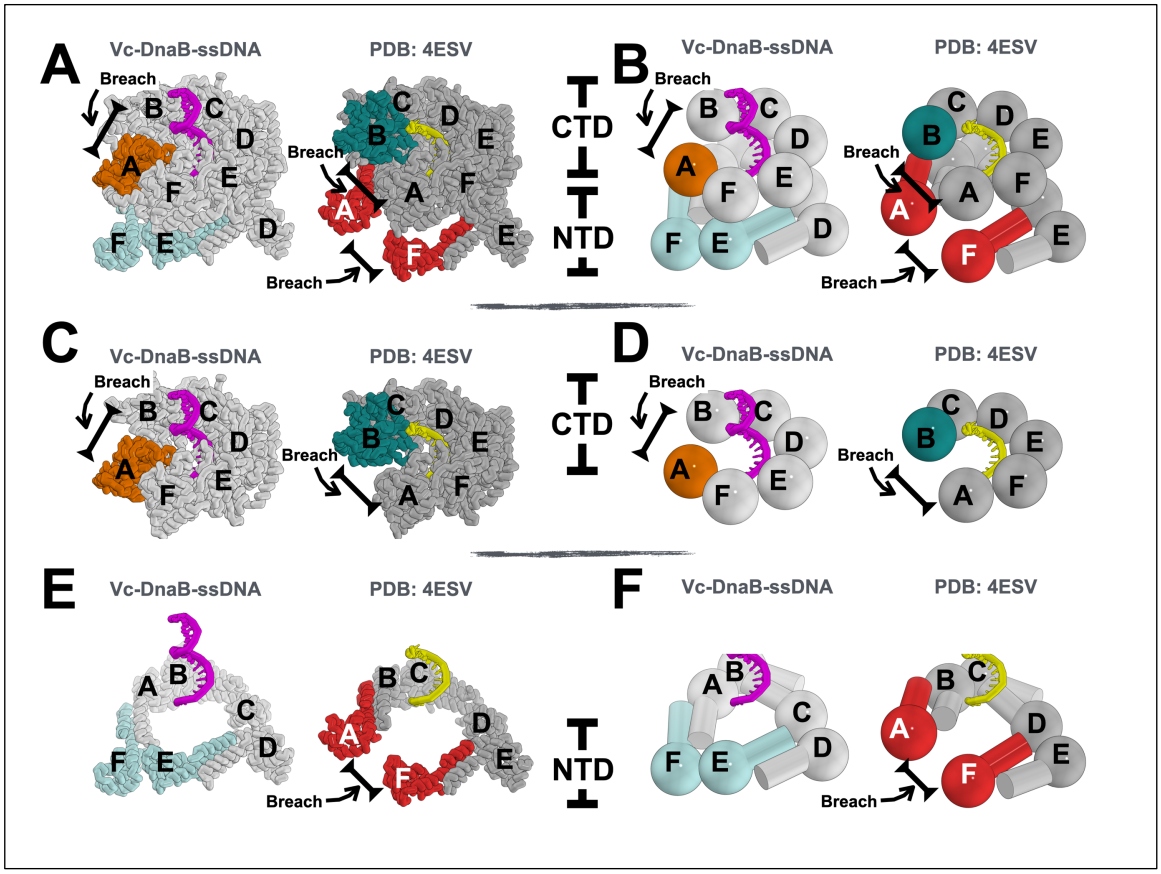

Figure 3. Nucleotide-Dependent Conformation-Switching between the Vc-DnaB-ssDNA-ATPγS and Bst-GDP•AlF$_4$ complexes. The two complexes are superimposed in all panels, as described in the main text. A) Ribbon representation of both complexes. Vc-DnaB NTD components chain F and E in the closed planar and triangular configuration are colored in pale cyan. Bst-DnaB NTD components chain A and F in the open spiral configuration are colored in red. Vc-DnaB chain A is colored orange. 4ESV chain B is colored deep teal. The ssDNA in the Vc and Bst complexes are drawn in the cartoon and stick representation and colored purple and yellow, respectively. All other chains of DnaB are colored in light gray (Vc) and dark gray (Bst). The breaches in the NTD and CTD layers are indicated. Chains corresponding to the NTD and CTD components are labeled. B) The depiction is identical to that in panel A, except that the NTD and CTD layers are represented using the sphere and mushroom-like shape design language. C) The exact representation as panel A, except that only the CTD layer is shown. D) Identical depiction as panel C except that the

DnaB CTD layers are depicted as spheres. E) The exact representation as panel A, except that only the NTD layer is shown. F) Identical depiction as panel E except that the DnaB NTD layers are depicted using mushroom-like shapes.

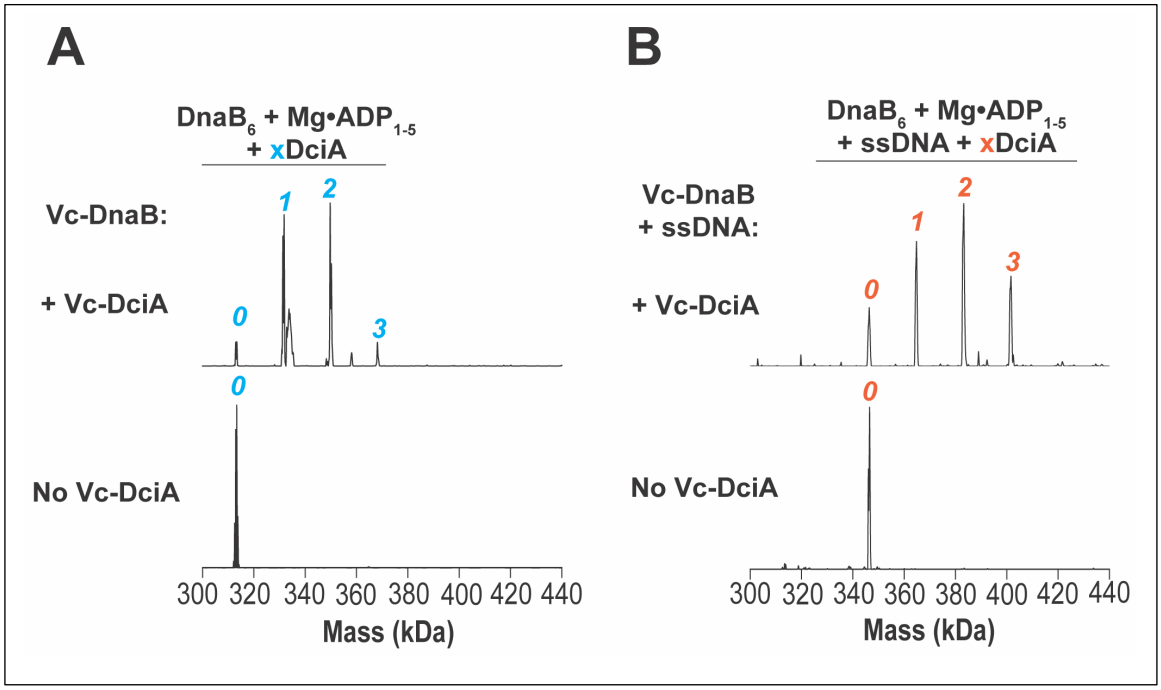

Figure 4. Up to Three Copies of Vc-DciA Bind to Isolated Hexameric Vc-DnaB and Vc-DnaB Complexed to Replication Origin-Derived ssDNA. The stoichiometry of reconstituted assemblies of Vc-DnaB, Vc-DciA, and origin-derived ssDNA. Deconvolved nMS spectra of 10 μM Vc-DnaB (measured as the monomer) without and with 7 μM full-length Vc-DciA (A) and in the absence or presence of 3 μM origin-derived ssDNA (O4-Vc-F) (B). The number of Vc-DciA molecules observed bound to Vc-DnaB are indicated in blue (A) or red (B). The expected masses include $DnaB_6$ = 311.5 kDa, DciA = 18.4 kDa, and ssDNA = 32.5 kDa. All samples were exchanged into 10 μM ATP, 500 μM magnesium acetate, 500 mM ammonium acetate, and 0.01% Tween-20 before nMS analysis.

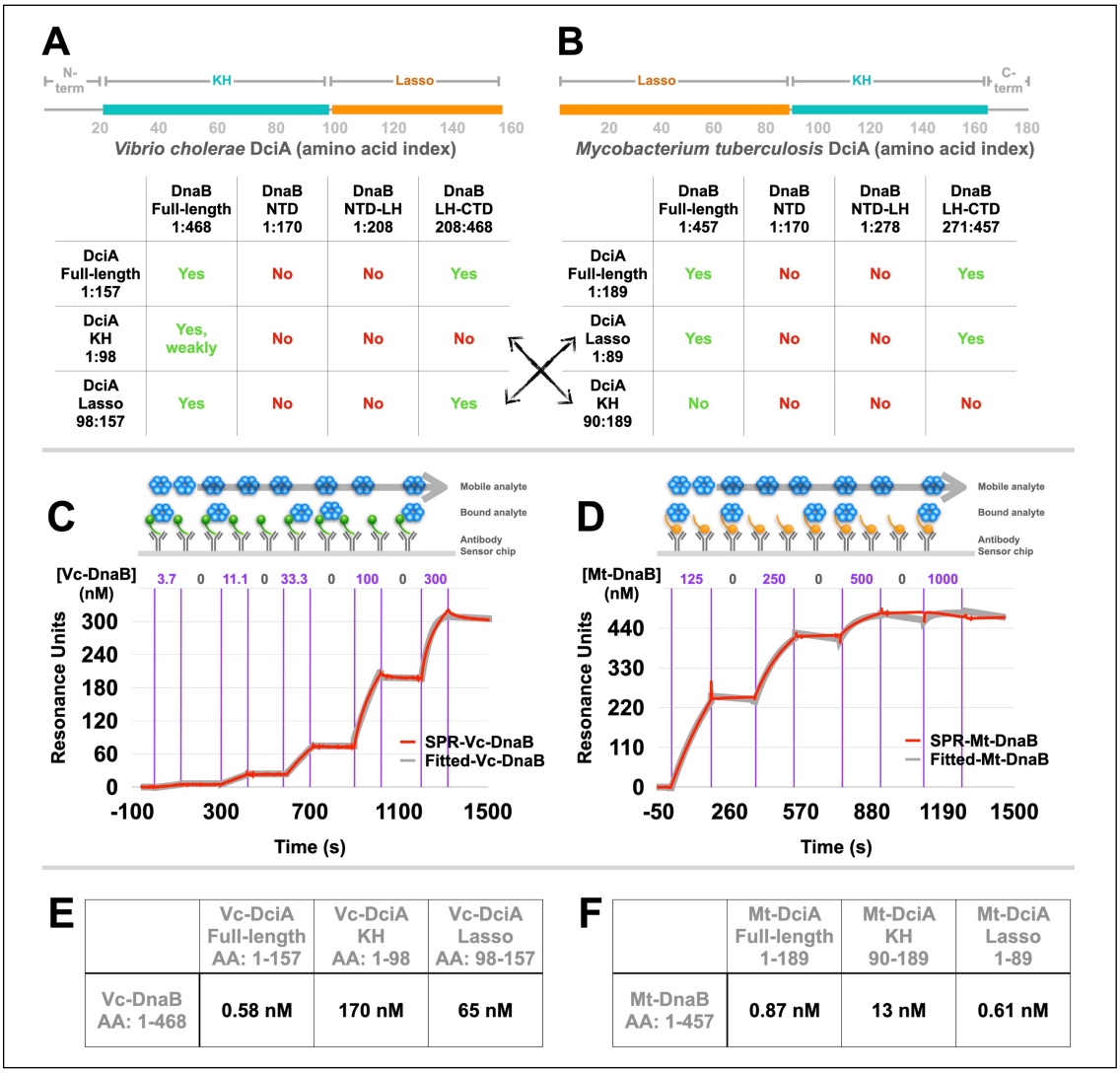

	DnaB Full-length 1:468	DnaB NTD 1:170	DnaB NTD-LH 1:208	DnaB LH-CTD 208:468
DciA Full-length 1:157	Yes	No	No	Yes
DciA KH 1:98	Yes, weakly	No	No	No
DciA Lasso 98:157	Yes	No	No	Yes

	DnaB Full-length 1:457	DnaB NTD 1:170	DnaB NTD-LH 1:278	DnaB LH-CTD 271:457
DciA Full-length 1:189	Yes	No	No	Yes
DciA Lasso 1:89	Yes	No	No	Yes
DciA KH 90:189	No	No	No	No

E

	Vc-DciA Full-length AA: 1-157	Vc-DciA KH AA: 1-98	Vc-DciA Lasso AA: 98-157
Vc-DnaB AA: 1-468	0.58 nM	170 nM	65 nM

F

	Mt-DciA Full-length 1-189	Mt-DciA KH 90-189	Mt-DciA Lasso 1-89
Mt-DnaB AA: 1-457	0.87 nM	13 nM	0.61 nM

Figure 5. Although featuring distinct arrangements, the Vc and Mt-DciA loaders display comparable affinity to their cognate DnaB helicase. A) The primary sequence of Vc-DciA is arranged as a bar, and the locations of the KH and Lasso domains are indicated. The table below summarizes the NiNTA 'pull-down' experiments, wherein the green 'yes' and red 'no' indicate that the pull-down assay was scored to report binding or no binding, respectively (Supplementary Figure 15). B) Same as panel A except that the image and table capture studies with Mt proteins (Supplementary Figure 16). Strikingly, although the KH and Lasso domains in the two DciA orthologs feature an inverted arrangement, the Lasso domains of each specify binding to the LH-CTD construct of DnaB. The dissociation constants (K_D) between DnaB and DciA were evaluated through

single-cycle kinetic analyses *via* Surface Plasmon Resonance (SPR). On and off rates of full-length DnaB at incremental concentrations (Vc: 3.7, 11.1, 33.3, 100, 300 nM; Mt: 125, 250, 500, 1000) were measured by immobilizing cognate C-term His-tagged full-length DciA, from Vc (C; K_D = 0.59 nM; Chi^2 = 4.33; R_{max} = 312.3) and Mt (D; K_D = 0.87 nM; Chi^2 = 11.8; R_{max} = 487.8) on the SPR sensor chip. A schematic of the SPR experiment accompanies the raw (in red) and fitted (in grey) SPR curves. Experimental data were fit as described in the methods. The same approach was applied to measure K_Ds for the KH and Lasso constructs (Supplementary Figures 17 and 18). The K_D values emerging from the SPR analysis are summarized for the Vc (E) and Mt (F) systems.

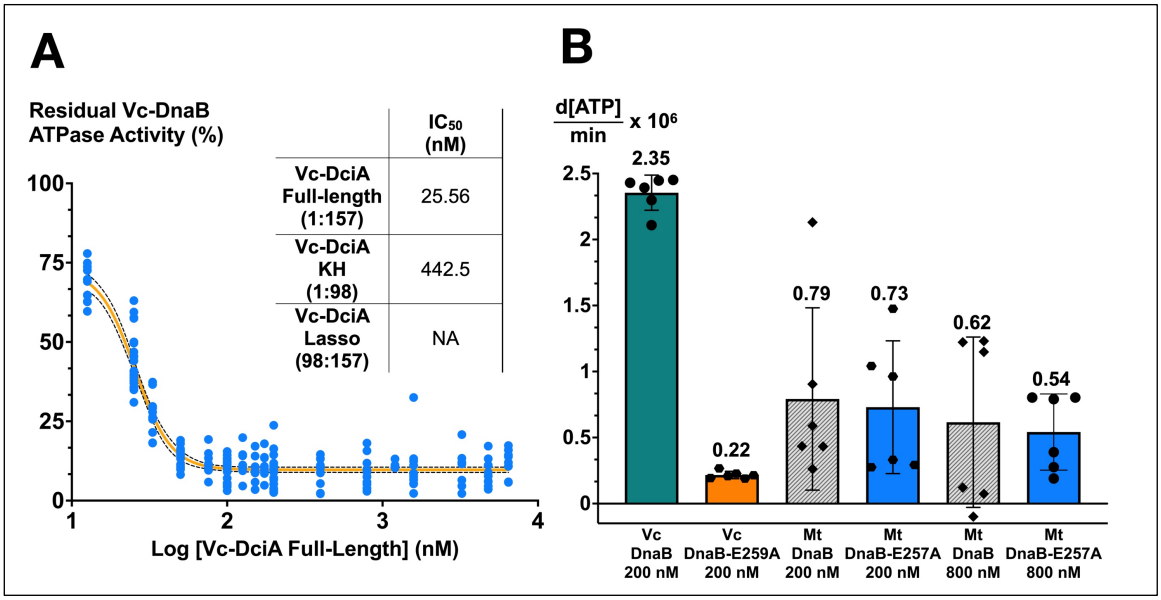

Figure 6. Vc-DnaB ATPase activity is suppressed by cognate full-length loader; Mt-DnaB is inactive. A) The effect of titrating Vc-DciA (0 - 6400 nM, log scale) on the residual ATPase activity of Vc-DnaB (200 nM) is plotted. For each experiment, the residual activity is the quotient of the ATPase rate of a particular DciA concentration and the rate for 0 nM DciA. The blue points represent seven experiments with different batches of Vc-DnaB and Vc-DciA on various days measured in triplicate. The light-orange line represents the non-linear fit of the residual activity points (Sigmoidal, 4PL, X is log (concentration) model in Prism. The dotted lines represent the 95% confidence interval. The fit encompassed 210 points, showed an R^2 value of 0.91, and produced an IC_{50} value of 25.56 nM (95% CI = 23.74 to 26.94 nM). Parallel analysis with the KH domain on four different batches revealed a 16-fold higher IC_{50} = 442.5 nM (R^2 = 0.9693: 95% CI: 380.5 to 520.0 nM). The Lasso domain was not found to inhibit; however, we observed activation of DnaB's ATPase at very high Lasso concentrations. The inset table summarizes the IC_{50} results. Control measurements with the E259A Vc-DnaB Walker B mutant exhibited no ATPase activity (panel B, orange). B) Investigation of the ATPase activity of Mt-DnaB. The ATPase rates for wild-type hardly exceed that measured from the Walker B mutant Mt-DnaB. The rate for 800 nM is lower than 200 nM Mt-DnaB. We conclude that Mt-DnaB, under the assay conditions, is not active. Positive (200 nM Vc-DnaB) and negative controls (200 nM Vc-DnaB-

E259A) provide context for results with Mt-DnaB. Each experiment in panel B was performed NN times in triplicate. The points represent the measured rates; The height of the bar represents the average of the measured points; The vertical bracket visually represents one standard deviation. Vc proteins are colored in deep teal and orange. Mt proteins are in blue and grey.

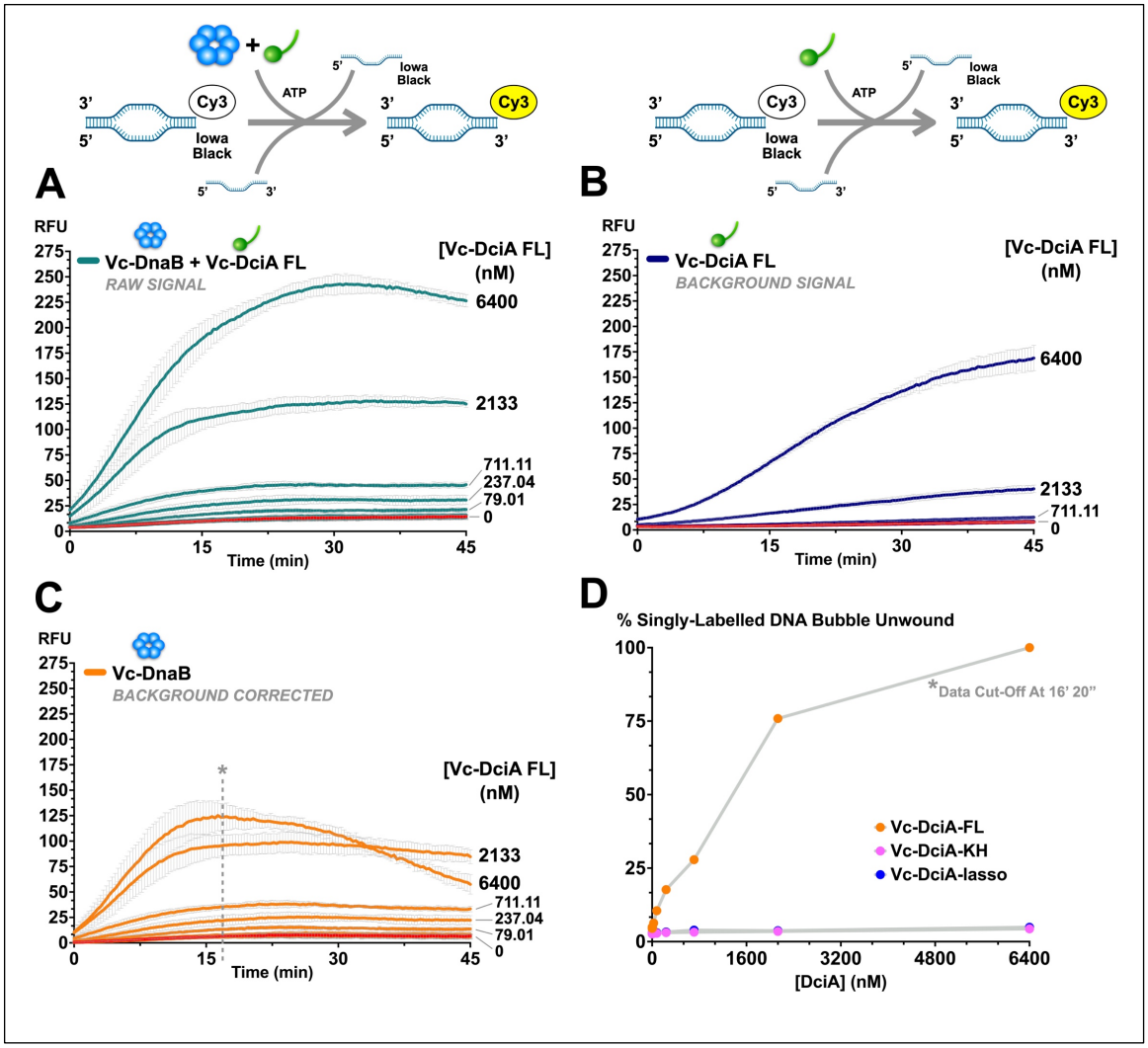

Figure 7. Vc-DnaB is loaded onto a physiological DNA bubble substrate by the full-length Vc-DciA loader. Helicase loading was measured using a DNA substrate that mimics unwound DNA at a replication origin as is diagrammed in the schematic above. A) Loading of full-length Vc-DnaB by full-length Vc-DciA. Loading is read out by measuring fluorescence (in relative fluorescence units, RFU) over 45 minutes at 570 nm from a DNA substrate after it had been unwound by DciA-loaded DnaB to relieve quenching. Data were taken by titrating Vc-DciA-FL (0.11-6400 nM) against Vc-DnaB (200 nM). Each labeled curve represents the average of 6 independent measurements taken from different batches of proteins on different days. The lack of loading activity in the curve that omits Vc-DciA (red curve) implies that DnaB's self-threading activity has been suppressed with the replication-origin mimicking DNA bubble substrate. The standard deviation of each

point is plotted in light gray. B) Same as Panel A except that Vc-DnaB is omitted. Envisioned as a control, this measurement teaches that Vc-DciA appears to have the capacity to unwind bubble DNA on its own. C) Point-by-point subtraction of the curves in panels A and B estimates the bubble unwinding signal that arises solely from Vc-DnaB. The downward phase of the 6400 nM DciA curve after 16 minutes arises from unwinding rate differences between Vc-DnaB and Vc-DciA. These data suggest that Vc-DciA stimulates the loading of Vc-DnaB by 25-fold (~5 to ~125 RFU). D) The unwinding data in panel C is converted to a percentage unwound by dividing by the maximum RFU point and plotting the resulting values against Vc-DciA concentration. Parallel measurements reveal that the isolated Vc-DciA KH and Lasso domains (Supplementary Figure 27A and 27B) exhibit little (less than 5%) to no loading activity.

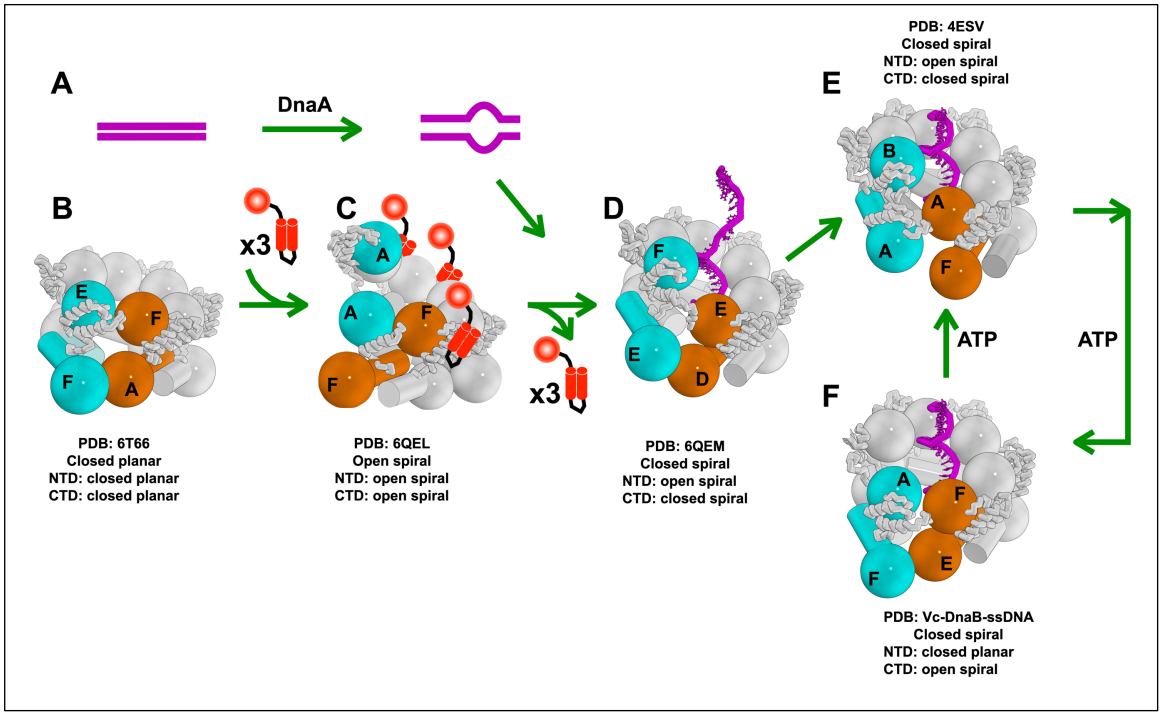

Figure 8. Model for Loading of DnaB by DciA and Translocation of DnaB on ssDNA. A) The DnaA protein binds to the replication origin and promotes melting into a DNA bubble.

B) The hexameric closed planar DNA-free Vc-DnaB (PDB: 6T66[12]) provides a ground state model. C) Our data suggests that up to 3 DciA loaders (red) bind to Vc-DnaB; we suggest that DnaB adopts an open spiral configuration analogous to that seen with the DnaC/λP complexes [19,43,44,48]. D) Remodeling of this complex accompanies the entry of DnaA-generated ssDNA into the central chamber of DnaB. We suggest translocating DnaB populates the two states captured in the ATPγS (E) and GDP•AlF_4 (F) DnaB conformations. Upward migration (E) by 25 Å of cyan CTD chain A in (E, black arrow) to the position in (F) represents the first translocation step. Migration is accompanied by NTD reconfiguration from the closed planar (E) to the open spiral (F). In the second step, orange CTD chain A in (F, black arrow) migrates upward by 25 Å to the position in (E). In this step, the NTD closes back to the closed planar configuration. Repetition of these two steps around the DnaB enables each subunit to translocate. We suggest that the loader DnaB-ssDNA complex, which resembles the GDP•AlF_4 conformation, enters this cycle by transitioning to the ATPγS state. The DnaB models in panels B-F are

colored in white except for certain blue and orange CTDs and NTDs that line the various breaches, except for the closed planar entity.

Supplementary Information

Assembly of Hexameric Helicases on Nucleic Acid Substrates

Cells apply three broad strategies to load hexameric helicases onto nucleic acid substrates: ring-opening, ring-forming, and ring-closing [22,55,56]; the terms refer to the initial state of the helicase. These schemes encompass loading onto ssDNA, ssRNA and dsDNA. In the ring-opening scheme, closed ring hexamers, e.g., *E. coli* DnaB, are opened by helicase loaders, such as *E. coli* DnaC [18–20] or phage λP[43,44,48] and assembled on ssDNA formed at the cognate replication initiator – origin DNA complex. In the ring-forming scheme, the hexameric helicase is assembled on ssDNA from monomers, either spontaneously as with the LT-antigen or E1 helicases or through the activity of a helicase loader such as DnaI, which loads the DnaB family helicase in *B. subtilis* [34,119]. The ring-closing scheme is observed with the bacterial Rho and the eukaryotic MCM2-7 hexameric replicative helicases (reviewed in [22,55,56]). In the Rho helicase, ring closure is mediated by the entry of the nucleic acid substrate. In the MCM2-7 ensemble, dsDNA is deposited via the chaperone origin recognition complex and associated factors. The scheme(s) the DciA loader uses to assemble DnaB onto the origin-DNA is unknown.

Vc-DnaB Primarily Contacts the Phosphate Backbone of ssDNA

Vc-DnaB subunits use seven residues (Asn353, Thr355, Asn383, Arg384, Arg400, Glu401, and Gly403) to contact the ssDNA backbone, though not every chain uses every residue; one contact is seen to contact a nucleobase (chain D Asn353 and N2 of G5). The segment of ssDNA within DnaB's central chamber is arranged with 11-12 nucleotides per turn of ssDNA and a pitch of ~32 Å, a value that compares well with the pitch (~33.4 Å) displayed by the DnaB CTD spiral. The

approximate match in pitch between protein and ssDNA spirals implies that corresponding DNA binding residues on each subunit make equivalent contacts with the ssDNA backbone[10] (Supplementary Figure 6 and Supplementary Table 2).

Divergent Solution Architecture of the DciA Helicase Loader

To understand the divergent solution architecture predicted by Alphafold for Vc and Mt DciA (Supplementary Figure 28), we performed limited proteolysis mass spectrometry (MS) and native MS. Our proteolysis study encompassed two enzymes (Trypsin and Asp-N) with distinct substrate preferences (Supplementary Figures 12A and 12B). MS analysis of the proteolysis products revealed a series of cuts (red and magenta dots) that were concentrated on the Lasso regions of both DciA orthologs; in contrast, recognition sites for both proteases on the KH domains (gray dots) were protected from proteolysis. These data support the predicted inverted KH-Lasso arrangement in Vc and Mt DciA. We also showed using native MS that both DciA orthologs are monomeric in solution and do not bind ATP (Supplementary Figures 12C and 12D).

Vc-DciA Stimulated Unwinding by Vc-DnaB Measured Using a Replication Fork-Mimic

Every bacterial helicase loader stimulates the DNA unwinding activity of its cognate DnaB helicase. To investigate the influence of DciA on cognate DnaB, we applied an ensemble FRET-based DNA unwinding assay wherein a DNA replication fork mimicking substrate [20] is fitted with a Cy3 labeled nucleobase Watson-Crick-Franklin paired with a nucleobase conjugated to the BHQ2 quencher; the unwinding of the fork substrate is readout by recording appearance of a fluorescent light signal at 570 nm (Supplementary Figure 21). This assay

showed that 200 nM Vc DnaB exhibited measurable albeit low DNA unwinding activity. However, titration of full-length Vc DciA (0.11 to 6400 nM) revealed a 10-fold (15 to 150) increase in fluorescence at the highest concentration (6400 nM) (Supplementary Figure 21B). Unwinding depended on ATP and was wholly absent in Vc DnaB Walker B mutant E259A (Supplementary Figure 22). Parallel analysis of the isolated DciA KH and Lasso domains implied retention of about 30% of the activity of the full-length Vc-DciA to activate the helicase. (Supplementary Figures 21B and 23).

Vc-DciA Stimulated Unwinding by Vc-DnaB Measured Using a Doubly Labeled DNA Bubble Substrate

The bubble DNA substrate (Figure 7 and Supplementary Figure 25), in principle, permits the loading of DnaB onto both single strands, leading to unwinding in both directions; however, the bubble substrate above with the single FRET pair only reports on activity at one end of the DNA. To examine activity at both ends, we repeated the helicase loading assay with a bubble substrate that featured the above FRET pairs at both termini. Full-length DciA and the two truncated constructed displayed the same pattern of activity as seen with the singly labeled substrate (Supplementary Figures 25, 27C, and 27D). Full-length DciA produced 10% more fluorescence on the doubly labeled substrate instead of the expected doubling of the signal. This discrepancy may be due to unexpected quenching between the two ends of the molecule due to conformational switching that brings them closer together. Alternatively, loading two DnaB molecules may be more complex than previously thought.

Comparison to other structures of Vc-DnaB

We compared our cryo-EM Vc-DnaB structure to three previously determined crystal structures: 6T66, 7QXM, and 8A3V. None feature ssDNA (6T66, 7QXM), and one includes DciA at a 6:6 ratio with DnaB (8A3V). We compared the structures for subunit proximity, ring breaches, nucleotide occupancy, disposition of the β-hairpin/arginine finger, and LH position.

The 6T66 structure [12] presents as a planar hexamer in the crystallographic asymmetric unit with a dilated NTD layer and a constricted CTD tier (Supplementary Figure 29A). The DnaB subunits in this structure are labeled A-B-C-D-E-F, counterclockwise down the CTD axis. Two of the CTDs (A – F: 35.1 Å and D – E: 36.4 Å) are 2-3 Å further away from their neighbors than the disposition of other subunit pairs (A – B: 32.8 Å; B – C; 32.7 Å; C – D: 32.7 Å; E – F: 33.1 Å), implying two breaches in the CTD layer; the NTD layer is unbreached. In the Vc-DnaB-ssDNA complex, chain A, at the bottom of the spiral, is further away (A – B: 39.6 Å; A – F: 34.6 Å) from its neighbors than other pairs (average: ~33.4 Å). The significance of two breaches in non-consecutive subunits in the CTD tier in the 6T66 structure remains to be understood.

The nucleotide-binding site of each subunit in 6T66 is populated with GDP•AlF_4/Mg^{2+}. However, the β-hairpin/arginine finger elements that complete these binding sites populate three positions. The distance between the P-loop lysine 234 and arginine finger 439 at the sites between chains D to E (18.7 Å) and A to F (16.0 Å) is considerably longer than the corresponding values for other subunit pairs (A – B: 10.9 Å; B – C: 11.2 Å; C – D: 11.1 Å; E – F : 11.3 Å). Naturally,

longer distances are seen in CTDs that are further apart (Supplementary Figure 29C).

We next examined the positions adopted by the LH element in the 6T66 hexamer. Alignment of the CTD onto the chain A CTD, but omitting the DH and LH elements from the calculation (resid 204:465 and not (resid 287:304 or resid 178:205)) produces an average RMSD = 0.74 Å. In this alignment, the LH elements populate two positions (LH1 and LH2 above). The LH elements from chains A and E populate positions closely related to LH2; the rest are seen in the LH1 position (Supplementary Figure 29D). The subunit pairs with divergent dispositions and arginine fingers populate the LH2 position; the rest are in LH1.

The 7QXM Vc-DnaB crystal structure features a planar hexamer in the asymmetric unit and is unliganded [13]. The DnaB subunits in this structure are labeled A-F-E-D-C-B, counterclockwise down the CTD axis. The NTD layer is dilated and follows NTD layers from 6T66 and the Vc-DnaB-ssDNA complex. The CTD layer is constricted, with individual CTD further away from each other than in 6T66 or the Vc-DnaB-ssDNA complex (A – B: 33.7 Å; B – C: 37.0Å; C – D: 33.7 Å, D – E: 36.3; E – F: 33.6 Å; F – A: 37.9 Å). Likewise, the P-loop lysine to arginine finger distances is variable (A – B: 21.1 Å; B - C: 16.8 Å; C – D: 20.4 Å, D – E: 15.7 Å; E – F: 20.9 Å; F – A: 17.3 Å). The observed variability in the disposition of CTDs in 7QXM may reflect the underlying lack of nucleotide to organize and stabilize inter-CTD contacts via the β-hairpin arginine finger. The LH elements in 7QXM populate two positions, LH2 (Chains B, D, and F) and another position (Chains A, C, and E), which are unique to this structure.

The 8A3V Vc-DnaB-DciA crystal structure has two DnaB subunits and two DciA molecules in the crystallographic asymmetric unit[14]. Applying crystallographic symmetry generates a 6:6 DnaB: DciA entity, revealing a dilated NTD layer and a constricted CTD layer. The nucleotide site of each Vc-DnaB CTD is filled with ADP. In the Vc-DnaB$_2$:Vc-DciA$_2$ asymmetric unit, the inter-CTD distance is ~32 Å, and the P-loop to arginine finger distance is 12.3 Å. The LH elements in 8A3V occupy the LH1 position.

Although parallels could be drawn between the 6T66, 7QXM, and 8A3V structures and the present Vc-DnaB-ssDNA structure, additional studies will be required to sequence them precisely in the reaction coordinate.

Structural Comparisons to *E. coli* DnaB-ssDNA Complexes

The RCSB PDB includes four unpublished entries corresponding to *E. coli* DnaB-ssDNA structures (PDB: 7T20, 7T21, 7T22, and 7T23[62,120–122]). One structure was determined with the ATP analog AMP-PNP (7T20); the others harbor the ADP•AlF$_4$ transition state analog (7T21, 7T22, and 7T23). The ATP analog structure maps closely to the Vc structure, while the ADP•AlF$_4$ transition state DnaB structures map to the Bst complex. As such, conclusions made from comparisons between the Vc and Bst structures are fully compatible with the *E. coli* structures.

Supplementary Figures

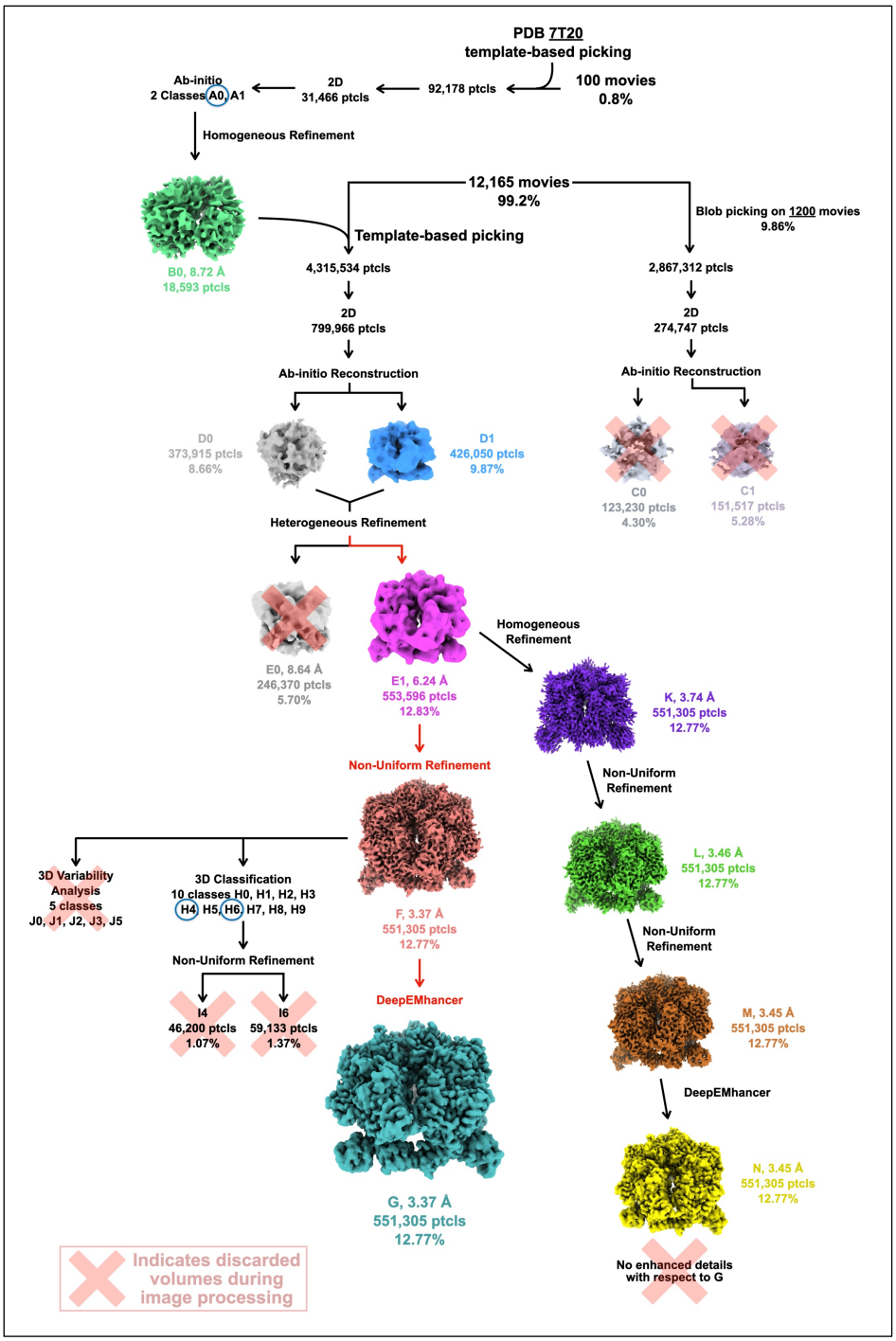

Supplementary Figure 1. Workflow Steps in the Processing of cryo-EM Data for the Vc-DnaB-ssDNA-ATPγS complex. Workflow steps are described in the Methods section. The percentages reported alongside the volumes are calculated against the number of starting picked particles. The various volumes/maps in the

workflow are depicted with unique colors. Map G represents the highest quality map we obtained, against which the atomic model was built and refined. The extended length of ssDNA was built into map E1.

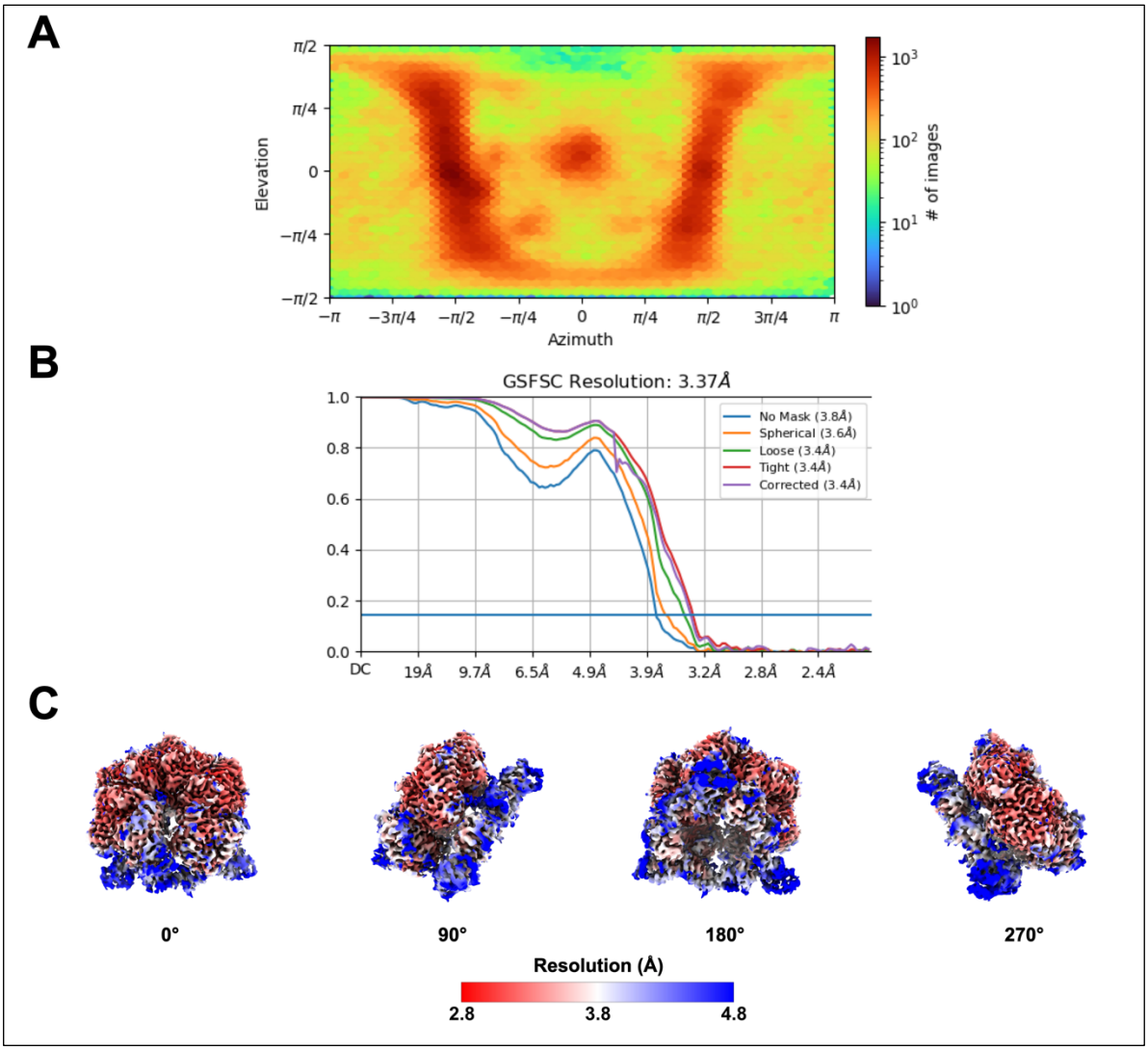

Supplementary Figure 2. Statistics Fourier Shell Correlation, and Local Resolution. A) CryoSPARC Plot of particles' azimuthal and elevation angles in the 3.37 Å reconstruction of Vc-DnaB-ssDNA-ATPγS. The blue-to-red scale describes the number of particles, from 10^0 to 10^3. The red clusters represent the preferred orientation of the particles in our data set; however, this distribution of particles did not impact the quality of the map reconstruction. B) Fourier Shell Correlation (FSC) plots taken from the non-uniform refinement job that produced the map G. Plots were generated by applying no mask, spherical mask, loose mask, tight mask, and corrected mask on the protein-DNA complex. The corrected tight mask plot shows a resolution of 3.37 Å at FSC = 0.143. C) The Vc-DnaB + ssDNA EM density map is colored (red: 2.8 Å to blue: 4.8 Å) according to the local

resolution. The density map is depicted in four poses that differ by rotations of 90° along the Y axis.

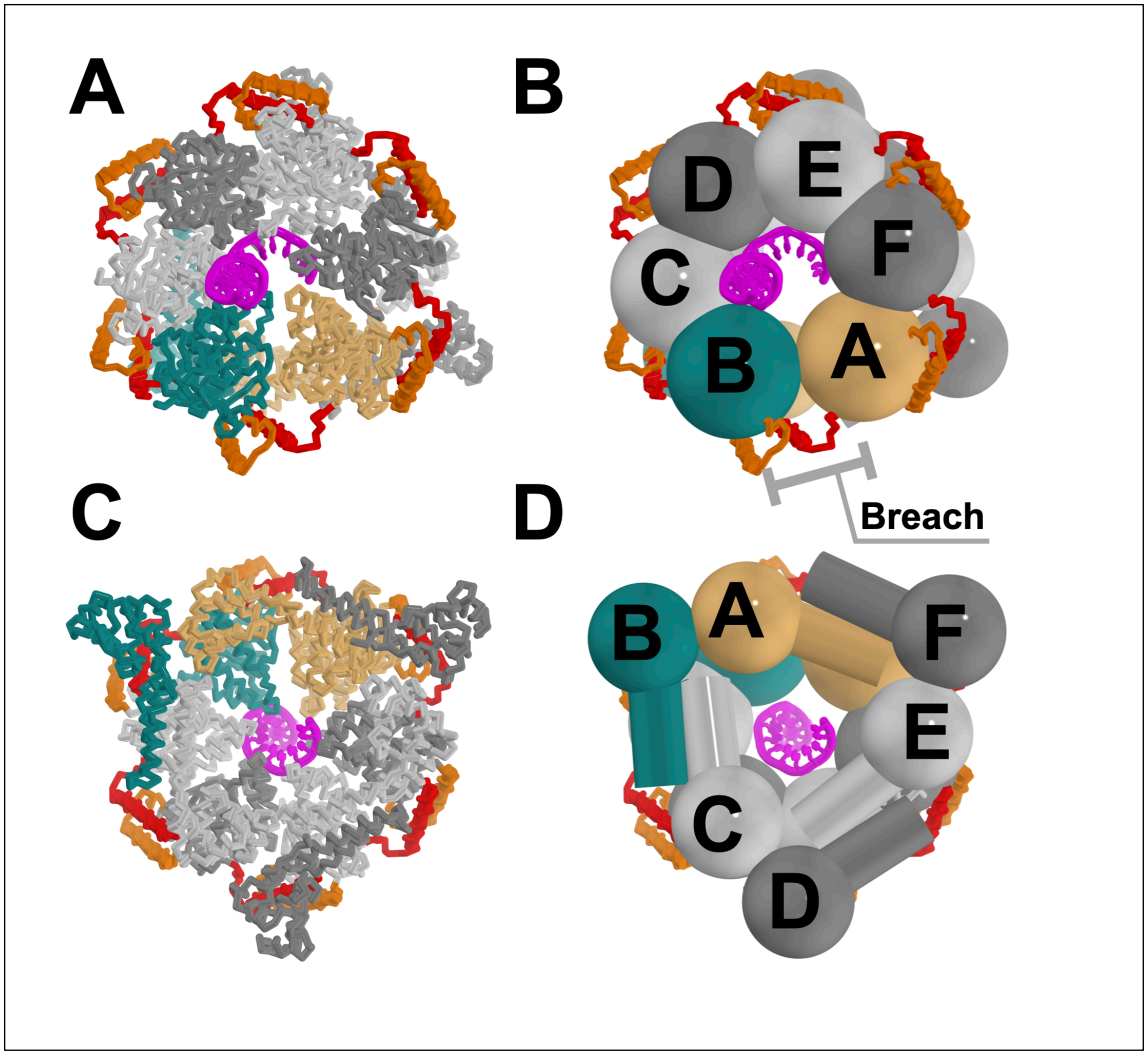

Supplementary Figure 3. The Vc-DnaB-ssDNA-ATPγS Complex. The Vc-DnaB-ssDNA-ATPγS is drawn in a ribbon representation (A or C) or a schematic using a design language wherein the NTDs are depicted as a mushroom shape and the CTDs as spheres (C or D). ssDNA, colored in magenta, is displayed in a cartoon and stick representation. The breach in the CTD layer is between chain A (deep teal) and chain B (light orange); other DnaB subunits are colored in alternating shades of gray. The Docking Helix (DH) and the Linker Helix (LH) are depicted as transparent cylinders colored orange and red, respectively. The pose in panels A and B is along the path of DNA. Panels C and D are in a pose that is rotated approximately 180° from that in panels A and B.

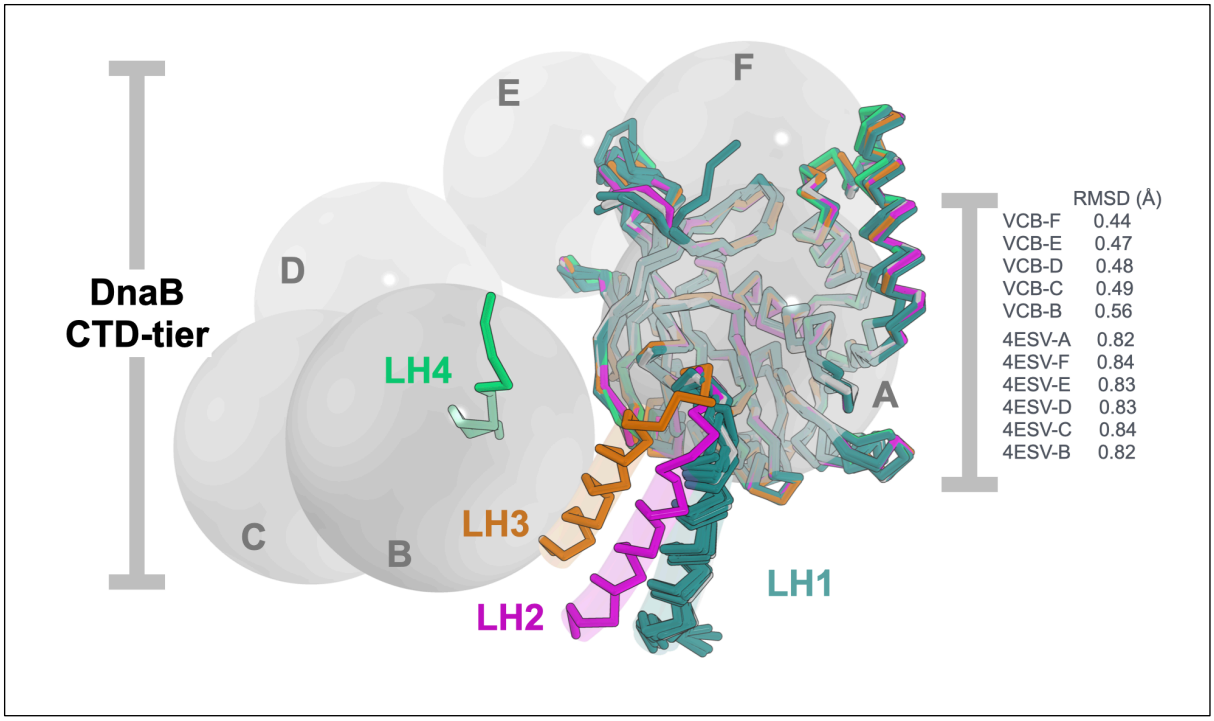

Supplementary Figure 4. The DnaB Linker Helix (LH) Element is a Moving Part During Translocation on ssDNA. Superposition analysis of the VC ATPγS and GDP•AlF_4 structures reveals that the LH element of DnaB occupies at least four positions, termed LH1, LH2, LH3, and LH4). The CTDs (total of 11) of the Vc and Bst structures were superimposed on residues 204:465 of Vc chain A (residues corresponding to the LH 178:205 or DH 287:304 elements were omitted from the calculation). The four positions of the LH are colored in deep teal (LH1), magenta (LH2), orange (LH3), and lime-green (LH4). Except for chains A (LH3) and F (LH2), the Vc DnaB chains populate the LH1 position. Chain A of the Bst-4ESV structure populates the LH4 position; the others are seen in the LH1 position. The CTD layer of the Vc structure is shown as labeled spheres drawn at the centers of mass of each CTD. The superimposed CTDs are drawn in the ribbon representation, and the transparent cylinder indicates the LH.

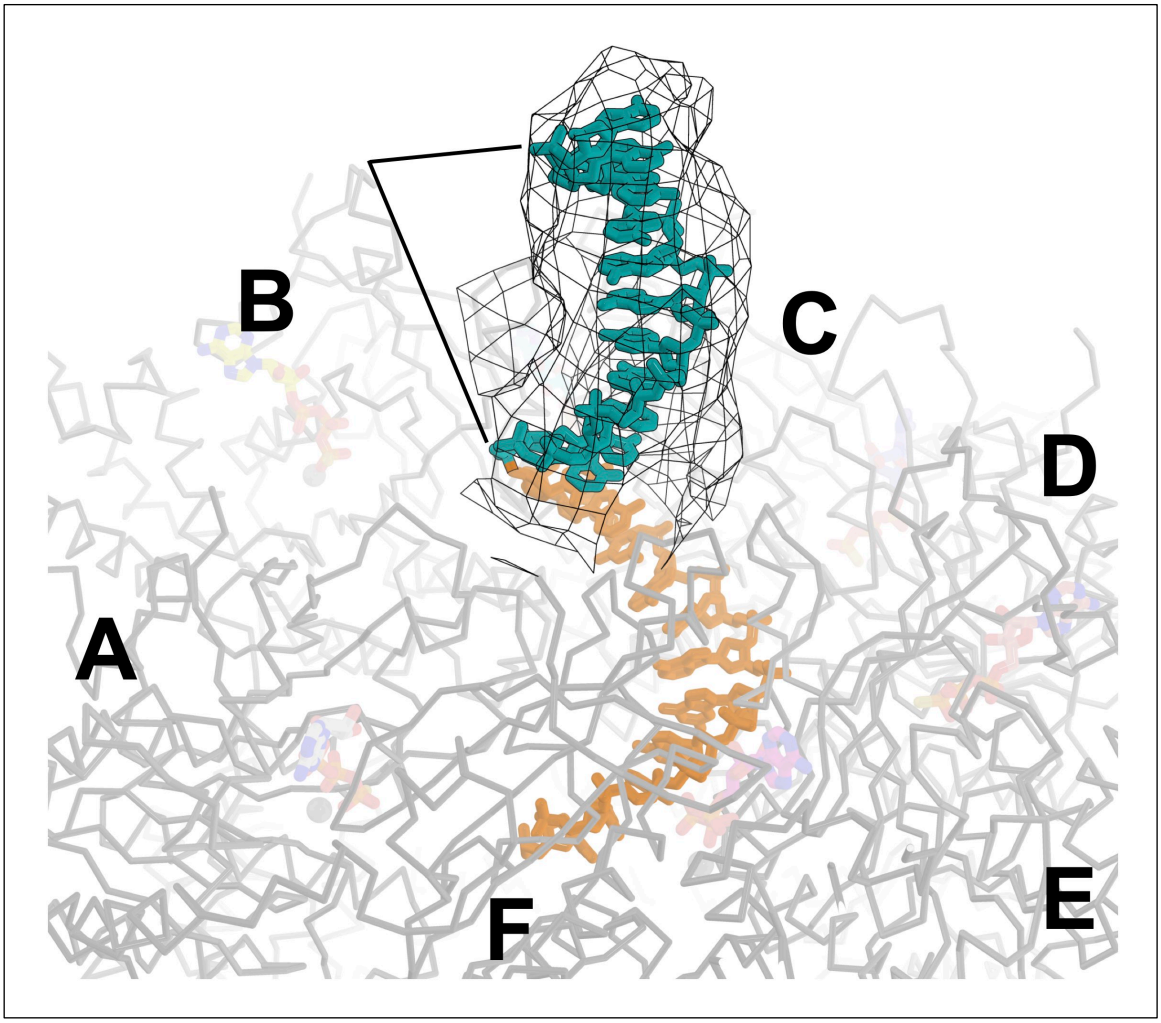

Supplementary Figure 5. 11 additional ssDNA positions outside the confines of Vc-DnaB are seen in the cryo-EM density map. Close inspection of the 6.24 Å map E1 (Methods and Supplementary Figure 1) enabled an ssDNA model to be constructed that was 11 positions longer than that seen in map G. The map into which this segment was built is shown as a mesh (isomesh level: 2.5). The extra positions are colored in teal; the ssDNA built into map G are colored orange. Vc-DnaB is represented as a grey ribbon, and each monomer is labeled by chain (A-B-C-D-E-F). For reference, the six ATPγS and six Mg^{2+} atoms are displayed as sticks and spheres, respectively, applying transparency. As noted in the methods, neither Map G nor Map E1 was sufficiently resolved to permit the assignment of parts of the input 60-mer sequence to the map. As such, the sequence in our final model was built as follows: TCCAGATACACAAAAAAAAAA.

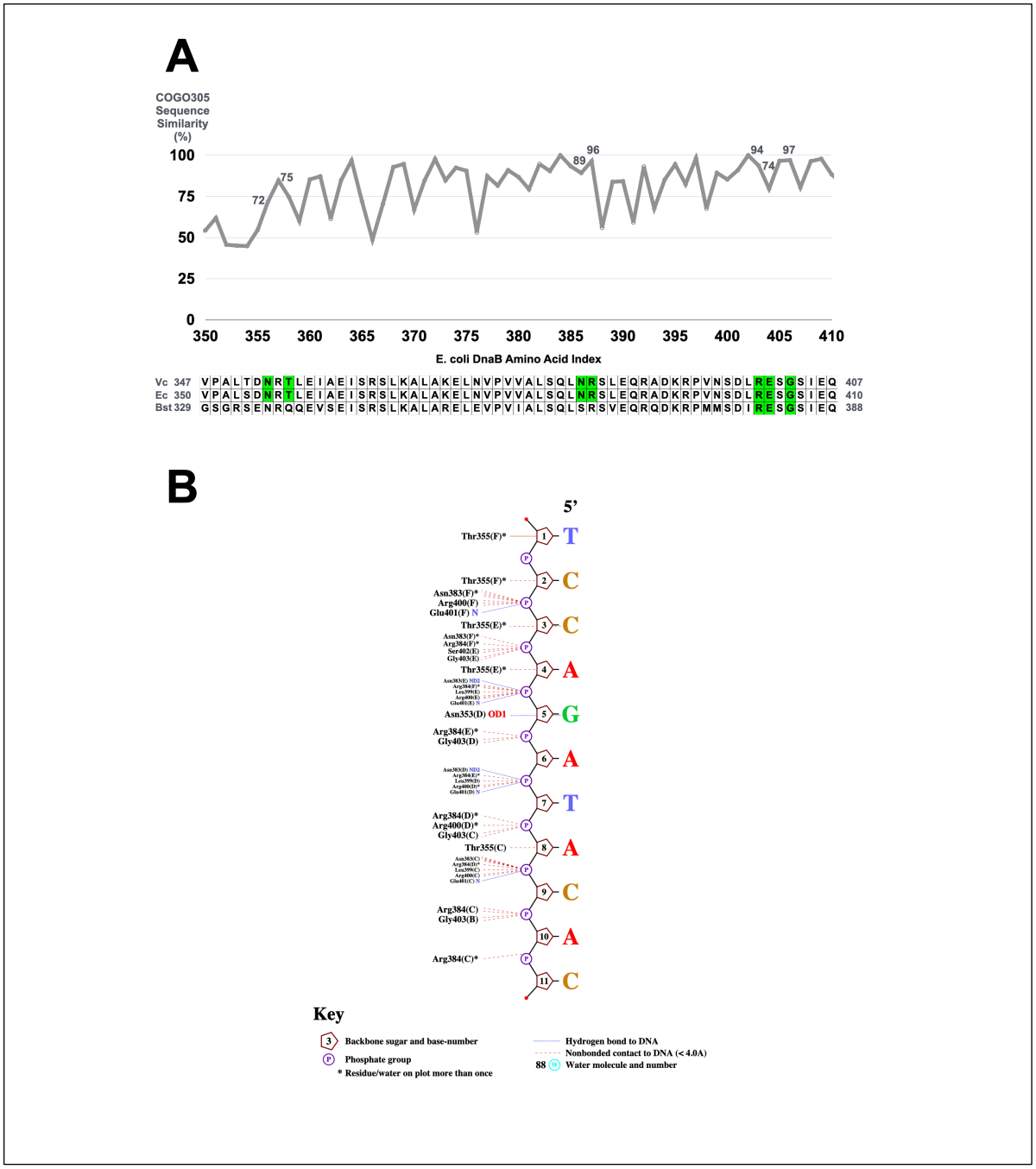

Supplementary Figure 6. Protein – ssDNA interactions in the Vc-DnaB-ssDNA complex. A) Sequence identity is plotted against the amino acid index of a portion of the sequence alignment derived from the DnaB COG0305 conserved protein domain family (100 sequences). Seven Vc-DnaB residues are in contact with ssDNA, though not every subunit uses each residue. These are N353, T355, N383, R384, R400, E401, and G403 (highlighted in green). The sequence

alignment teaches that these residues are conserved in the COG0305 DnaB-family. The conservation value for each contact residue is listed in the plot. The residues used by *E. coli* (PDB: 7T20[62]) and Bst (PDB: 4ESV[10]) are also highlighted. B) Vc-DnaB-ssDNA contacts are depicted schematically as drawn by Nucplot [117].

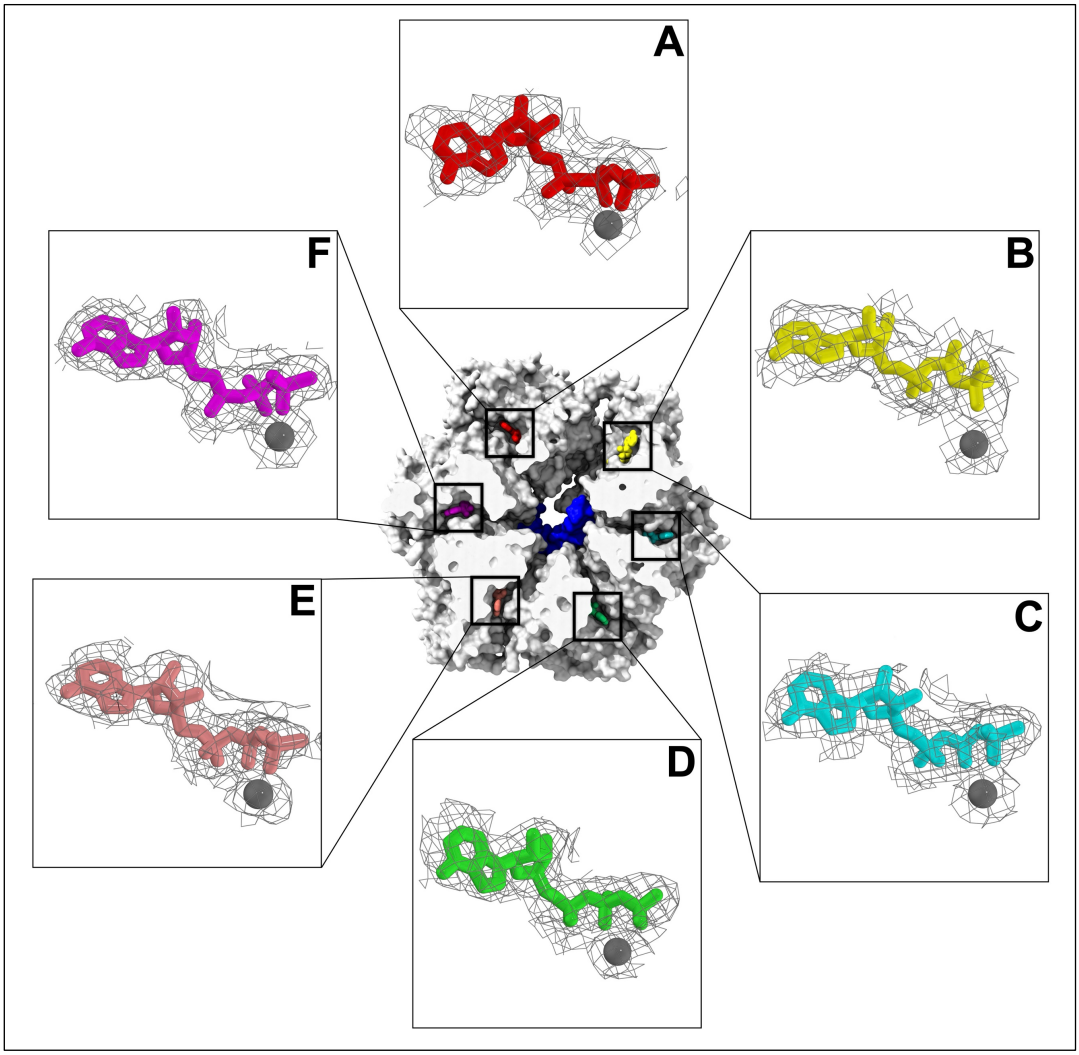

Supplementary Figure 7. The six nucleotide binding pockets in the Vc-DnaB-ssDNA structure are filled with ATPγS coordinated to a Mg^{2}+ atom. The β and γ phosphates of each ATPγS moiety are coordinated to an Mg^{2+} atom. EM density is drawn as a mesh around each nucleotide, which supports our interpretation. The density is drawn in PyMol using the following parameters: isomesh level chain B: 0.5; chains A-C-D-E-F: 2 and isomesh carve: chains A-B-C-D-E-F: 2.8. The ATPγS molecules, each colored uniquely are drawn in the stick representation, with the Mg^{2+} ion depicted as a grey sphere. The position of the nucleotide pockets is indicated on the surface representation of Vc-DnaB sliced to expose the six pockets. ssDNA within DnaB is colored dark blue.

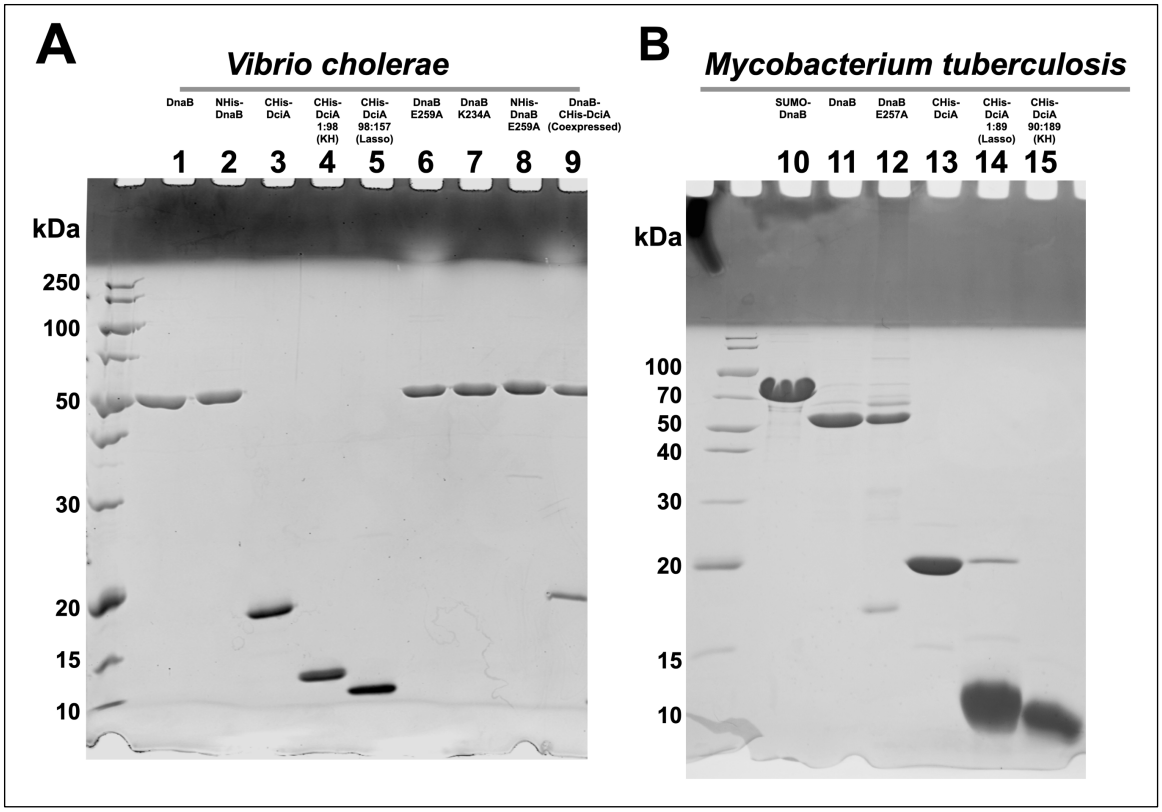

Supplementary Figure 8. Purified DnaB and DciA proteins from *Vibrio cholerae* and *Mycobacterium tuberculosis* used in this study. A) Gel electrophoretic analysis of purified Vc proteins. Lane 1: Vc-DnaB untagged; Lane 2: N-terminal His-tagged Vc-DnaB; Lane 3: C-terminal His-tagged Vc-DciA full-length; Lane 4: C-terminal His-tagged Vc-DciA KH domain (residues 1:98); Lane 5: C-terminal His-tagged Vc-DciA Lasso domain (residues 98:157); Lane 6: Untagged Vc-DnaB-E259A; Lane 7: Untagged Vc-DnaB-K234A; Lane 8: N-terminal His-tagged Vc-DnaB-E259A; Lane 9: Coexpressed Vc-DnaB untagged + C-terminal His-tagged Full-length Vc-DciA.

B) Gel electrophoretic analysis of purified Mt proteins. Lane 10: SUMO-tagged-Mt-DnaB; Lane 11; Untagged Mt-DnaB; Lane 12: Untagged-Mt-DnaB-E257A; Lane 13: Full-length C-terminal His-tagged Mt-DciA; Lane 14: C-terminal His-tagged Mt-DciA Lasso Domain (1:89); Lane 15: C-terminal His-tagged Mt-DciA KH domain (90:189).

The analyses in panels A and B are from 15% SDS-PAGE.

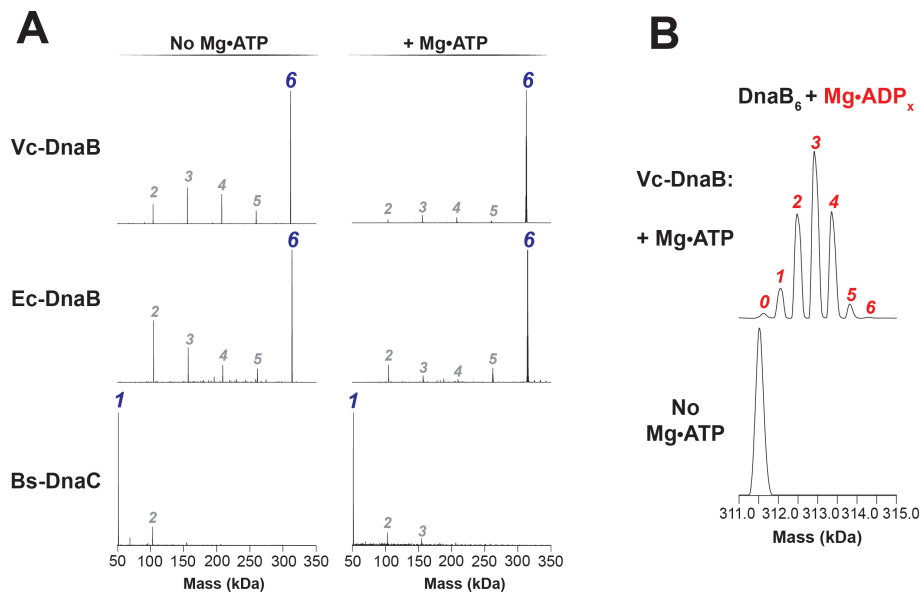

C

nMS mass measurements for Vc-DnaB in the presence of Mg•ATP

$DnaB_6$ + *x* Mg•ADP	Mass/Da Measured	Expected[a]	Δ	Mass Error (%)[b]
0	311,612	311,502	110	0.04
1	312,039	311,953	86	0.03
2	312,476	312,405	71	0.02
3	312,914	312,856	58	0.02
4	313,354	313,307	47	0.01
5	313,786	313,759	27	0.01
6	314,274	314,210	64	0.02

[a] From the protein sequence of Vc-DnaB with the N-terminal methionine removed (monomer mass = 51,917.7 Da).
[b] Calculated from the % difference between the measured and expected masses relative to the expected mass.

Supplementary Figure 9. Although highly conserved, particular DnaB helicases orthologs feature distinct oligomeric states. (A) Deconvolved nMS spectra of replicative helicases from *V. cholerae* (Vc), *E. coli* (Ec), and *B. subtilis* (Bs) with and without Mg•ATP. Unlike the *B. subtilis* ortholog, which is monomeric (with or without ATP), *V. cholerae* and *E. coli* DnaB are hexamers. Each measurement encompassed a monomeric protein concentration of 10 μM. (B) Closeup of the peaks from panel A that correspond to hexameric Vc-DnaB complex, indicating ATP hydrolysis and distinct Mg•ADP occupied states. (C) List of mass assignments of the various nucleotide-bound peaks in panel B. The expected masses for Vc-DnaB = 51.9 kDa, Ec-DnaB = 52.2 kDa, and Bs-DnaC = 51.4 kDa. The numbers in panels A and B refer to the oligomeric state of Vc-DnaB (A) and the numbers (in red) of Mg-ADP molecules bound to Vc-DnaB (B).

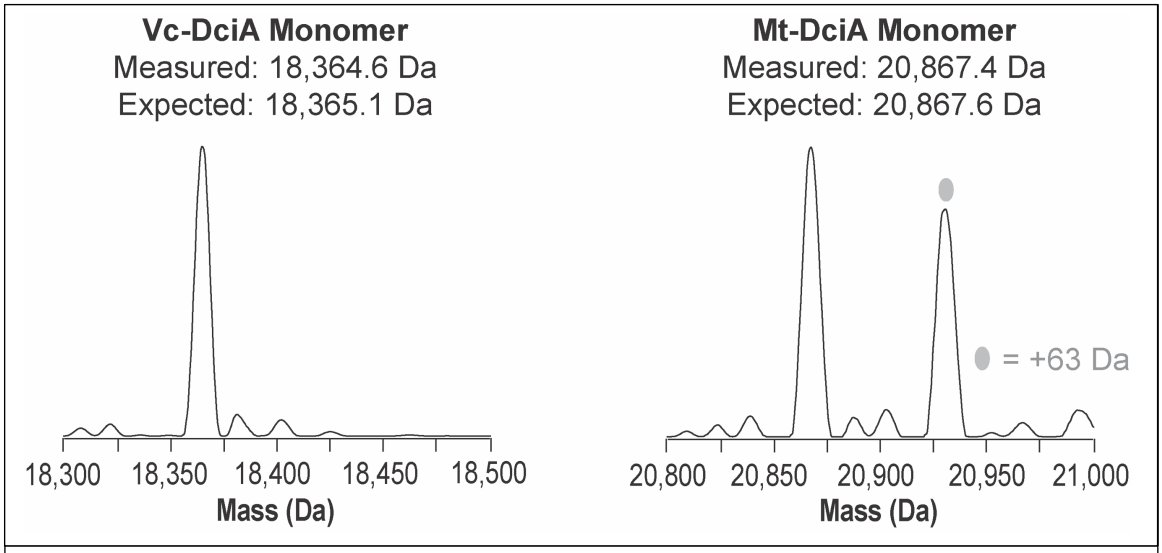

Supplementary Figure 10. Isolated Vc- and Mt-DciA are monomeric. Deconvolved nMS spectra of Vc- (A) and Mt-DciA (B). The additional +63 Da peak (grey oval) in the Mt-DciA nM spectrum most likely corresponds to a nonspecific metal ion adduct (Zn^{2+} or $Cu^{1+/2+}$) by the carboxy-terminal hexahistidine tag.

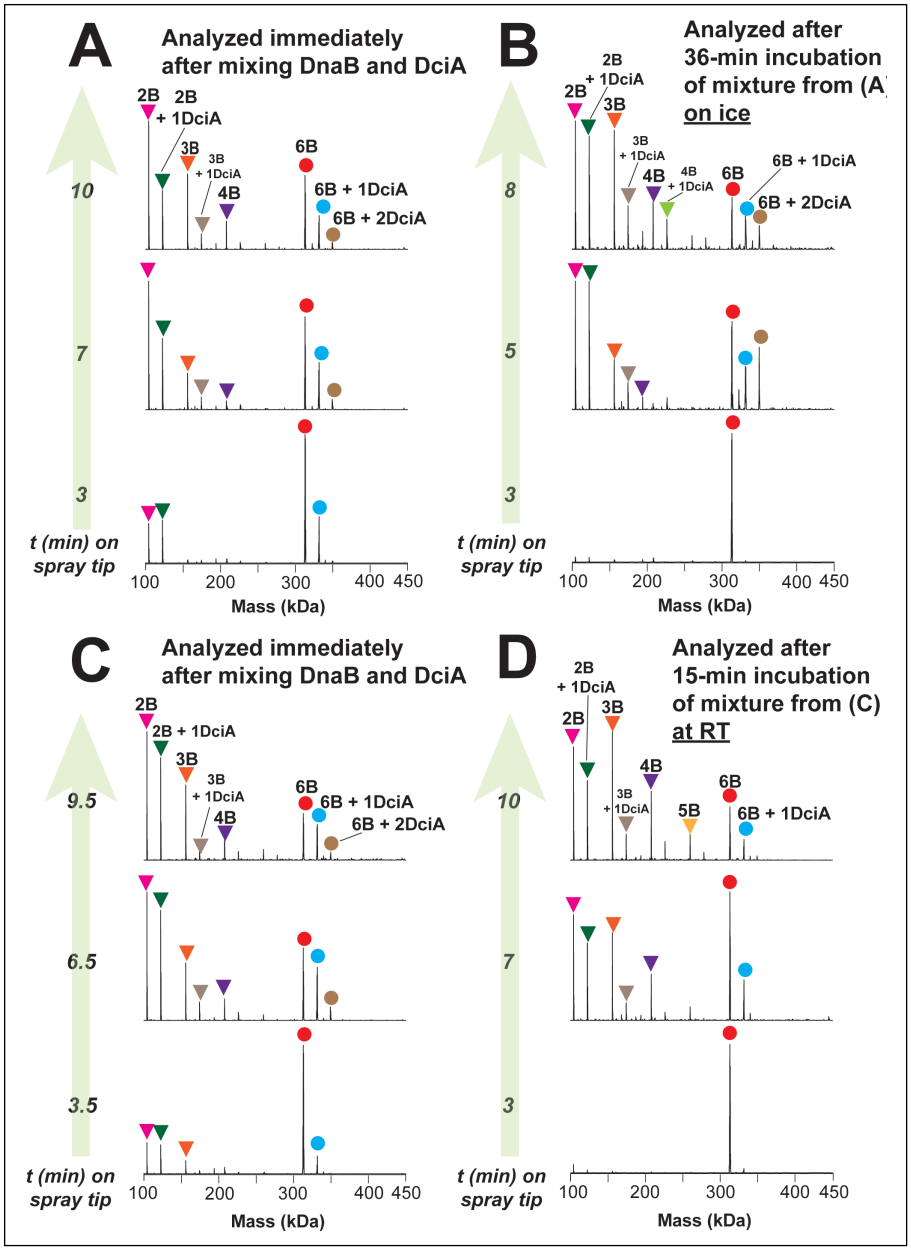

Supplementary Figure 11. Disassembly of Vc-DnaB upon incubation with Vc-DciA during nMS analysis. Vc-DnaB was mixed with Vc-DciA, and an aliquot of the mixture was loaded immediately on the electrospray tip for nMS analysis (A and C), and the rest of the mix was either incubated on ice for 36 min (B) or at room temperature for 13 min (D) before nMS characterization. The deconvolved spectra at specific time points during the nMS analysis (~100 scans averaged) and the corresponding peak assignments are shown for each sample. The overall delay time from loading the sample into the tip, setting up the electrospray, and initiating nMS data acquisition is typically 2 min. The sample mixture comprised

of 10 μM DnaB and 7 μM DciA in 10 μM ATP, 0.5 mM magnesium acetate, 500 mM ammonium acetate, 0.01% Tween-20. The peaks for $DnaB_6$ and $DnaB_6$ + $DciA_1$ predominate at the first 1 - 3 min of initiating the electrospray and then peaks with increasing intensities for $DnaB_2$, $DnaB_2$ + $DciA_1$ and other DnaB subcomplexes appear indicating progressive disassembly of $DnaB_6$. Analysis of the rest of the sample incubated on ice or at RT resulted in similar time-resolved MS profiles, suggesting that $DnaB_6$ dissociation only occurs during electrospray. Overall, the results indicate that DciA binding can destabilize $DnaB_6$, and this destabilization is intensified during the electrospray process, leading to $DnaB_6$ disassembly.

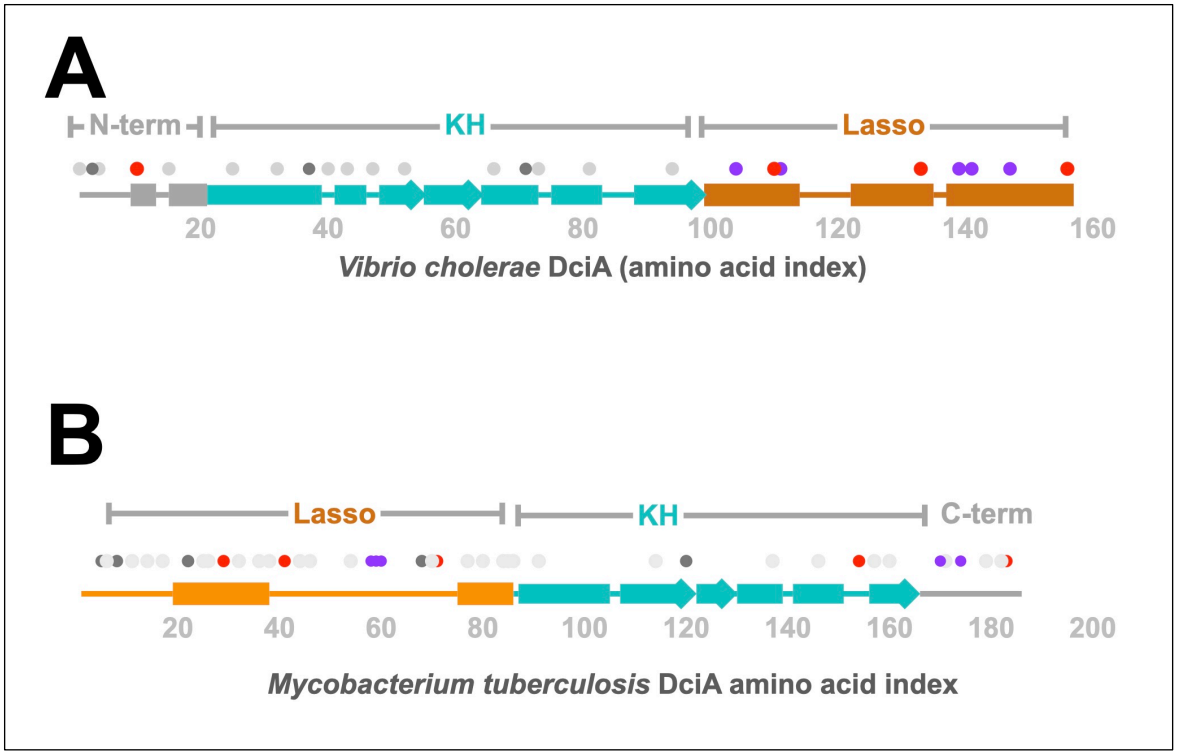

Supplementary Figure 12. The arrangement of KH and Lasso domains in the primary sequence DciA loaders from Vc and Mt is divergent. The domain architecture of DciA from Vc (A) and Mt (B) was inferred from prior analyses [40,41,58] and limited proteolysis and mass spectrometry (Supplementary Figure 10). The red and purple circles represent proteolysis sites by the Asp-N and trypsin proteases, respectively. The dark (Asp-N) and light (trypsin) grey circles represent protease sites where cuts are not observed. The KH, Lasso, and amino and carboxy-terminal domains are labeled.

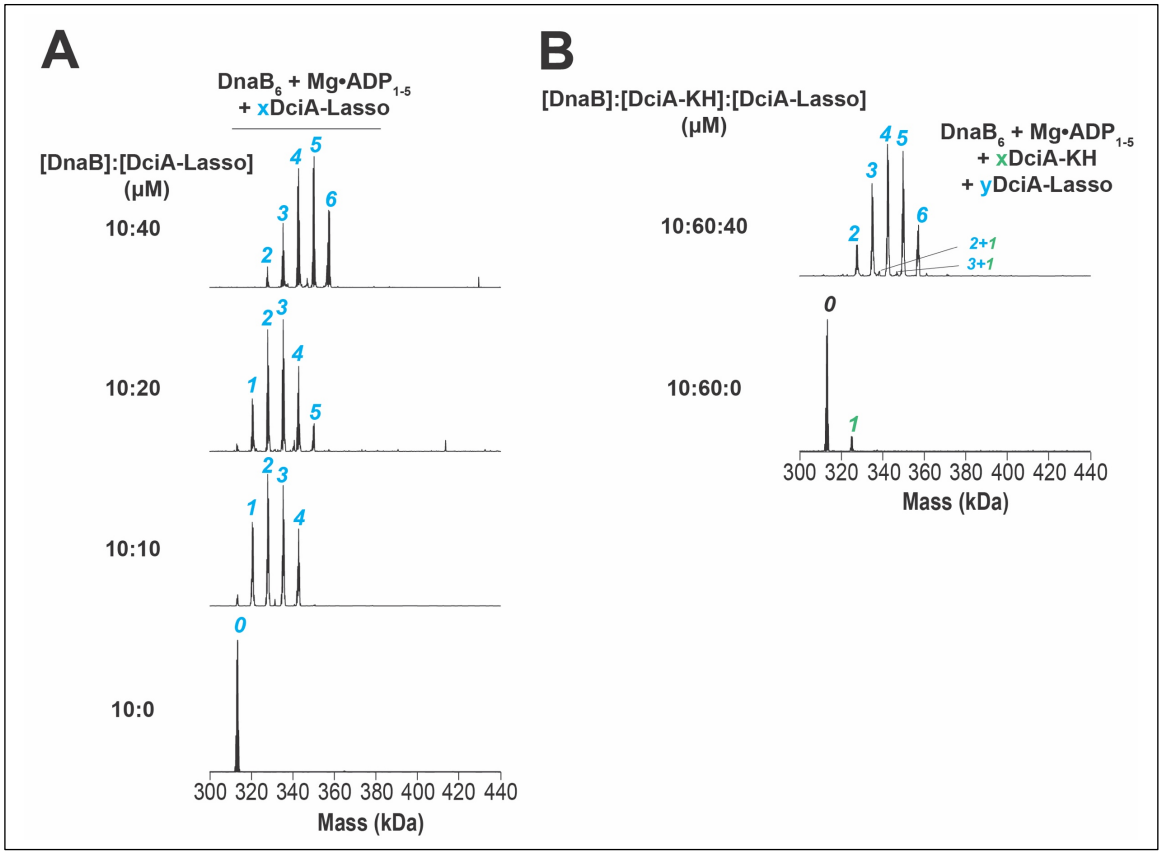

Supplementary Figure 13. Stoichiometry of binding the Vc-DciA KH domain, the Vc-DciA Lasso, and ssDNA to Vc-DnaB by nMS. Deconvolved nMS spectra of (**A**) DnaB titrated with increasing concentrations of DciA-Lasso, and (**B**) DnaB incubated with an excess DciA's KH domain in the absence or presence of DciA's Lasso domain. The expected masses of Vc-DnaB$_6$ = 311.5 kDa, DciA-KH = 11.8 kDa, DciA Lasso = 7.5 kDa, and ssDNA = 32.5 kDa. The colored numbers and Roman letters 'X' and 'Y' indicate the number of DciA-Lasso domains bound (A) or DciA-KH and Lasso bound (B).

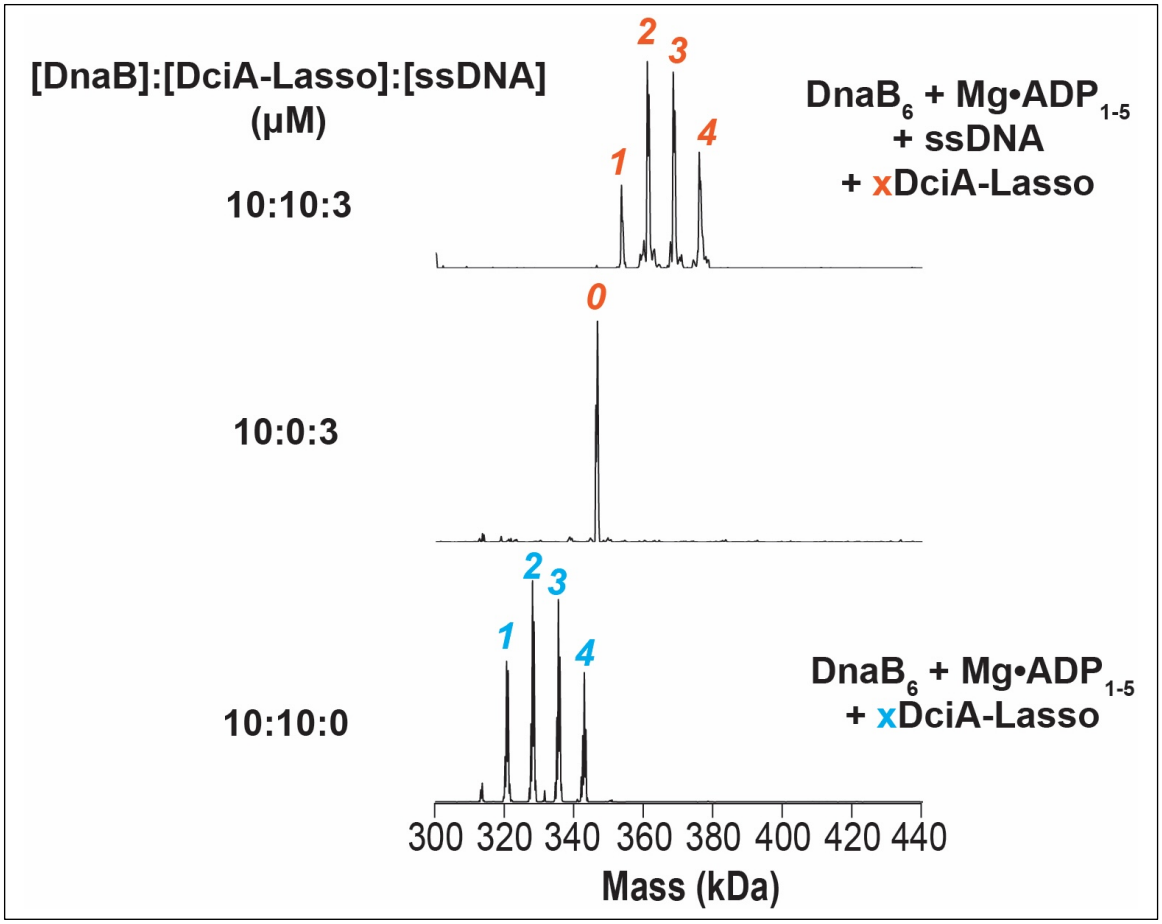

Supplementary Figure 14. The Vc- Lasso domain forms complexes with Vc-DnaB and ssDNA. Up to 4 Vc Lasso domains are found in Vc-DnaB complexes, whether ssDNA in the absence/presence of ssDNA. Deconvolved nMS spectra of DnaB and ssDNA (O4-Vc-F) incubated with and without an equimolar concentration of DciA-Lasso. All samples are in 10 μM ATP, 500 μM magnesium acetate, 500 mM ammonium acetate, and 0.01% Tween-20 before nMS analysis. Spectra were collected at the indicated DnaB: DciA-Lasso: ssDNA concentrations. The blue and red Roman letter 'X' indicates the number of copies of Vc-DciA revealed by nMS for a given sample. The expected masses are $DnaB_6$ = 311.5 kDa, DciA-KH = 11.8 kDa, DciA Lasso = 7.5 kDa, and ssDNA = 32.5 kDa.

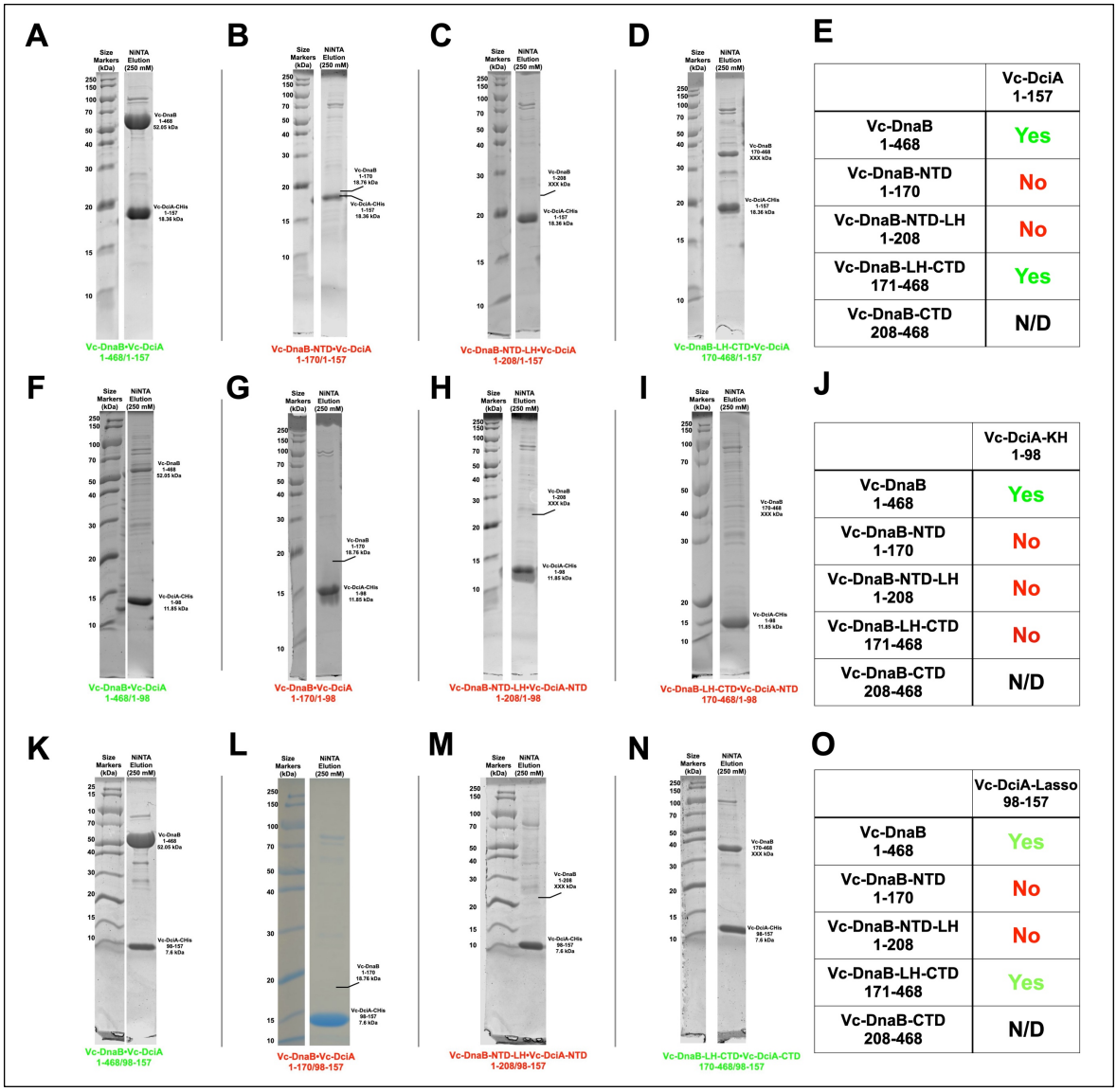

Supplementary Figure 15. Vc-DciA binds tightly to Vc-DnaB, and the Vc-Lasso domain prefers the LH-CTD domain. Composite image of 12 NiNTA 'pull down' assay between Vc-DciA (full-length: 1:157; KH: 1:98; Lasso: 98:157) and DnaB (full-length: 1:468; NTD: 1:170; NTD-LH: 1:208; LH-CTD: 171:468; CTD: 208:468) constructs. A-D) Full-length Vc-DciA and various Vc-DnaB constructs. E) Summary of binding data from panels A-D; the Vc-DnaB CTD (residues 208:468) could not be stably expressed.

F-I) Vc-DciA KH domain (1:98) and various Vc-DnaB constructs. J) Summary of binding data from panels F-I.

K-N) Vc-DciA Lasso domain (98:157) and various Vc-DnaB constructs. O) Summary of binding data from panels K-N.

The green text indicated a NiNTA pull-down scored as interacting, and the red indicated no interaction was observed.

These data show that full-length Vc-DciA binds to full-length Vc-DnaB and that the Lasso domain binds to the LH-CTD, likely at the DH-LH interface, as with other helicase loaders [12,14,19,43,44,48].

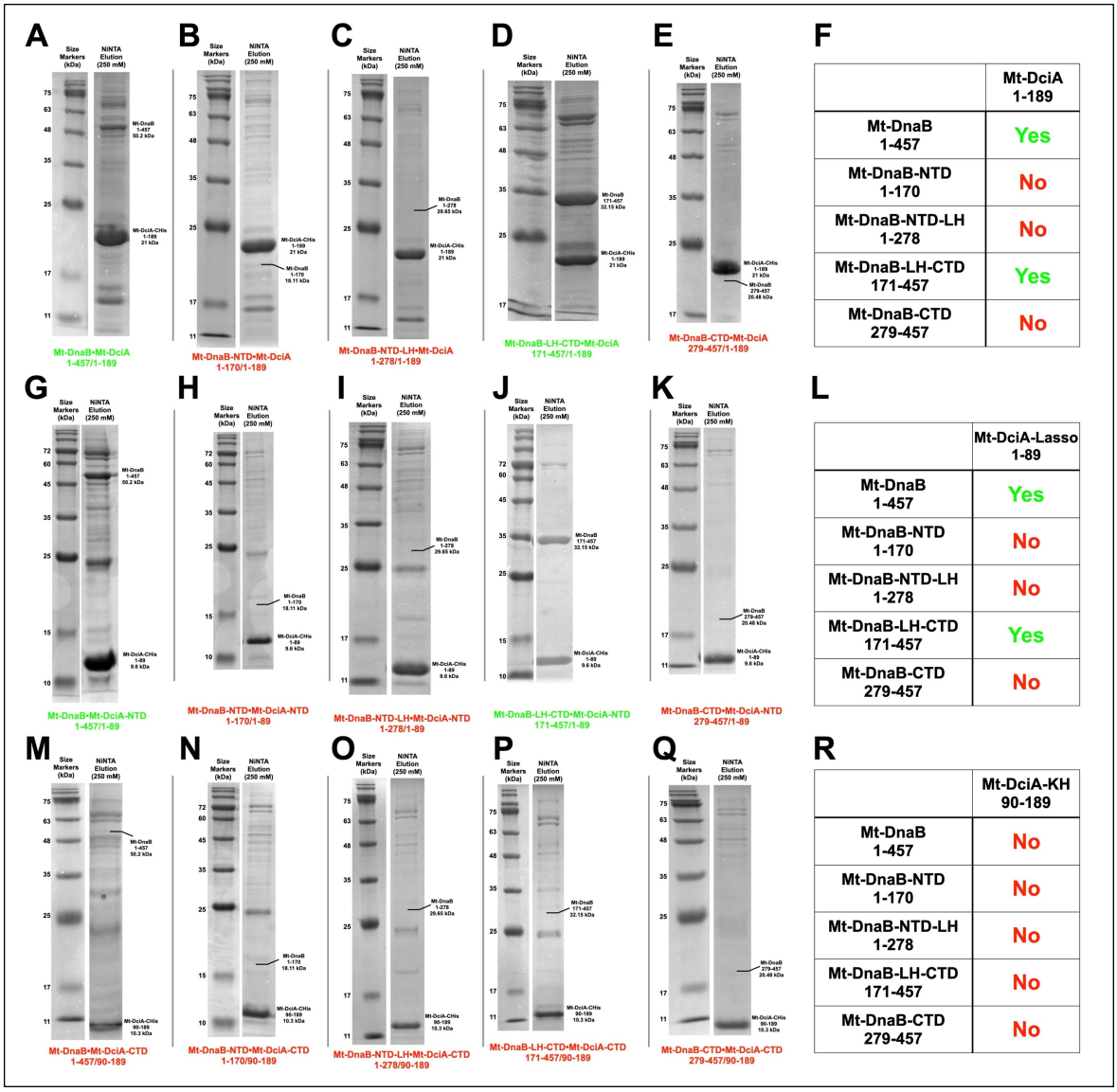

Supplementary Figure 16. The pattern of binding of Mt-DciA and its sub-domains to Mt-DnaB is identical even though the order of the domains is inverted in the primary sequence.

Composite image of 15 NiNTA 'pull down' assay between Mt-DciA (full-length: 1:189; Lasso: 1:89; KH: 90:189) and DnaB (full-length: 1:457; NTD: 1:170; NTD-LH: 1:278; LH-CTD: 171:457; CTD: 279:457) constructs. A-E) Full-length Mt-DciA and various Mt-DnaB constructs. F) Summary of binding data from panels A-E. G-K) Mt-DciA KH domain (90:189) and various Vc-DnaB constructs. L) Summary of binding data from panels G-K.

M-Q) Mt-DciA Lasso domain (1:89) and various Mt-DnaB constructs. R) Summary of binding data from panels M-Q.

The green text indicated a NiNTA pull-down scored as interacting, and the red indicated no interaction was observed.

These data show that full-length Mt-DciA binds to full-length Mt-DnaB and that the Lasso domain binds to the LH-CTD, likely at the DH-LH interface as with other helicase loaders [12,14,19,43,44,48].

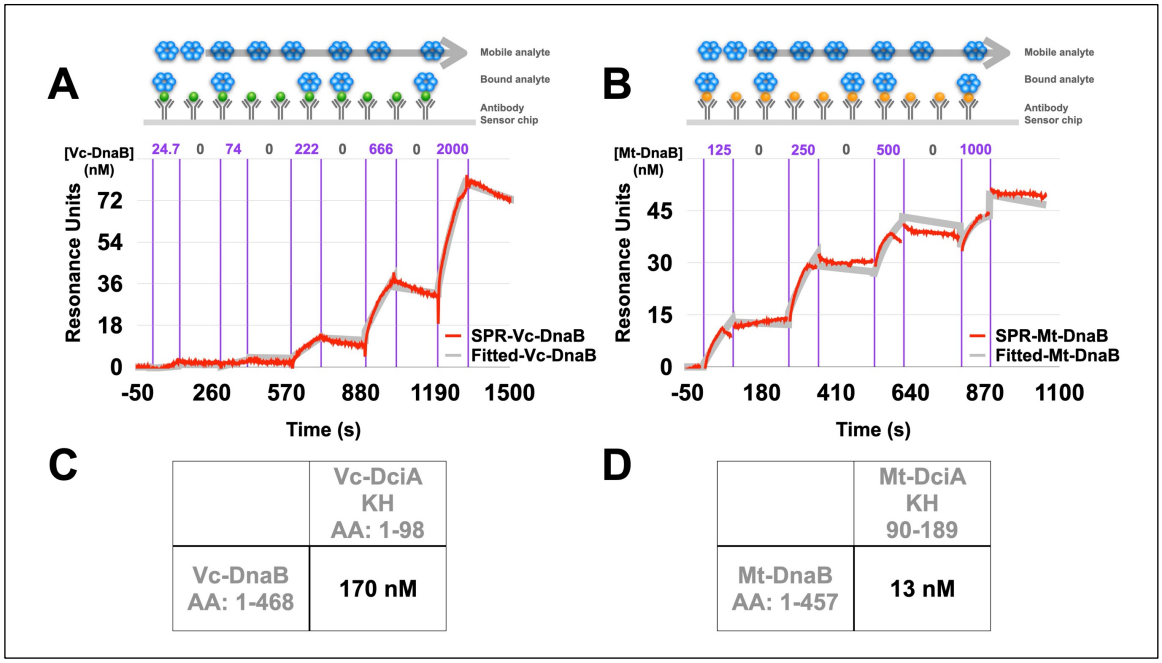

Supplementary Figure 17. Vc and Mt-DciA's KH domain retains affinity to cognate DnaB, albeit with a higher K_D. The SPR experiments are diagrammed schematically above each trace. On and off rates with full-length DnaB at incremental concentrations (Vc: 24.7, 74, 222, 666, 2000 nM; Mt: 125, 250, 500, 1000) were measured by immobilizing cognate C-terminal His-tagged DciA-KH, from Vc (A) and Mt (B) to the SPR sensor chip. The raw SPR signal is shown in red, and the fitted model is depicted in grey. Experimental data were fit as described in the methods. The single-cycle kinetic analyses through SPR revealed how DciA's KH domain retained a decreased affinity to cognate helicase. The Vc KH domain displays a K_D = 170 nM (Chi^2 = 1.82; R_{max} = 135.2), representing a ~300-fold reduction compared to full-length (A, C). This difference is less pronounced in the Mt system, where the K_D constant for binding to Mt KH is 13 nM (Chi^2 = 4.18; R_{max} = 51.23); this value is 15-fold lower than for full-length (B, D).

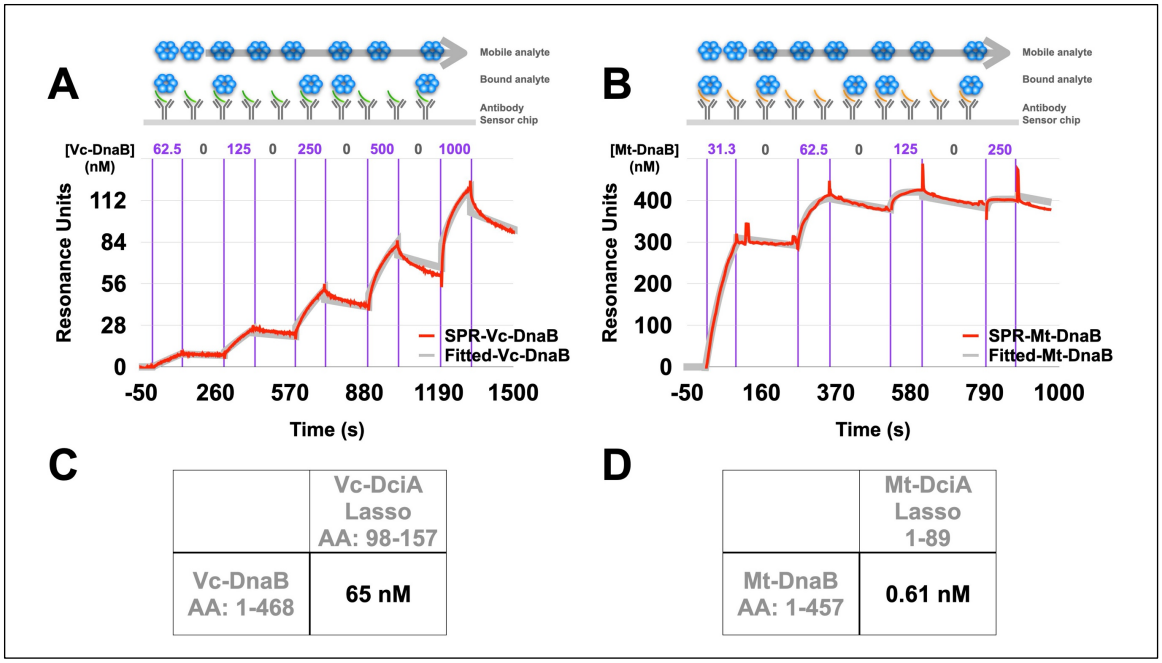

	Vc-DciA Lasso AA: 98-157
Vc-DnaB AA: 1-468	65 nM

	Mt-DciA Lasso 1-89
Mt-DnaB AA: 1-457	0.61 nM

Supplementary Figure 18. The Vc and Mt-DciA Lasso domains form energetically significant contacts to cognate DnaB. The SPR experiments are diagrammed schematically above each trace. On and off rates with full-length DnaB at incremental concentrations (Vc: 62.5, 125, 250, 500, 1000 nM; Mt: 31.3, 62.6, 125, 250 nM) were measured as described in Methods and Supplementary Figure 17. The raw SPR signal is shown in red, and the fitted model is depicted in grey. Experimental data were fit as described in the methods. The Vc Lasso domain features a K_D of 65 nM (Chi^2 = 5.89; R_{max} = 126.3), contrasting with the 0.58 nM value measured for full-length protein and the 170 nM value for the KH domain (A, C). In the Mt system, we measure a K_D = 0.61 nM (Chi^2 = 123; R_{max} = 411.5), close to the value (0.87 nM) recorded for full-length. These data establish a central role for the DciA-Lasso domain in driving the helicase-loader interaction.

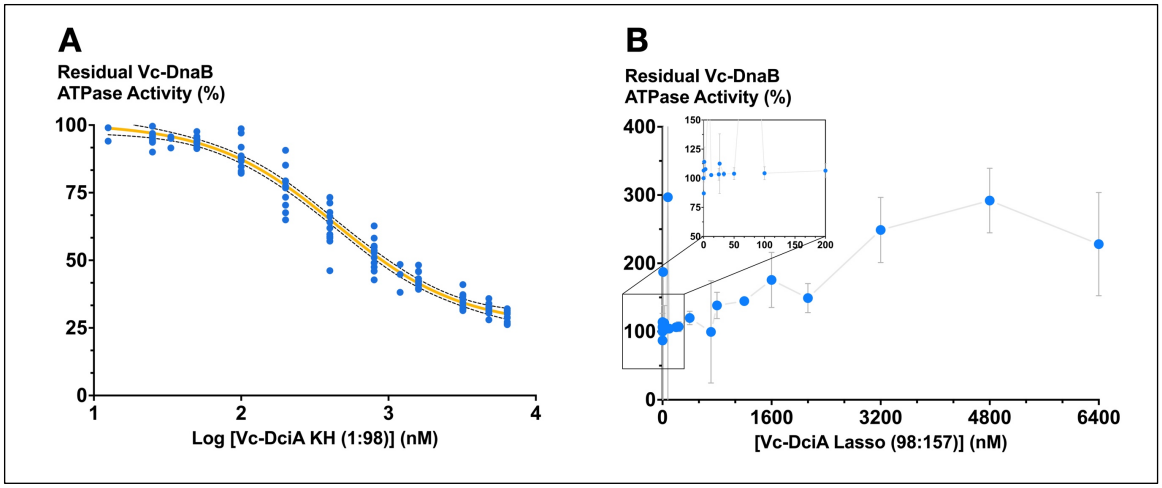

Supplementary Figure 19. The Vc-DciA KH, but not the Lasso, domain partially retains the ATPase suppression activity of full-length. A) The IC_{50} experiment and calculation described in Figure 6 were applied to the Vc KH and Lasso domains. Experimenting on four different protein batches, we find that the Vc-DciA KH domain represses Vc-DnaB ATPase activity with an IC_{50} of 442.5 nM (R^2 = 0.9693: 95% confidence interval: 380.5 to 520.0 nM), 16-fold weaker than the full-length loader. The blue dots represent individual measured ATPase rates plotted on a log scale. A non-linear fit (light-orange line), calculated using the Sigmoidal, 4PL model as implemented in PRISM, is superimposed on the experimental data. The dashed lines represent the 95% confidence interval (CI). B) The same analysis applied to the Vc-DciA Lasso domain revealed no effect on Vc-DnaB's ATPase activity at low concentrations (0.11 – 200 nM). However, the titration of a significant excess of the Lasso domain (800 – 6400 nM) revealed a 2-fold stimulation of DnaB's ATPase activity. The measured ATPase rates (blue dots) are plotted on a linear scale and connected with the grey line.

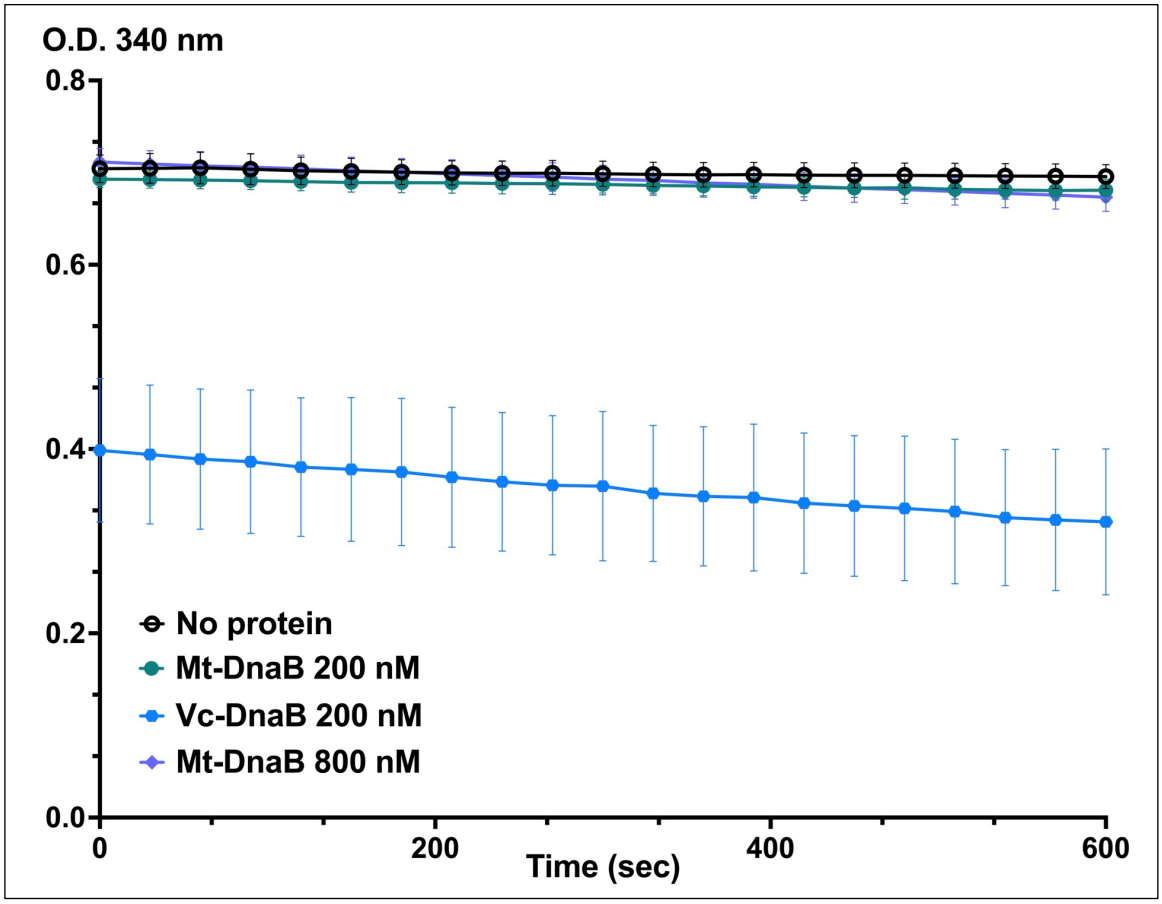

Supplementary Figure 20. Mt-DnaB is essentially inactive under the conditions tested. The basal ATPase activity of Vc and Mt DnaB were measured as described in the Methods. A comparison of the signals detected at 340 nM during the PK/LDH-coupled assay shows how Mt-DnaB is hardly more active than the measurements that lack protein. This finding is sustained at 200 nM (green) and 800 nM (violet) Mt-DnaB concentrations; both curves exhibit slopes nearly identical to the sample where the protein was omitted. By contrast, the rate produced by 200 nM Vc-DnaB (cyan) is ~10-fold higher.

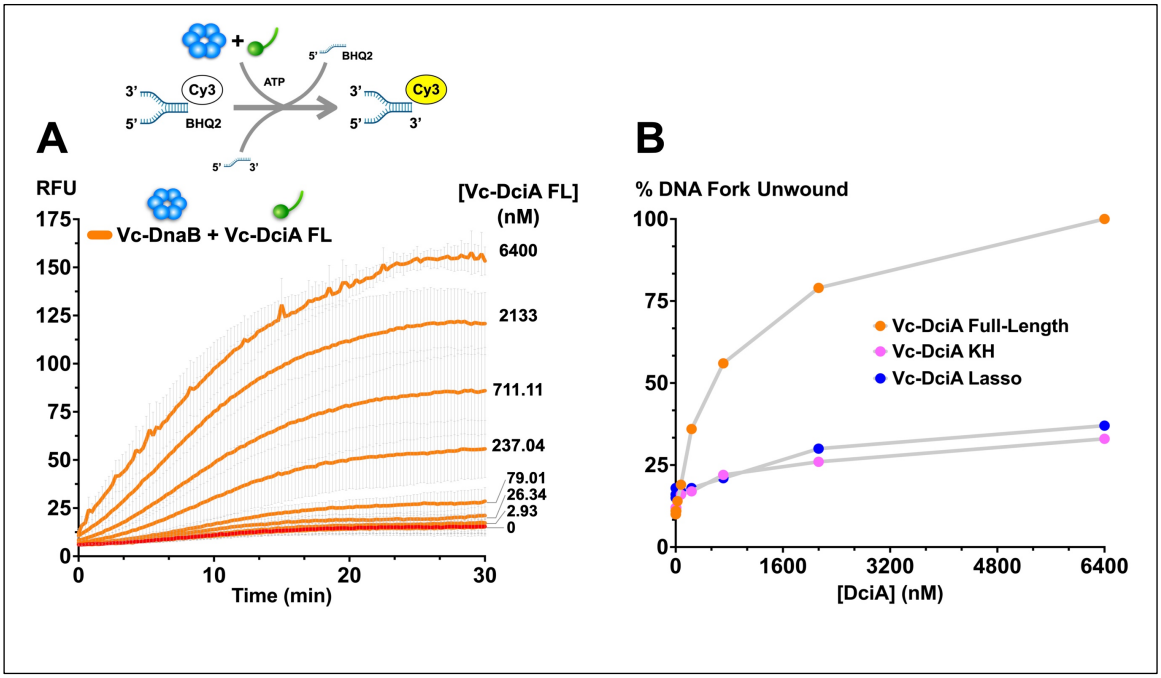

Supplementary Figure 21. Vc-DciA stimulates the DNA unwinding activity of Vc-DnaB in a concentration-dependent manner. A) The unwinding experiments employed a FRET-based 5' and 3' tailed replication fork mimic and are diagrammed schematically above. A time course of the evolution of fluorescence at 570 nm, due to relief of quenching at the Cy3/BHQ2 center during unwinding, is shown for unwinding experiments where the Vc-DnaB concentration was held fixed at 200 nM, and the Vc-DciA concentration varied from 0.11 to 6400 nM (orange curves). Shown in red is Vc-DnaB's unwinding when Vc-DciA was absent. The data imply a 10-fold stimulation of unwinding. B) The data in panel A are plotted as a function of %DNA unwound, where the highest RFU value was considered 100% unwound. By this measure, the Vc-DciA-KH (pink) and Vc-DciA-Lasso (blue) domains show 30% of the activity of full-length. Control measurements lacking Vc-DciA showed no unwinding, as was observed with the bubble substrate (Figure 7 and Supplementary Figure 25).

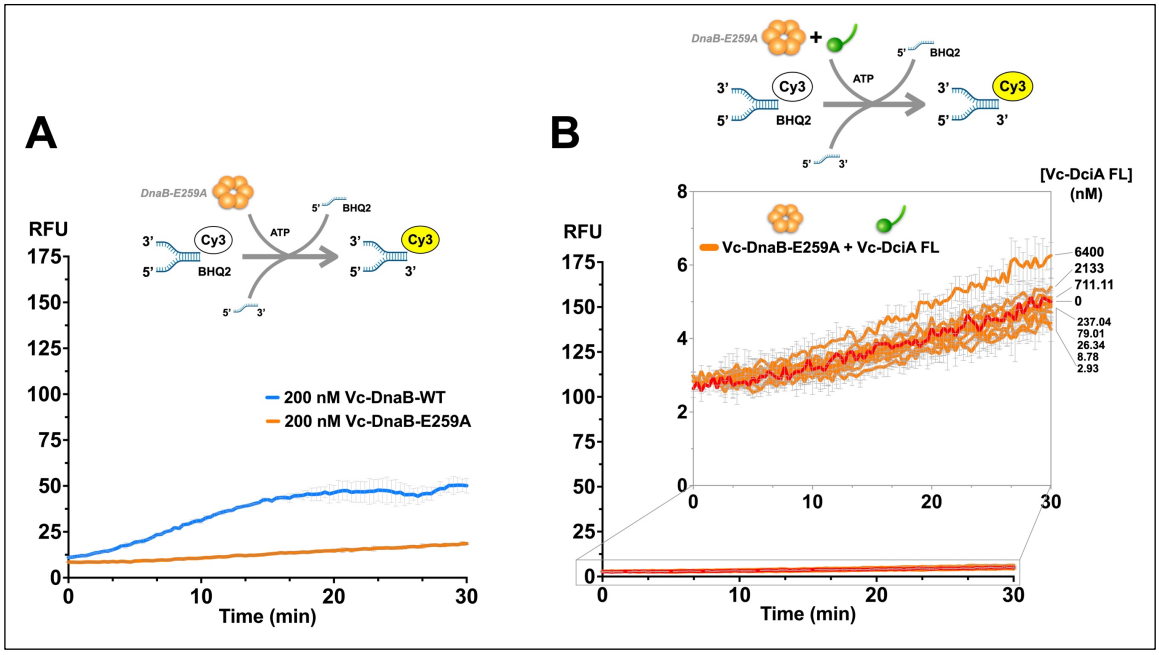

Supplementary Figure 22. The Vc Walker B glutamate (E259A) mutation abolishes DNA unwinding activity and Vc-DciA-stimulated unwinding. The FRET-based DNA unwinding experiments used a 5' and 3' tailed replication fork mimic as diagrammed schematically above each panel. A) The time course of the 570 nm fluorescence signal due to the unwinding of the DNA substrate is plotted for wild-type (blue) and E259A mutant (orange) DnaB. In this experiment, the Vc-DnaB concentration was held at 200 nM. The Walker B mutation significantly reduces unwinding activity. B) The time course of the 570 nm fluorescence signal arising from titration of Vc-DciA (0.11-6400 nM) into an assay containing the Walker B Vc-DnaB-E259A mutant. Essentially no unwinding activity was recovered. The inset shows the same data but expands a section of the plot.

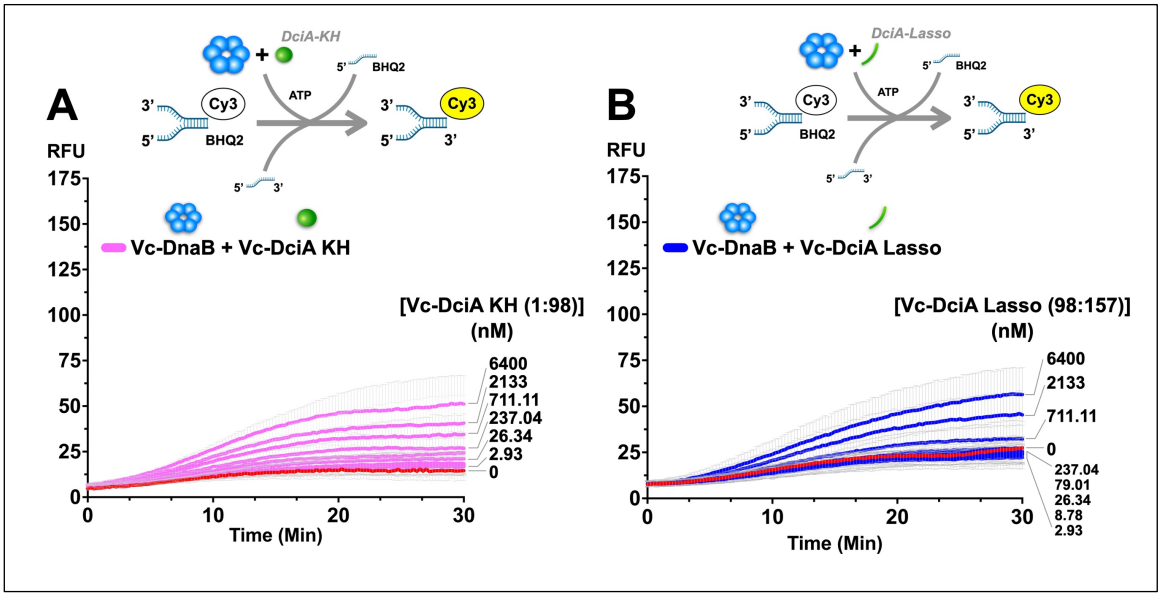

Supplementary Figure 23. The isolated KH and Lasso domains of Vc-DciA exhibit significantly reduced activity. The FRET-based DNA unwinding experiments used a 5' and 3' tailed replication fork mimic as diagrammed schematically above each panel. Titration of Vc-DciA-KH (pink, A) or DciA-Lasso (blue) domains into the assay stimulated DnaB's unwinding activity by only 30% with respect to full-length DciA. The titration of appropriate DciA-construct encompassed concentrations from 0.11 to 6400 nM. At most, the isolated KH and Lasso domains stimulated DNA unwinding by 3.3-fold compared to a sample lacking DciA. By contrast, full-length DciA produces a 10-fold increase (Supplementary Figure 21).

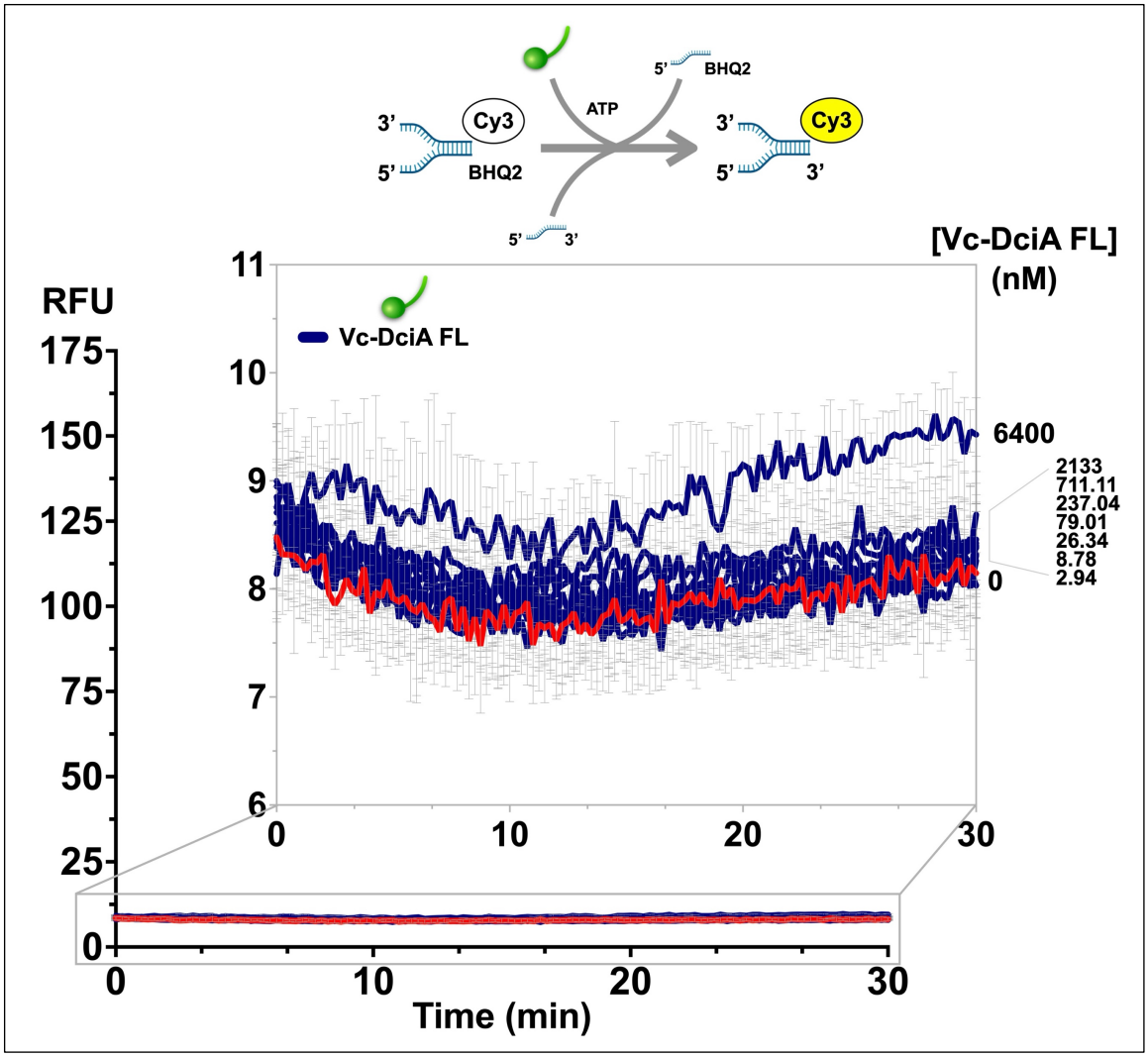

Supplementary Figure 24. Isolated Vc-DciA fails to unwind the 5' and 3' tailed replication fork-mimic. Titration from 0-6400 nM (blue curves) of Vc-DciA into an assay that lacks DnaB, as diagrammed schematically above, fails to show any 570 nm fluorescent signal arising from unwinding of the DNA. The inset shows a plot section expanded around RFU values of 6-11. The red curve describes fluorescent signals from an experiment that lacked DciA. These data suggest that DciA alone fails to unwind the fork DNA substrate; this finding contrasts with robust unwinding seen with the DNA bubble substrate; the reason for this difference in activity is unknown.

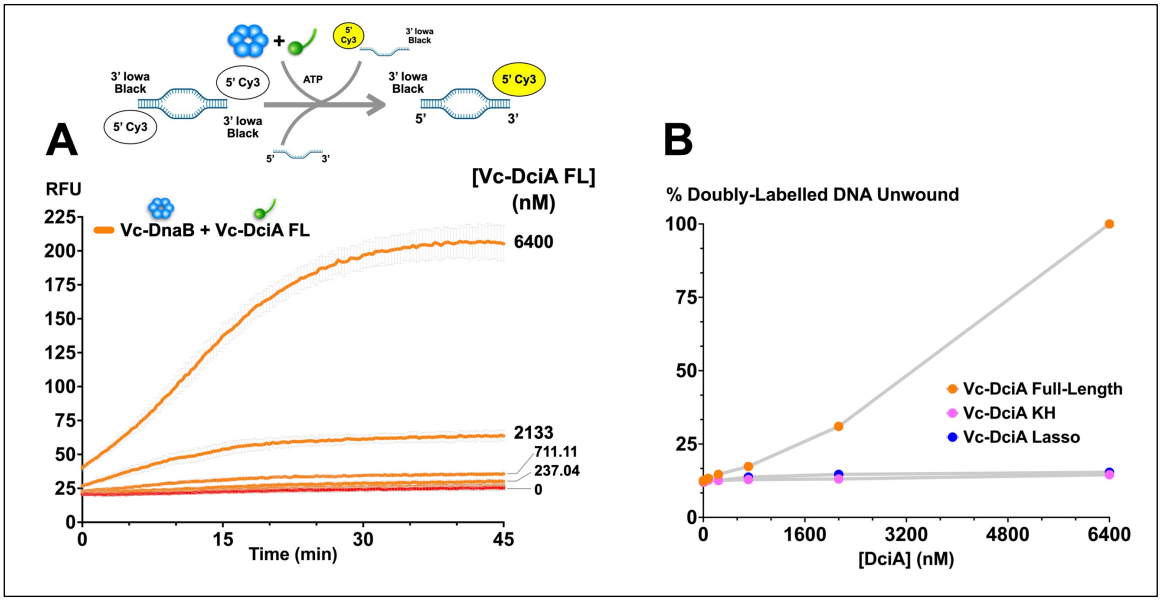

Supplementary Figure 25. Measurement of Vc-DciA-mediated loading of Vc-DnaB using a doubly labeled DNA bubble. The assay diagrammed above was performed precisely as the singly labeled DNA bubble substrate in Figure 7, except that FRET labels were included at both ends of the DNA bubble. A) A time course (orange curves) of fluorescence at 570 nM was recorded from an experiment wherein Vc-DciA was titrated from 0.11 to 6400 nM while the Vc-DnaB concentration was fixed at 200 nM. The red curve shows the signal from an experiment that lacked Vc-DciA. Surprisingly, the amplitude of the fluorescence signals did not increase two-fold compared to the singly labeled, as was expected, given the presence of two fluorescence centers; instead, the signal increased by 10%. B) Data from panel A plotted a % DNA unwound as a function of Vc-DciA concentration. These data show no loading activity by the Vc-DciA-KH (pink) or Lasso domains (blue), even with a significant excess of each domain (Supplementary Figure 27).

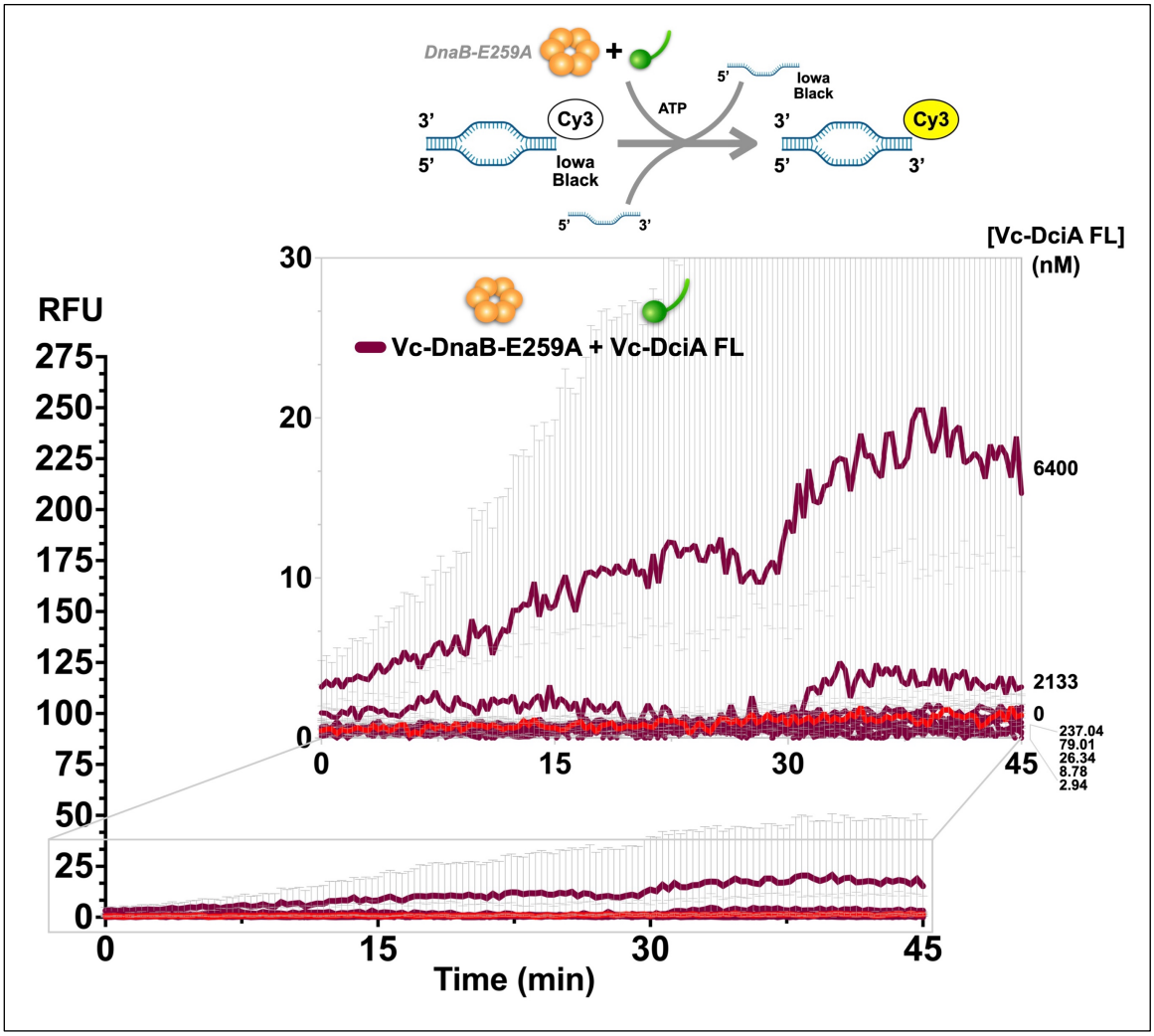

Supplementary Figure 26. The Vc Walker B glutamate (E259A) mutation is deficient in Vc-DnaB loading on a physiological bubble substrate. This experiment, diagrammed above the plot, is similar to that shown in Supplementary Figure 22, except that a DNA bubble substrate is used. The plot depicts a point-by-point subtraction of the fluorescence signals generated by Vc-DciA (taken from Figure 7B). The resulting curves (orange) show little loading activity above the basal rate measured without DciA (red). Only when DciA is present at 6400 nM is a curve with significant activity above the basal rate observed. However, the amplitude of this curve (~15) was 30% of the amplitude seen with wild-type Vc-DnaB. The inset shows the same data but expands a section of the plot.

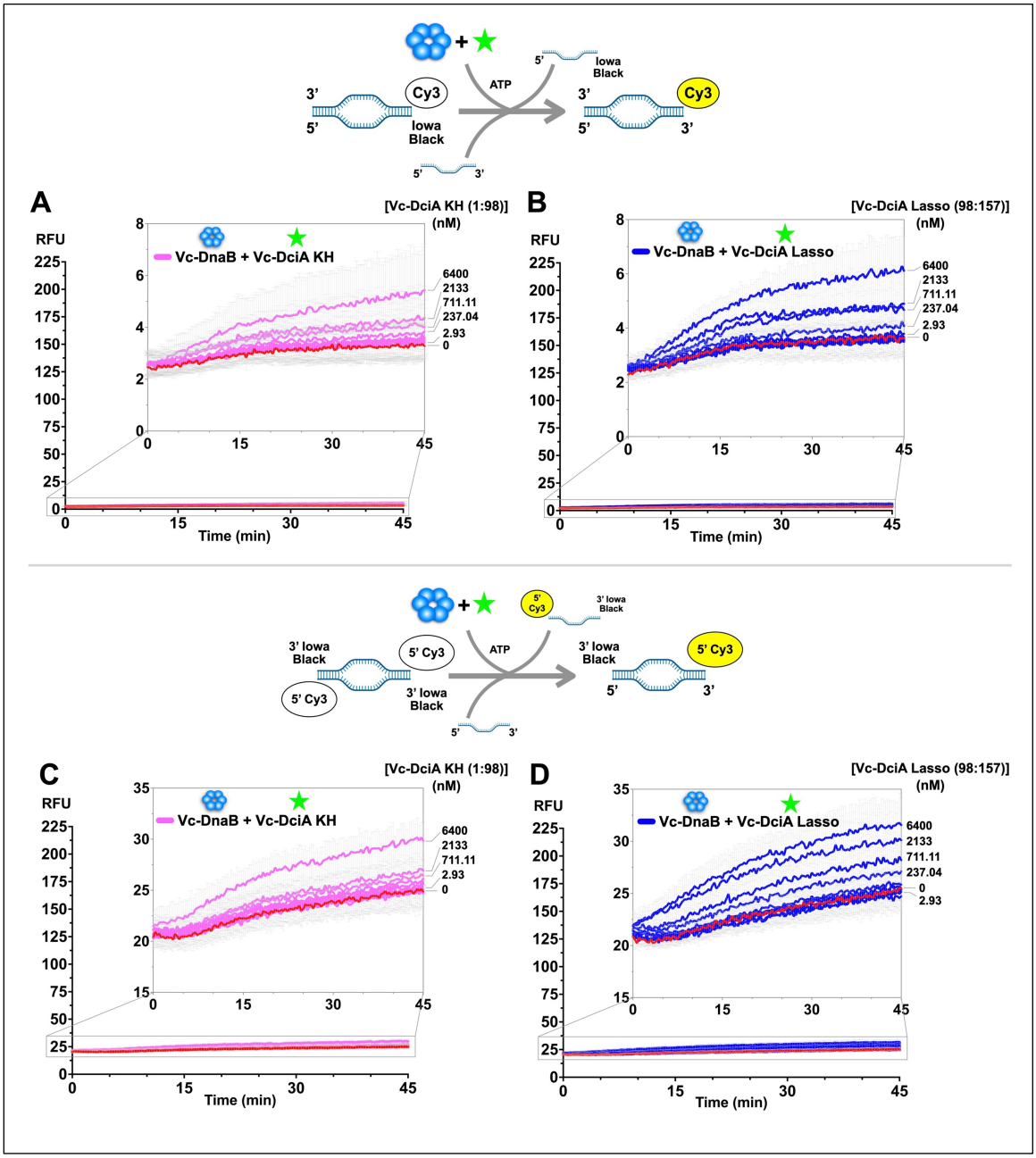

Supplementary Figure 27. The isolated Vc-DciA KH and Lasso domains are inactive in the bubble-loading assay. These measurements diagrammed above each panel, represent controls for parallel studies with full-length Vc-DciA. Panels A and B employ the singly labeled substrate, and panels C and D employ the doubly labeled substrate. Titration of the appropriate DciA construct was carried out as described in Figure 7. Measurements with the Vc-DciA-KH domain are colored pink, and those with the Vc-DciA-Lasso domain are colored blue. The red curves in each plot represent the basal rate of loading measured in the absence

of Vc-DciA. With the singly labeled substrate, a 1.5 to 2-fold increase in the fluorescence signal was seen at the highest concentration tested (6400 nM); in contrast, full-length Vc-DciA produces a 10-fold increase (Figure 7). With the doubly labeled substrate, a ~1.2-fold increase in the fluorescence signal was seen at the highest concentration tested (6400 nM); in contrast, full-length Vc-DciA produces an 8-fold increase (Supplementary Figure 25). The lack of differentiation of the DciA titration-derived curves from the basal rate (red) leads us to conclude that each Vc-DciA truncated construct is inactive in helicase loading.

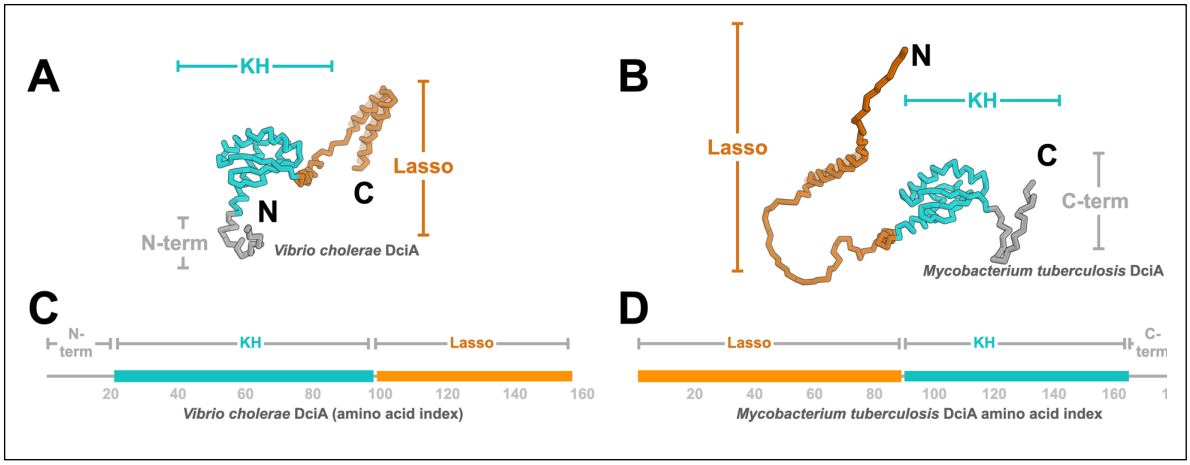

Supplementary Figure 28. Calculated structures of DciA loaders from *Vibrio Cholerae* and *Mycobacterium tuberculosis*. Ribbon representation of the Alphafold calculated structures of DciA from Vc[123] (A) and Mt[124] (B). Linear representation of Vc-DciA and Mt-DciA in panels C and D. The KH domain is colored cyan, the Lasso orange, and other segments in grey. Vc-DciA is also seen in the crystal structure of the Vc-DnaB-Vc-DciA complex (PDB: 8A3V)[14].

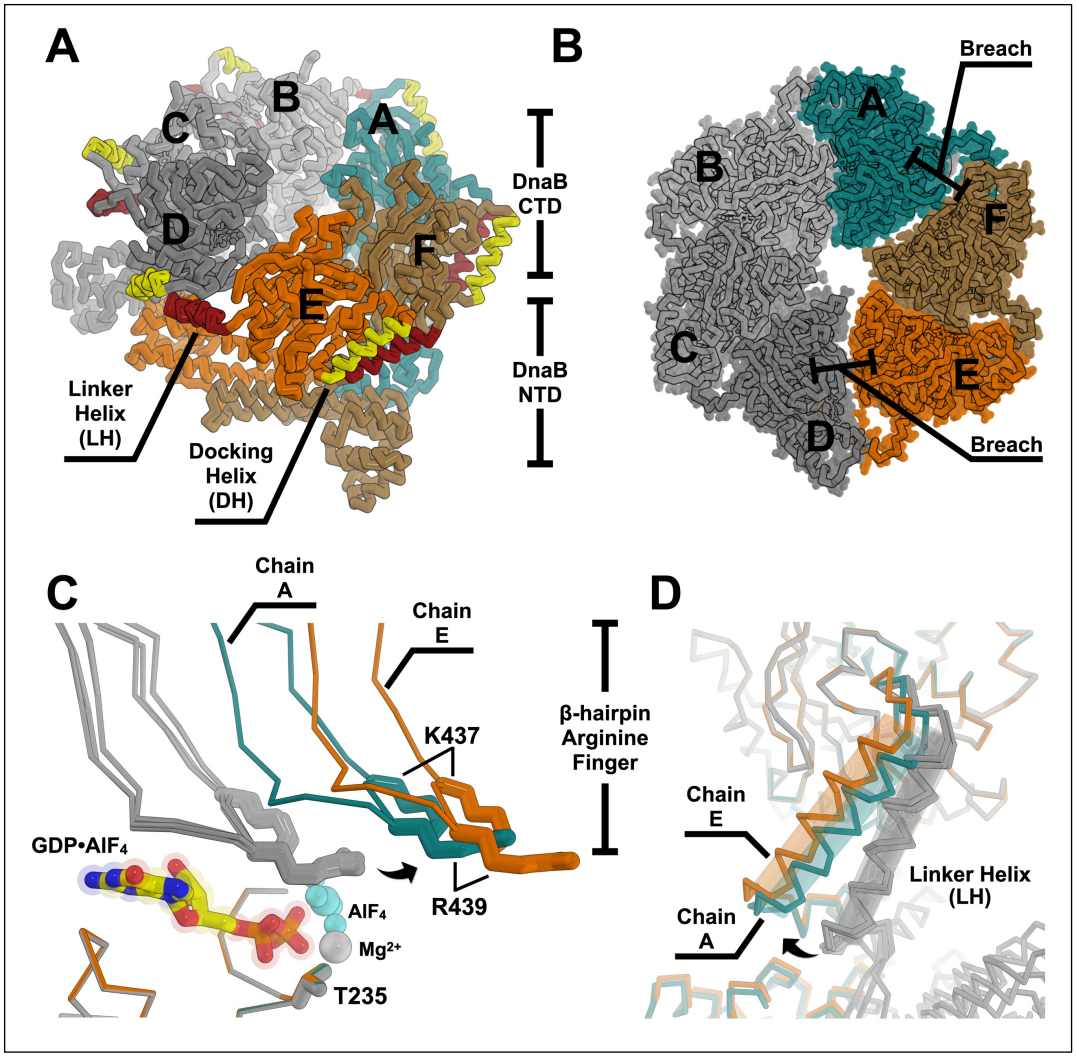

Supplementary Figure 29. Crystal Structure of Vc-DnaB-GDP/AlF$_4$ (PDB: 6T66) and the disposition of β-hairpin arginine fingers and Linker Helix elements. A) Vc-DnaB is depicted as a ribbon with chains labeled. The NTD and CTD layers are indicated. The six Docking-Helix (DH) and Linker-Helix (LH) elements are shown in yellow and red, respectively. Chains A, F, and E are shown in blue, sand, and orange, and the other chains are in alternating shades of gray. B) The 6T66 DnaB structure depicts the two breaches in the CTD layer: the largest is between chains E (orange) and D (grey), and the narrowest is between chains A (deep teal) and F (sand). The protein surface is drawn with the PyMol solvent radius = 0.3 setting. C) The six CTD pairs (A-B, B-C, etc, residue 200:461) from 6T66 were superimposed (RMSD = 0.03 Å) on chain A, but where the DH elements (residue 280:306) and the second chain were excluded from the calculation. Each

Vc-DnaB harbors a GDP•AlF_4 species, and only one is shown in the stick representation, which has transparent spheres overlaid. The β-hairpin arginine fingers are shown as ribbons, and K437 and K439 are shown as sticks. The β-hairpins from four chains (B, C, D, F) follow each other closely (grey), although not included in the alignment. The corresponding elements from chain A (deep teal) and E (orange) have moved away by ~9 Å and ~13 Å, respectively.

D) The superposition from panel C was interrogated for the disposition of the LH elements represented as transparent cylinders. The LH elements from chains B, C, D, and F (grey) superimpose closely and occupy the LH1 position as defined in the main text and Supplementary Figure 4. In contrast, those belonging to chain A (deep teal) and chain E (orange) drift away by ~5-~9 Å and occupy position LH2.

Supplementary Movie 1. Migration of Subunits from the Bottom to the Top of the DnaB spiral during translocation. This video shows the transition from the ATPγS conformation of the present Vc-DnaB-ssDNA complex to the GDP-AlF_4 configuration of the Bst 4ESV DnaB ssDNA [10] complex. The two complexes are aligned by superimposing the ssDNA molecules of each structure, as detailed in the main text. The motions depicted in the video are described in the main text. The DnaB-ssDNA-ATPγS complex is drawn in the ribbon representation (left) or the sphere/cylinder/ribbon schematic (right). Both representations are colored by chain. The ssDNA is shown in cartoon and stick representation and is colored orange. To calculate the transition between structures, a version of the 4ESV coordinates was constructed that encompassed the *Vibrio cholerae* primary sequence. The two states were then submitted to PyMol to calculate the 90 intermediate structures between the ATPγS and the GDP-AlF_4 conformers and an additional 90 structures between the GDP-AlF_4 and ATPγS structures. Frames were rendered in PyMol and assembled in QuickTime player.

Supplementary Methods

Expression Plasmid Construction

Genes corresponding to full-length *Vibrio cholerae* (Vc) DnaB and Vc-DciA were amplified using polymerase chain reaction (PCR) and genomic DNA from *Vibrio cholerae* N16961 (ATCC # 39315D-5), and, variously, cloned into the following protein expression vectors (pET24a, pCDFDuet-1, or pRSFDuet-1). These efforts encompassed untagged, amino, or carboxy-terminal hexahistidine-tagged proteins. Point mutations were introduced using the Quickchange Site Directed Mutagenesis kit (Agilent).

Genes encoding full-length wild-type and Walker B point mutant (E257A) *Mycobacterium tuberculosis* Mt-DnaB (NCBI accession number CCP42780.1) were synthesized and cloned into the pET28a vector (Genscript) to generate an amino-terminal hexahistidine-SUMO-tagged Mt-DnaB (Mt-DnaB-SUMO_pET28a) or cloned into the pET16b vector (Genscript) to express untagged *Mt-DnaB*. *Mt*DnaB gene (1:874) contains an intein (400:815) [61,80,81], which was not included in the expression plasmid. To keep the Mt-DnaB numbering consistent with other orthologs that lack inteins, we numbered the sequence from 1-457, where the intein was excluded. Four truncated variants of Mt-DnaB (NTD: residues 1:170; CTD: residues 279-457; NTD-LH Residues 1:278; LH-CTD Residues 171:457) were subcloned into a pCDFDuet-1 plasmid (Genscript) for protein expression.

Genes encoding full-length *Mt-DciA* (NCBI accession number NP_214518.1) (Mt-DciA_pET22b), *Mt-DciA*-NTD (residues 1-89, Mt-DciA-NTD_pET22b), or *Mt-DciA*-CTD (residues 90-189, Mt-DciA-CTD_pET22b), as

fusion proteins with a C-terminal 6xHis were cloned into pET22b vector for protein expression.

E. coli DnaB was prepared as previously described of the *E. coli* DnaB•λP complex, except that λP was omitted [44].

Protein Expression

For production-scale bacterial growths, colonies corresponding to bacterial transformants were picked and resuspended in LB media supplemented with the appropriate antibiotic concentration. Bacterial cultures were grown at 37 °C to an OD600 ≈ 0.6 – 0.7 (RPM = 180). Protein expression was induced by making the culture 0.5 mM in isopropyl -D-1-thiogalactopyranoside (IPTG), followed by a temperature shift of the culture to 16 °C; protein production was allowed to continue for 14-16 hours (RPM = 180). Cells were recovered by centrifugation, resuspended in 20mM Tris-HCl pH 7.4, 500mM NaCl, 5mM $MgCl_2$, 10% sucrose, 5mM β-mercaptoethanol at a ratio of 5 mL buffer per gram of wet cells, and frozen at -80°C.

Vc-DnaB. Vc-DnaB-untagged (pNG066, 50 µg/mL kanamycin), Vc-DnaB-NHis (pNG067, 50 µg/mL kanamycin), Vc-DnaB-E259A-NHis (pNG072, 50 µg/mL kanamycin), Vc-DnaB-NTD-untagged (pNG114, 50 µg/ml kanamycin), Vc-DnaB-NTD_LH-untagged (pNG131, 50 µg/mL kanamycin) and Vc-DnaB-LH_CTD-untagged (pNG134, 50 µg/mL kanamycin) were expressed using the above procedure.

Vc-DciA. Vc-DciA-FL-CHis (pNG057, 50 µg/ml streptomycin) and Vc-DciA-CTD-CHis (pNG087, 50 µg/ml streptomycin) were expressed using the procedure above, except for three changes: a) the media was LB for pNG057 and SB [125,126]:

for pNG087, b). after adding 0.5 mM IPTG to the culture, protein expression was allowed to continue for 3 hours at 37 °C, and c) cells were resuspended after harvesting in 20 mM Tris-HCl pH 8, 300 mM NaCl, 5% glycerol, 5 mM β-mercapoethanol.

Vc-DciA-NTD-Chis (pNG078, 50 µg/ml streptomycin) was grown using the same procedure as full-length DciA, except that cells were resuspended in 20 mM Tris-HCl pH 8, 300 mM NaCl, 5% glycerol, and 5 mM β-mercapoethanol.

Vc-DnaB-Vc-DciA coexpression. Vc-DnaB-untagged (pNG066, streptomycin: 50 ug/mL) and Vc-DciA-FL-Chis (pNG057, Kanamycin: 50 ug/mL) were co-expressed using the above procedure altered to account for the co-expression.

Mt-DnaB. Cells bearing plasmids encoding NHis-SUMO-Mt-DnaB (Mt-DnaB-SUMO_pET28a) were grown in 2xTY medium [127], supplemented with kanamycin (50 µg/mL). The culture was permitted to grow at 37 °C to an OD600 ≈ 0.6, after which IPTG was added to 0.1 mM. Protein expression was allowed to continue for 20 hours at 17 °C (RPM = 210), after which the cells were harvested by centrifugation at 4 °C and frozen at -80 °C.

Mt-DnaB-untagged (Mt-DnaB-WT_pET16b) was expressed using the same procedure as adopted for the other Mt-DnaB constructs, except that the culture included 50 µg/mL ampicillin, was induced with 0.15 mM IPTG, and protein expression continued for 18 hours.

Untagged truncations here, Mt-DnaB-NTD (Mt-DnaB-NTD_pCDF-DUET-1), Mt-DnaB-NTD-LH (Mt-DnaB-NTD-LH_pCDF-DUET-1), Mt-DnaB-LH-CTD (Mt-DnaB-LH-CTD_pCDF-DUET-1) and Mt-DnaB-CTD (Mt-DnaB-CTD_pCDF-DUET-

1) were expressed using the same procedure as for Mt-DnaB-untagged, except for the inclusion of Streptomycin (50 µg/mL) during culturing and addition of 0.5 mM IPTG for protein expression.

Mt-DciA. Mt-DciA full-length (Mt-DciA_pET22b), and truncated variants Mt-DciA-NTD (Mt-DciA-NTD_pET22b), and Mt-DciA-CTD (Mt-DciA-CTD_pET22b), were expressed using the same protocol. Transformed bacterial cells were grown in a 2xTY medium supplemented with Ampicillin (50 µg/mL). Cells were grown to an OD600 ≈ 0.6 at 37 °C; then 0.5 mM IPTG was added to the culture, and protein expression was allowed to continue for 3 hours at 30 °C (RPM = 210), after which the cells were harvested by centrifugation at 4 °C and frozen at -80 °C.

Protein Biochemistry

Unless otherwise indicated, standard protein biochemistry techniques were used to purify all the proteins in this study (Supplementary Figure 8). All manipulations were carried out at 4 °C.

Unless otherwise indicated, 90 - 160 mls of cells expressing the protein of interest were lysed using a Sonic dismembrator (Model 500, Fisher Scientific) at the following settings: 3 min at 70% amplitude, with alternating 30s on and off cycles (Vc) and 15 min at 50% amplitude, with alternating cycles of 30s on and 60s off (Mt). The protein of interest was recovered in the soluble fraction by centrifugation (RPM=16,000, JA-17, Beckman-Coulter).

Vc-DnaB. Untagged Vc-DnaB was purified by combining ammonium sulfate (AS) precipitation and heparin, hydroxyapatite, and size exclusion chromatography. Vc-DnaB was found in the supernatant after making the soluble fraction 20% of saturated AS (SAS), but in the pellet when treated with 45% SAS. The 45% SAS

pellet was resuspended in heparin buffer A below and purified over a 50 mL Heparin Sepharose Fast Flow (Cytiva), with the following buffers: heparin buffer A: 20 mM Tris-HCl, pH = 7.4, 5 mM $MgCl_2$, 5% glycerol, 5 mM β-mercaptoethanol; Heparin buffer B: A + 1 M NaCl and a linear gradient from 0% to 40% B. Heparin-purified Vc-DnaB was purified by hydroxyapatite chromatography (65 ml, CHT, Bio-Rad) in the following buffers: A: 5mM potassium phosphate, pH = 7.5, 100 mM NaCl, 5 mM $MgCl_2$, 5% glycerol, 5 mM β-mercaptoethanol; B: A + 250 mM potassium phosphate, pH = 7.5). CHT-purified Vc-DnaB was concentrated by 45% AS precipitation, redissolved in 6 mL of 20 mM potassium HEPES, pH=7.5, 500 mM NaCl, 5 mM $MgCl_2$, 5% glycerol, 5 mM β-mercaptoethanol), and applied to a 320mL Superdex200 Prep Grade (Cytiva) column equilibrated in the above buffer. Size exclusion chromatography fractions free of nuclease activity were pooled, concentrated (Corning, 20 ml, 10 kDa molecular weight cutoff) to 55 mg/ml, aliquoted (~10-20 µl aliquots), flash frozen in liquid nitrogen, and maintained at -80 °C until use.

Vc-DnaB-NHis and Vc-DnaB-E259A-NHis were purified using the protocol employed with untagged Vc-DnaB but with discrete changes. The 45% SAS pellet was resuspended in Ni^{2+}-nitrilotriacetic acid (NiNTA) Buffer A (20 mM Tris-HCl, pH = 7.4, 50 mM NaCl, 5 mM $MgCl_2$, 5% glycerol, 5 mM β-mercaptoethanol) and incubated with 15 mL of NiNTA agarose beads (Qiagen) according to the manufacturer's instructions. The beads were washed with 180 mL of NiNTA Buffer B (20 mM Tris-HCl, pH=7.4, 50 mM NaCl, 5 mM $MgCl_2$, 5% glycerol, 5 mM β-mercaptoethanol, 30 mM imidazole pH 8); Vc-DnaB-NHis and was eluted from the

beads with 300 mL of NiNTA Buffer C (20 mM Tris-HCl pH=7.4, 50 mM NaCl, 5 mM $MgCl_2$, 5% glycerol, 5 mM β-mercaptoethanol, 250 mM imidazole, pH = 8). NiNTA-purified Vc-DnaB-NHis was further purified over Heparin Sepharose Fast Flow as was done with untagged DnaB except that the elution gradient was modified; 4 column volumes of Heparin buffer A (above), followed by a linear gradient from 5% to 100% Heparin buffer B over six column volumes. Vc-DnaB-NHis fractions were recovered and pooled in the ~80 mM to ~600 mM NaCl positions on the gradient. The heparin pool was passed through a 23 mL SP Sepharose Fast Flow (Cytiva) equilibrated in Q buffer A: 20 mM Tris-HCl, pH=7.4, 100 mM NaCl, 5 mM $MgCl_2$, 5% glycerol, and 5 mM β-mercaptoethanol; Vc-DnaB-NHis was captured by a 50mL Q Sepharose Fast Flow column (Cytiva) attached in-line. After a 4-column volume wash with 10% Q buffer B: (20 mM Tris-HCl, pH = 7.4, 1 M NaCl, 5 mM $MgCl_2$, 5% glycerol, and 5 mM β-mercaptoethanol), a linear gradient from 10% to 100% Q buffer B was used to elute Vc-DnaB-NHis, which was recovered in the ~250 mM to ~800 mM NaCl positions on the gradient. The pooled Vc-DnaB-NHis containing fractions were further purified CHT and Superdex200 Prep grade (Cytiva) as described above. Size exclusion chromatography fractions were pooled, concentrated as described above, to 40 mg/ml, aliquoted (~15-30 µL aliquots), flash frozen in liquid nitrogen, and maintained at -80 °C until use.

Vc-DciA. Vc-DciA-FL-CHis, Vc-DciA-NTD-CHis, and Vc-DciA-CTD-CHis were purified using nearly identical protocols. Cells were lysed as above, except that Protease Inhibitor Mini Tablet, EDTA-free (Pierce, ThermoFisher Scientific p/n

32955), was added to the Vc-DciA-CTD-CHis sample at a ratio of one tablet for every 10 mL of lysate. All three Vc-DciA constructs were recovered in the soluble fraction. Each fraction was applied to ~10 mL of Ni-NTA agarose beads, incubated for 40 min, and washed with 80 mL of NiNTA Buffer A (20 mM Tris-HCl, pH = 8, 300 mM NaCl, 5% glycerol, and 5 mM β-mercaptoethanol), supplemented with 15 mM imidazole, pH = 8 (Vc-DciA-NTD-CHis), or 30 mM imidazole, pH = 8 (Vc-DciA-FL-CHis and Vc-DciA-CTD-CHis). Vc-DciA constructs were eluted from the beads with NiNTA Buffer B (20 mM Tris-HCl, pH = 7.4, 50 mM NaCl, 5 mM $MgCl_2$, 5% glycerol, 5 mM β-mercaptoethanol, and 250mM imidazole, pH = 8). Further purification was achieved by flowing the various Vc-DciA constructs through a 50mL Q Sepharose Fast Flow column for capture on a 23mL SP Sepharose Fast Flow column attached in-line; both columns had been equilibrated in SP buffer A: (20mM Tris-HCl, pH = 7.4, 50 mM NaCl, 5% glycerol, and 5 mM β-mercapoethanol). After separating the two columns, weakly bound proteins were washed away with 4 columns volumes of 5% SP buffer B (20 mM Tris-HCl, pH = 7.4, 1 M NaCl, 5% glycerol, and 5 mM β-mercaptoethanol); this was followed by a linear gradient from 5% to 100% SP buffer B over 3 column volumes. Notably, we observed that Vc-DciA-FL-CHis eluted at the ~150 mM to ~350 mM NaCl position in the gradient, Vc-DciA-NTD-CHis between ~120mM and ~700mM NaCl, and Vc-DciA-CTD-CHis between ~180 mM and ~300 mM NaCl. Pooled fractions were concentrated (Vc-DciA-FL-CHis by 50% AS precipitation, Vc-DciA-NTD-CHis by 70% AS precipitation, and Vc-DciA-CTD-CHis using a 15 mL (2 kiloDalton molecular weight cutoff) spin concentrator (Sartorius Vivaspin). Each construct

was then chromatographed over a 320mL Superdex200 Prep Grade column, equilibrated in 20 mM potassium-HEPES, pH = 7.5, 300 mM NaCl, 5% glycerol, and 5 mM β-mercaptoethanol, and processed for -80° storage as described above.

Coexpressed Vc-DnaB-Vc-DciA. A soluble fraction derived from coexpressed Vc-DnaB-untagged - Vc-DciA-FL-Chis, prepared as described above, was submitted to NiNTA and size exclusion chromatography (320mL Superdex200 Prep Grade). The NiNTA chromatography was performed as above with the following buffers: NiNTA buffer A (20 mM Tris-HCl, pH = 7.4, 500 mM NaCl, 5 mM $MgCl_2$, 5% glycerol, 5 mM β-mercaptoethanol, and 30 mM imidazole, pH = 8) and NiNTA buffer B (20 mM Tris-HCl, pH = 7.4, 500 mM NaCl, 5 mM $MgCl_2$, 5% glycerol, 5 mM β-mercaptoethanol, and 250 mM imidazole, pH = 8). NiNTA-purified protein was concentrated by precipitation with 75% SAS and redissolved in 6 mL of the running buffer (below) for size exclusion chromatography. The size exclusion chromatography was carried out in (20 mM potassium HEPES, pH = 7.5, 500 mM NaCl, 5 mM $MgCl_2$, 5% glycerol, and 5 mM β-mercaptoethanol).

Mt-DnaB. Mt-DnaB-NHis-SUMO containing bacterial cell pellets were thawed and resuspended in Buffer A containing 20 mM Tris-HCl pH = 8, 500 mM NaCl, 5 mM $MgCl_2$, 0.1 mM ATP, 20 mM imidazole, and 5% glycerol, supplemented with a protease inhibitor cocktail (ThermoScientific p/n 78439) at a volume ratio of 100 µL per 40 mL of lysis buffer. The resuspended cells were disrupted by sonication as described above. The soluble fraction from this procedure was incubated in NiNTA beads equilibrated in Mt-DnaB buffer A for 90 min. A 10-column-volume wash of buffer A supplemented with 80 mM imidazole was followed by treatment

of buffer A containing 250 mM imidazole to elute *Mt-DnaB*-NHis-SUMO. Subsequent incubation (60 min, 22 °C) with 2 mM DTT and the SUMO protease ScUlp1 at a 1:250 protease:substrate molar ratio released Mt-DnaB-WT. The preparation was completed by concentrating the sample to 5 mL followed by chromatography over a HiLoad 16/600 Superdex 200 prep grade column equilibrated in 20 mM Tris-HCl pH = 8, 500 mM NaCl, 5 mM $MgCl_2$, and 5% glycerol. Fractions containing *Mt-DnaB*-WT were pooled, concentrated up to 1 mg/mL, frozen, and stored at -80 °C. *Mt-DnaB* point mutants Walker A (K232A) and Walker B (E257A) were prepared in an identical manner as for the wild-type sequence.

Bacterial cell lysates with overexpressed truncated Mt-DnaB constructs (1-170, 1-278, 171-457, 279-457) were used in pull-down experiments but not purified.

Mt-DciA. Full-length (1-189) Mt-DciA were purified using a combination of NiNTA and size exclusion chromatography as described above. Fractions containing the various *Mt-DciA* constructs were pooled, concentrated, frozen, and stored at -80 °C. Bacterial cell lysates with overexpressed truncated Mt-DciA constructs (1-89 and 90-189) were purified, exploiting the same approach as the full-length construct.

NiNTA pull-downs (Vc proteins)

Equal volumes (22.5 mL) of cells at similar densities expressing untagged Vc-DnaB (full-length, NTD, NTD-LH, or LH-CTD, each in 20mM Tris-HCl pH 7.4, 500mM NaCl, 5mM $MgCl_2$, 10% sucrose, 5mM β-mercaptoethanol) and his-tagged Vc-DciA (full-length, Lasso, or KH, each in 20 mM Tris-HCl pH 8, 300 mM NaCl,

5% glycerol, 5 mM β-mercapoethanol), were mixed, diluted with 15mL of buffer (20mM Tris-HCl pH 8, 300mM NaCl, 5% glycerol 5 mM β-mercapoethanol) were mixed to a total volume of 60 mL. The mixture was lysed using a Sonic dismembrator (Model 500, Fisher Scientific) at the following settings: 2 min at 70% amplitude, with alternating 30s on and off cycles. Sonication settings were: 30s on, 30s off, 2 min total on time, 70% amplitude. The lysate was centrifuged at 16k RPM in a JA-17 rotor (Beckman-Coulter), and a supernatant was recovered.

The clarified lysate was incubated with Ni-NTA Agarose beads for 40 mins, washed with 90mL of NiNTA Buffer A (20 mM Tris-HCl pH 8, 300 mM NaCl, 5% glycerol, 5 mM β-mercaptoethanol, 15 mM Imidazole pH 8). Protein was eluted using 30 mL of NiNTA Buffer B (20 mM Tris-HCl pH 8, 300 mM NaCl, 5% glycerol, 5 mM β-mercaptoethanol, 250 mM Imidazole pH 8).

NiNTA pull-downs (Mt proteins)

A C-terminal 6xHis-tag Mt-DciA construct was used as bait, and one untagged Mt-DnaB construct was used as prey. The same protocol was exploited for every combination reported. Two bacterial pellets, independently expressing DciA and DnaB, harvested from 500 mL of bacterial cultures were thawed and mixed in Buffer A containing 20 mM Tris-HCl pH = 8, 300 mM NaCl, 5 mM MgCl2, 5% glycerol. Cells were disrupted by sonication (total: 10 min with On/Off cycles of 30”/60″). The lysate was clarified at 14,000g for 45 min at 4 °C, and the supernatant was incubated with Ni-NTA beads, previously equilibrated with Buffer A for 60 minutes, while shaking. Following the incubation, the beads were washed with 10 column volumes of Buffer A supplemented with 15 mM imidazole. Bound

1 proteins were then eluted with Buffer A containing 250 mM imidazole. The
2 collected protein fractions were analyzed using SDS-PAGE.
3

Supplementary Tables

Supplementary Table 1: Cryogenic Electron Microscopy Data Measurement and PDB Model Refinement

PDB	9DLS
EMDB	EMD-46984
Data Collection and Processing	
Microscope	Titan Krios
Voltage (kV)	300
Camera	Gatan K3
Magnification	81000
Defocus range (μm)	-3.7 – 6.8
Exposure time (ms)	2000
Electron dose (e^-/Å^2)	51.37
Number of frames collected (no.)	40
Number of frames processed (no.)	40
Calibrated pixel size (Å)	0.5413
Micrographs (no.)	12265
Total particle images (no.)	4315534
Refinement	
Particle per class (no.)	551305
Symmetry imposed	C1
Map resolution (Å), FSC = 0.143	3.37
Map sharpening B-factor (Å^2)	115.8
Map versus Model cross-correlation	0.7517
Model Composition	
Non-hydrogen atoms	21051
Protein residues	2648
Nucleotide residues	11
Ligand: ATPγS	6
Ligand: Mg^{2+}	6
Model Refinement	
Resolution limit (Å)	3.37
Number of chains	14
Number of residues	2648
B factors (Å^2)	
Protein	73.05
Nucleotide	51.57
Ligand (ATPγS)	53.07
RMS deviations	

Bond lengths (Å)	0.004
Bond angles (°)	0.482
Validation	
MolProbity score	1.66
Clashscore	5.63
Rotamer outliers (%)	2.09
Ramachandran plot (%)	
Favored (%)	97.42
Allowed (%)	2.58
Outliers (%)	0.00

1 **Supplementary Table 2. Contacts (<4 Å) in the Vc-DnaB-ssDNA complex.**

Model1	Chain1	Res1	ResN1	Atom1	to	Model2	Chain2	Res2	ResN2	Atom2	Dist
Vc-B-ssDNA	B	THR	355	OG1	to	Vc-B-ssDNA	G	DC	9	O2	3.947
Vc-B-ssDNA	B	ASN	383	OD1	to	Vc-B-ssDNA	G	DC	11	C5'	3.716
Vc-B-ssDNA	B	ASN	383	ND2	to	Vc-B-ssDNA	G	DC	11	O5'	3.771
Vc-B-ssDNA	B	ASN	383	OD1	to	Vc-B-ssDNA	G	DC	11	O5'	3.727
Vc-B-ssDNA	B	ASN	383	CG	to	Vc-B-ssDNA	G	DC	11	OP1	3.107
Vc-B-ssDNA	B	ASN	383	ND2	to	Vc-B-ssDNA	G	DC	11	OP1	2.651
Vc-B-ssDNA	B	ASN	383	OD1	to	Vc-B-ssDNA	G	DC	11	OP1	2.814
Vc-B-ssDNA	B	ASN	383	ND2	to	Vc-B-ssDNA	G	DC	11	OP2	3.263
Vc-B-ssDNA	B	ASN	383	CG	to	Vc-B-ssDNA	G	DC	11	P	3.922
Vc-B-ssDNA	B	ASN	383	ND2	to	Vc-B-ssDNA	G	DC	11	P	3.259
Vc-B-ssDNA	B	ASN	383	OD1	to	Vc-B-ssDNA	G	DC	11	P	3.784
Vc-B-ssDNA	B	ASN	383	CA	to	Vc-B-ssDNA	G	DA	12	OP2	3.423
Vc-B-ssDNA	B	ASN	383	CB	to	Vc-B-ssDNA	G	DA	12	OP2	3.404
Vc-B-ssDNA	B	ASN	383	CG	to	Vc-B-ssDNA	G	DA	12	OP2	3.126
Vc-B-ssDNA	B	ASN	383	OD1	to	Vc-B-ssDNA	G	DA	12	OP2	2.483
Vc-B-ssDNA	B	ASN	383	OD1	to	Vc-B-ssDNA	G	DA	12	P	3.825
Vc-B-ssDNA	B	ARG	400	CA	to	Vc-B-ssDNA	G	DC	11	OP1	3.351
Vc-B-ssDNA	B	ARG	400	CD	to	Vc-B-ssDNA	G	DA	12	OP2	3.746
Vc-B-ssDNA	B	ARG	400	NH1	to	Vc-B-ssDNA	G	DA	12	OP2	3.77
Vc-B-ssDNA	B	GLU	401	CA	to	Vc-B-ssDNA	G	DA	10	C4'	3.997
Vc-B-ssDNA	B	GLU	401	CA	to	Vc-B-ssDNA	G	DA	10	C5'	3.812
Vc-B-ssDNA	B	GLU	401	CA	to	Vc-B-ssDNA	G	DA	10	O3'	3.636
Vc-B-ssDNA	B	GLY	403	CA	to	Vc-B-ssDNA	G	DA	10	OP1	3.887
Vc-B-ssDNA	C	THR	355	OG1	to	Vc-B-ssDNA	G	DA	8	C5'	3.886
Vc-B-ssDNA	C	ASN	383	ND2	to	Vc-B-ssDNA	G	DC	9	O5'	3.47
Vc-B-ssDNA	C	ASN	383	CG	to	Vc-B-ssDNA	G	DC	9	OP1	3.534
Vc-B-ssDNA	C	ASN	383	ND2	to	Vc-B-ssDNA	G	DC	9	OP1	3.136
Vc-B-ssDNA	C	ASN	383	OD1	to	Vc-B-ssDNA	G	DC	9	OP1	3.236
Vc-B-ssDNA	C	ASN	383	ND2	to	Vc-B-ssDNA	G	DC	9	OP2	2.885
Vc-B-ssDNA	C	ASN	383	ND2	to	Vc-B-ssDNA	G	DC	9	P	3.222
Vc-B-ssDNA	C	ARG	384	NH2	to	Vc-B-ssDNA	G	DA	10	O3'	3.553
Vc-B-ssDNA	C	ARG	384	NH2	to	Vc-B-ssDNA	G	DA	10	O5'	3.969
Vc-B-ssDNA	C	ARG	384	CB	to	Vc-B-ssDNA	G	DA	10	OP2	3.621
Vc-B-ssDNA	C	ARG	384	NH2	to	Vc-B-ssDNA	G	DC	11	OP1	3.334
Vc-B-ssDNA	C	ARG	384	NH2	to	Vc-B-ssDNA	G	DC	11	OP2	3.229
Vc-B-ssDNA	C	ARG	384	NH2	to	Vc-B-ssDNA	G	DC	11	P	3.476
Vc-B-ssDNA	C	ARG	400	NH2	to	Vc-B-ssDNA	G	DC	9	O3'	3.991
Vc-B-ssDNA	C	ARG	400	CA	to	Vc-B-ssDNA	G	DC	9	OP1	3.163
Vc-B-ssDNA	C	ARG	400	CB	to	Vc-B-ssDNA	G	DC	9	OP1	3.945
Vc-B-ssDNA	C	GLU	401	CA	to	Vc-B-ssDNA	G	DA	8	O3'	3.771

Vc-B-ssDNA	C	GLU	401	CA	to	Vc-B-ssDNA	G	DC	9	OP1	3.548
Vc-B-ssDNA	C	GLY	403	CA	to	Vc-B-ssDNA	G	DA	8	OP1	3.765
Vc-B-ssDNA	D	ASN	353	CG	to	Vc-B-ssDNA	G	DG	5	N2	3.974
Vc-B-ssDNA	D	ASN	353	OD1	to	Vc-B-ssDNA	G	DG	5	N2	3.119
Vc-B-ssDNA	D	ASN	383	ND2	to	Vc-B-ssDNA	G	DT	7	O5'	3.535
Vc-B-ssDNA	D	ASN	383	CG	to	Vc-B-ssDNA	G	DT	7	OP1	3.881
Vc-B-ssDNA	D	ASN	383	ND2	to	Vc-B-ssDNA	G	DT	7	OP1	3.317
Vc-B-ssDNA	D	ASN	383	ND2	to	Vc-B-ssDNA	G	DT	7	OP2	2.826
Vc-B-ssDNA	D	ASN	383	OD1	to	Vc-B-ssDNA	G	DA	8	OP2	3.144
Vc-B-ssDNA	D	ASN	383	ND2	to	Vc-B-ssDNA	G	DT	7	P	3.287
Vc-B-ssDNA	D	ARG	384	NH1	to	Vc-B-ssDNA	G	DC	9	OP1	3.975
Vc-B-ssDNA	D	ARG	384	CB	to	Vc-B-ssDNA	G	DA	8	OP2	3.817
Vc-B-ssDNA	D	ARG	384	NH1	to	Vc-B-ssDNA	G	DC	9	OP2	3.673
Vc-B-ssDNA	D	ARG	400	CA	to	Vc-B-ssDNA	G	DT	7	OP1	3.31
Vc-B-ssDNA	D	ARG	400	NH1	to	Vc-B-ssDNA	G	DA	8	OP1	3.523
Vc-B-ssDNA	D	ARG	400	NH1	to	Vc-B-ssDNA	G	DA	8	OP2	3.988
Vc-B-ssDNA	D	GLU	401	CA	to	Vc-B-ssDNA	G	DA	6	C5'	3.914
Vc-B-ssDNA	D	GLU	401	CA	to	Vc-B-ssDNA	G	DA	6	O3'	3.561
Vc-B-ssDNA	D	GLU	401	CG	to	Vc-B-ssDNA	G	DA	6	O3'	3.774
Vc-B-ssDNA	D	GLU	401	CA	to	Vc-B-ssDNA	G	DT	7	OP1	3.923
Vc-B-ssDNA	D	GLY	403	CA	to	Vc-B-ssDNA	G	DA	6	OP1	3.815
Vc-B-ssDNA	E	THR	355	OG1	to	Vc-B-ssDNA	G	DA	4	C5'	3.779
Vc-B-ssDNA	E	THR	355	OG1	to	Vc-B-ssDNA	G	DC	3	O2	3.494
Vc-B-ssDNA	E	THR	355	OG1	to	Vc-B-ssDNA	G	DA	4	O4'	3.947
Vc-B-ssDNA	E	ASN	383	OD1	to	Vc-B-ssDNA	G	DG	5	C3'	3.914
Vc-B-ssDNA	E	ASN	383	CG	to	Vc-B-ssDNA	G	DG	5	O5'	3.967
Vc-B-ssDNA	E	ASN	383	ND2	to	Vc-B-ssDNA	G	DG	5	O5'	3.376
Vc-B-ssDNA	E	ASN	383	CG	to	Vc-B-ssDNA	G	DG	5	OP1	3.957
Vc-B-ssDNA	E	ASN	383	ND2	to	Vc-B-ssDNA	G	DG	5	OP1	3.414
Vc-B-ssDNA	E	ASN	383	CG	to	Vc-B-ssDNA	G	DG	5	OP2	3.968
Vc-B-ssDNA	E	ASN	383	ND2	to	Vc-B-ssDNA	G	DG	5	OP2	2.769
Vc-B-ssDNA	E	ASN	383	OD1	to	Vc-B-ssDNA	G	DA	6	OP2	3.377
Vc-B-ssDNA	E	ASN	383	ND2	to	Vc-B-ssDNA	G	DG	5	P	3.268
Vc-B-ssDNA	E	ARG	384	CB	to	Vc-B-ssDNA	G	DA	6	OP2	3.604
Vc-B-ssDNA	E	ARG	384	NH2	to	Vc-B-ssDNA	G	DT	7	OP2	3.483
Vc-B-ssDNA	E	ARG	400	CA	to	Vc-B-ssDNA	G	DG	5	OP1	3.17
Vc-B-ssDNA	E	ARG	400	CB	to	Vc-B-ssDNA	G	DG	5	OP1	3.856
Vc-B-ssDNA	E	GLU	401	CA	to	Vc-B-ssDNA	G	DA	4	C4'	3.884
Vc-B-ssDNA	E	GLU	401	CA	to	Vc-B-ssDNA	G	DA	4	C5'	3.87
Vc-B-ssDNA	E	GLU	401	CA	to	Vc-B-ssDNA	G	DA	4	O3'	3.897
Vc-B-ssDNA	E	GLY	403	CA	to	Vc-B-ssDNA	G	DA	4	OP1	3.625
Vc-B-ssDNA	F	THR	355	OG1	to	Vc-B-ssDNA	G	DC	2	C5'	3.719

Vc-B-ssDNA	F	THR	355	OG1	to	Vc-B-ssDNA	G	DT	1	O4'	3.647
Vc-B-ssDNA	F	ASN	383	CG	to	Vc-B-ssDNA	G	DC	3	O5'	3.901
Vc-B-ssDNA	F	ASN	383	ND2	to	Vc-B-ssDNA	G	DC	3	O5'	3.271
Vc-B-ssDNA	F	ASN	383	CG	to	Vc-B-ssDNA	G	DC	3	OP1	3.928
Vc-B-ssDNA	F	ASN	383	ND2	to	Vc-B-ssDNA	G	DC	3	OP1	3.269
Vc-B-ssDNA	F	ASN	383	ND2	to	Vc-B-ssDNA	G	DC	3	OP2	3.048
Vc-B-ssDNA	F	ASN	383	OD1	to	Vc-B-ssDNA	G	DA	4	OP2	3.653
Vc-B-ssDNA	F	ASN	383	ND2	to	Vc-B-ssDNA	G	DC	3	P	3.276
Vc-B-ssDNA	F	ARG	384	NH2	to	Vc-B-ssDNA	G	DA	4	C3'	3.931
Vc-B-ssDNA	F	ARG	384	NH2	to	Vc-B-ssDNA	G	DG	5	OP1	3.545
Vc-B-ssDNA	F	ARG	384	CB	to	Vc-B-ssDNA	G	DA	4	OP2	3.528
Vc-B-ssDNA	F	ARG	384	NH2	to	Vc-B-ssDNA	G	DG	5	OP2	3.591
Vc-B-ssDNA	F	ARG	384	NH2	to	Vc-B-ssDNA	G	DG	5	P	3.861
Vc-B-ssDNA	F	ARG	400	CA	to	Vc-B-ssDNA	G	DC	3	OP1	3.216
Vc-B-ssDNA	F	ARG	400	CB	to	Vc-B-ssDNA	G	DC	3	OP1	3.778
Vc-B-ssDNA	F	GLU	401	CA	to	Vc-B-ssDNA	G	DC	2	C4'	3.918
Vc-B-ssDNA	F	GLU	401	CG	to	Vc-B-ssDNA	G	DC	2	C4'	3.794
Vc-B-ssDNA	F	GLU	401	CA	to	Vc-B-ssDNA	G	DC	2	C5'	3.855
Vc-B-ssDNA	F	GLU	401	OE2	to	Vc-B-ssDNA	G	DC	3	C5'	3.76
Vc-B-ssDNA	F	GLU	401	CG	to	Vc-B-ssDNA	G	DC	2	O3'	3.81

1

1 **Supplementary Table 3. Expression Plasmids Used in This Study**

ExpressionPlasmid	Insert	Template	Primers	Plasmid vector
pNG066-pET24a-VcDnaB-unt	VcDnaB-untagged	*V. cholerae* N16961 genomic DNA	VcDnaB-NdeI-F, VcDnaB-XhoI-R	pET24a
pNG067-pET24a-VcDnaB-NHis	VcDnaB-NHis	pNG066	VcDnaB-pET24a-NHis-F, VcDnaB-pET24a-NHis-R	pET24a
pNG072-pET24a-VcDnaB-E259A-NHis	VcDnaB-E259A-NHis	pNG067	VcDnaB-E259A-F, VcDnaB-E259A-R	pET24a
pNG114-pET24a-VcDnaB-1to170-unt	VcDnaB-NTD-untagged	pNG066	VcDnaB_170-pET24a-F, VcDnaB_170-pET24a-R	pET24a
pNG131-pET24a-VcDnaB-1to208-unt	VcDnaB-NTD_LH-untagged	pNG066	VcDnaB_208-pET24a-F, VcDnaB_208-pET24a-R	pET24a
pNG134-pET24a-VcDnaB-170to468-unt	VcDnaB-LH_CTD-untagged	pNG066	pET24a-VcDnaB_170-F, pET24a-VcDnaB_170-R	pET24a
pNG057-pCDFDuet-1-VcDciA-CHis	VcDciA-CHis	*V. cholerae* N16961 genomic DNA	VcDciA-NdeI-F, VcDciA-XhoI-CHis-R	pCDFDuet-1
pNG078-pCDFDuet-VcDciA-1to98-CHis	VcDciA-NTD-CHis	pNG057	VcDciA_98-CHis_pCDF-F, VcDciA_98-CHis_pCDF-R	pCDFDuet-1
pNG087-pCDFDuet-VcDciA-98to157-CHis	VcDciA-CTD-CHis	pNG057	VcDciA_1-VcDciA_98-F, VcDciA_1-VcDciA_98-R	pCDFDuet-1
MtDciA_pET22b	MtDciA-FL-CHis	n/a, synthesized	n/a, synthesized	pET22b
MtDciA-NTD_pET22b (1-89)	MtDciA-NTD-CHis	n/a, synthesized	n/a, synthesized	pET22b
MtDciA-CTD_pET22b (90-189)	MtDciA-CTD-CHis	n/a, synthesized	n/a, synthesized	pET22b
MtDnaB-SUMO_pET28a	MtDnaB-untagged	n/a, synthesized	n/a, synthesized	pET28a
MtDnaB-SUMO_pET28a	MtDnaB-SUMO	n/a, synthesized	n/a, c synthesized	pET28a
MtDnaB-SUMO-E257A_pET28a	MtDnaB-E257A-untagged	n/a, synthesized	n/a, synthesized	pET28a
MtDnaB-SUMO-K232A_pET28a	MtDnaB-K232A-untagged	n/a, synthesized	n/a, synthesized	pET28a
MtDnaB-NTD_pCDF-DUET-1 (1-170)	MtDnaB-NTD_pCDF-DUET-1	n/a, synthesized	n/a, synthesized	pCDF-DUET-1
MtDnaB-NTD-LH_pCDF-DUET-1 (1-278)	MtDnaB-NTD-LH-untagged	n/a, synthesized	n/a, synthesized	pCDF-DUET-1
MtDnaB-LH-CTD_pCDF-DUET-1 (171-457)	MtDnaB-LH-CTD-untagged	n/a, synthesized	n/a, synthesized	pCDF-DUET-1
MtDnaB-CTD_pCDF-DUET-1 (279-457)	MtDnaB-CTD-untagged	n/a, synthesized	n/a, synthesized	pCDF-DUET-1
MtDnaB-WT_pET16b	MtDnaB-WT	n/a, synthesized	n/a, synthesized	pET16b

2
3

1 ## Supplementary Table 4. Primers and other DNAs Used in This Study

DNA Name	DNA Sequence (5' to 3')
VcDnaB-NdeI-F	GGGAGAGCATATGGCAGATCCACGTACTGATA
VcDnaB-XhoI-R	GGGAGAGCTCGAGTTACTCATCGTCAAATGCAGGT
VcDnaB-pET24a-NHis-F	CTTTAAGAAGGAGATATACATATGCATCACCATCACCATCACGCAGATCCACGTACTGATAATCG
VcDnaB-pET24a-NHis-R	CGATTATCAGTACGTGGATCTGCGTGATGGTGATGGTGATGCATATGTATATCTCCTTCTTAAAG
VcDnaB-E259A-F	GATCTTCTCGCTGGCGATGCCCGCCGAAC
VcDnaB-E259A-R	GTTCGGCGGGCATCGCCAGCGAGAAGATC
VcDnaB_170-pET24a-F	GCCGAAGCGCGTACCTAACTCGAGCACCAC
VcDnaB_170-pET24a-R	GTGGTGCTCGAGTTAGGTACGCGCTTCGGC
VcDnaB_208-pET24a-F	GAGTGAACACGGGCTTTTAACTCGAGCACCACC
VcDnaB_208-pET24a-R	GGTGGTGCTCGAGTTAAAAGCCCGTGTTCACTC
pET24a-VcDnaB_170-F	TAAGAAGGAGATATACATATGACCAGTGAAAATGAAGGCCCG
pET24a-VcDnaB_170-R	CGGGCCTTCATTTTCACTGGTCATATGTATATCTCCTTCTTA
VcDciA-NdeI-F	GGGAGAGCATATGCGTGATCACCGCCCTACC
VcDciA-XhoI-CHis-R	GGGAGAGCTCGAGTCAGTGATGGTGATGGTGATGATCGTCTTTCTGATTTGCTT
VcDciA_1-VcDciA_98-F	TAAGAAGGAGATATACATATGCCTGAGTTGTATCGGCAAAGC
VcDciA_1-VcDciA_98-R	GCTTTGCCGATACAACTCAGGCATATGTATATCTCCTTCTTA
VcDciA_98-CHis_pCDF-F	GAAGTGCGAGTCAATCCTCATCACCATCACCATCAC
VcDciA_98-CHis_pCDF-R	GTGATGGTGATGGTGATGAGGATTGACTCGCACTTC
FRET-DNA-fork-top-strand	/5Cy3/TACGTAACGAGCCTGCTTTTTTTTTTTTTTTTTTTTTTTTT
FRET-DNA-fork-bottom-strand	TTTTTTTTTTTTTTTTTTTTTTTTTTGCAGGCTCGTTACGTA/3BHQ_2/
FRET-DNA-fork-capture-oligo	GCAGGCTCGTTACGTA
895	TCCTTGTTATCCACAGGGCAGTTTTTTTTTTTTTTTTTTT

References

1. Parker, M. W., Botchan, M. R. & Berger, J. M. Mechanisms and regulation of DNA replication initiation in eukaryotes. *Crit Rev Biochem Mol* **52**, 1–41 (2017).

2. Burgers, P. M. J. & Kunkel, T. A. Eukaryotic DNA Replication Fork. *Annu Rev Biochem* **86**, 1–22 (2017).

3. Costa, A. & Diffley, J. F. X. The Initiation of Eukaryotic DNA Replication. *Annu Rev Biochem* **91**, 107–131 (2022).

4. O'Donnell, M., Langston, L. & Stillman, B. Principles and concepts of DNA replication in bacteria, archaea, and eukarya. *Cold Spring Harbor perspectives in biology* **5**, a010108–a010108 (2013).

5. Greci, M. D. & Bell, S. D. Archaeal DNA Replication. *Annu Rev Microbiol* **74**, 1–16 (2020).

6. Li, H., Yao, N. Y. & O'Donnell, M. E. Anatomy of a twin DNA replication factory. *Biochem Soc T* **48**, 2769–2778 (2020).

7. Wang, G. *et al.* The structure of a DnaB-family replicative helicase and its interactions with primase. *Nat Struct Mol Biol* **15**, 94–100 (2008).

8. Strycharska, M. S. *et al.* Nucleotide and Partner-Protein Control of Bacterial Replicative Helicase Structure and Function. *Mol. Cell* **52**, 844–854 (2013).

9. Bailey, S., Eliason, W. K. & Steitz, T. A. Structure of hexameric DnaB helicase and its complex with a domain of DnaG primase. *Science (New York, NY)* **318**, 459–463 (2007).

10. Itsathitphaisarn, O., Wing, R. A., Eliason, W. K., Wang, J. & Steitz, T. A. The Hexameric Helicase DnaB Adopts a Nonplanar Conformation during Translocation. *Cell* **151**, 267–277 (2012).

11. Cargemel, C. *et al.* Structural Insights of the DciA Helicase Loader in Its Relationship with DNA. *Int J Mol Sci* **24**, 1427 (2023).

12. Marsin, S. *et al.* Study of the DnaB:DciA interplay reveals insights into the primary mode of loading of the bacterial replicative helicase. *Nucleic Acids Res.* **49**, gkab463- (2021).

13. Cargemel, C. *et al.* The apo-form of the Vibrio cholerae replicative helicase DnaB is a labile and inactive planar trimer of dimers. *Febs Lett* (2022) doi:10.1002/1873-3468.14403.

14. Cargemel, C. *et al.* The LH-DH module of the bacterial replicative helicases is the common binding site for DciA and other helicase loaders. (2022) doi:10.1101/2022.07.08.499335.

15. Lo, Y.-H. *et al.* The crystal structure of a replicative hexameric helicase DnaC and its complex with single-stranded DNA. *Nucleic Acids Research* **37**, 804–814 (2009).

16. Liu, B., Eliason, W. K. & Steitz, T. A. Structure of a helicase-helicase loader complex reveals insights into the mechanism of bacterial primosome assembly. *Nature communications* **4**, 2495 (2013).

17. Bazin, A., Cherrier, M. V., Gutsche, I., Timmins, J. & Terradot, L. Structure and primase-mediated activation of a bacterial dodecameric replicative helicase. *Nucleic Acids Research* **43**, 8564–8576 (2015).

18. Nagata, K. *et al.* Crystal structure of the complex of the interaction domains of E. coli DnaB helicase and DnaC helicase loader: Structural basis implying a distortion-accumulation mechanism for the DnaB ring opening caused by DnaC binding. *Journal of biochemistry* **5**, a010108 (2019).

19. Arias-Palomo, E., Puri, N., Murray, V. L. O., Yan, Q. & Berger, J. M. Physical Basis for the Loading of a Bacterial Replicative Helicase onto DNA. *Mol Cell* **74**, 173-184.e4 (2019).

20. Arias-Palomo, E., O'Shea, V. L., Hood, I. V. & Berger, J. M. The Bacterial DnaC Helicase Loader Is a DnaB Ring Breaker. *Cell* **153**, 438–448 (2013).

21. O'Donnell, M. E. & Li, H. The ring-shaped hexameric helicases that function at DNA replication forks. *Nat. Struct. Mol. Biol.* **25**, 122–130 (2018).

22. Fernandez, A. J. & Berger, J. M. Mechanisms of hexameric helicases. *Crit Rev Biochem Mol* 1–19 (2021) doi:10.1080/10409238.2021.1954597.

23. Bleichert, F., Botchan, M. R. & Berger, J. M. Mechanisms for initiating cellular DNA replication. *Science* **355**, eaah6317 (2017).

24. Gao, Y. & Yang, W. Different mechanisms for translocation by monomeric and hexameric helicases. *Curr. Opin. Struct. Biol.* **61**, 25–32 (2020).

25. Spinks, R. R., Spenkelink, L. M., Dixon, N. E. & Oijen, A. M. van. Single-Molecule Insights Into the Dynamics of Replicative Helicases. *Frontiers Mol Biosci* **8**, 741718 (2021).

26. Perera, H. M., Behrmann, M. S., Hoang, J. M., Griffin, W. C. & Trakselis, M. A. Contacts and context that regulate DNA helicase unwinding and replisome progression. *Enzym.* **45**, 183–223 (2019).

27. Medagli, B. & Onesti, S. DNA Helicases and DNA Motor Proteins. *Adv. Exp. Med. Biol.* **767**, 75–95 (2012).

28. Hingorani, M. M. & Patel, S. S. Interactions of bacteriophage T7 DNA primase/helicase protein with single-stranded and double-stranded DNAs. *Biochemistry* **32**, 12478–12487 (1993).

29. Gao, Y. *et al.* Structures and operating principles of the replisome. *Science* **363**, eaav7003 (2019).

30. Kaguni, J. M. DnaA, DnaB, and DnaC. in 1–14 (Springer New York, 2014). doi:10.1007/978-1-4614-6436-5_142-1.

31. Learn, B. A., Um, S. J., Huang, L. & McMacken, R. Cryptic single-stranded-DNA binding activities of the phage lambda P and Escherichia coli DnaC replication initiation proteins facilitate the transfer of E. coli DnaB helicase onto DNA. *Proceedings of the National Academy of Sciences of the United States of America* **94**, 1154–1159 (1997).

32. Bailey, S. *et al.* Structural Analysis of Bacillus subtilis SPP1 Phage Helicase Loader Protein G39P*. *J Biol Chem* **278**, 15304–15312 (2003).

33. Seco, E. M. *et al.* Bacteriophage SPP1 DNA replication strategies promote viral and disable host replication in vitro. *Nucleic Acids Res* **41**, 1711–1721 (2013).

34. Velten, M. *et al.* A Two-Protein Strategy for the Functional Loading of a Cellular Replicative DNA Helicase. *Mol Cell* **11**, 1009–1020 (2003).

35. Jones, C. E., Mueser, T. C., Dudas, K. C., Kreuzer, K. N. & Nossal, N. G. Bacteriophage T4 gene 41 helicase and gene 59 helicase-loading protein: A versatile couple with roles in replication and recombination. *Proc. Natl. Acad. Sci.* **98**, 8312–8318 (2001).

36. Odegrip, R., Schoen, S., Haggård-Ljungquist, E., Park, K. & Chattoraj, D. K. The Interaction of Bacteriophage P2 B Protein with Escherichia coli DnaB Helicase. *J. Virol.* **74**, 4057–4063 (2000).

37. Brézellec, P., Vallet-Gely, I., Possoz, C., Quevillon-Cheruel, S. & Ferat, J.-L. DciA is an ancestral replicative helicase operator essential for bacterial replication initiation. *Nature communications* **7**, 13271 (2016).

38. Brézellec, P. *et al.* Domestication of lambda phage genes into a putative third type of Replicative Helicase Matchmaker. *Genome Biol Evol* **9**, evx111 (2017).

39. Marsin, S. *et al.* Study of the DnaB:DciA interplay reveals insights into the primary mode of loading of the bacterial replicative helicase. *Nucleic Acids Res* gkab463- (2021) doi:10.1093/nar/gkab463.

40. Blaine, H. C., Burke, J. T., Ravi, J. & Stallings, C. L. DciA Helicase Operators Exhibit Diversity across Bacterial Phyla. *J Bacteriol* **204**, e00163-22 (2022).

41. Blaine, H. C., Simmons, L. A. & Stallings, C. L. Diverse Mechanisms of Helicase Loading during DNA Replication Initiation in Bacteria. *J. Bacteriol.* **205**, e00487-22 (2023).

42. Ozaki, S., Wang, D., Wakasugi, Y., Itani, N. & Katayama, T. The Caulobacter crescentus DciA promotes chromosome replication through topological loading of the DnaB replicative helicase at replication forks. *Nucleic Acids Res.* **50**, gkac1146- (2022).

43. Chase, J., Berger, J. & Jeruzalmi, D. Convergent evolution in two bacterial replicative helicase loaders. *Trends Biochem Sci* **47**, 620–630 (2022).

44. Chase, J. *et al.* Mechanisms of opening and closing of the bacterial replicative helicase. *Elife* **7**, 1822 (2018).

45. Bell, S. P. & Kaguni, J. M. Helicase loading at chromosomal origins of replication. *Cold Spring Harbor perspectives in biology* **5**, a010124 (2013).

46. Ayora, S., Stasiak, A. & Alonso, J. C. The Bacillus subtilis bacteriophage SPP1 G39P delivers and activates the G40P DNA helicase upon interacting with the G38P-bound replication origin. *J. Mol. Biol.* **288**, 71–85 (1999).

47. Ioannou, C., Schaeffer, P. M., Dixon, N. E. & Soultanas, P. Helicase binding to DnaI exposes a cryptic DNA-binding site during helicase loading in Bacillus subtilis. *Nucleic Acids Res* **34**, 5247–5258 (2006).

48. Brown, D. *et al.* An Autoinhibited Conformation of the DnaB-Replicative Helicase – phage λP Loader Complex. *Biorxiv* 2022.12.30.522210 (2022) doi:10.1101/2022.12.30.522210.

49. AlphaFold-Protein-Structure-Database. Inhibitor_G39P domain-containing protein. https://alphafold.ebi.ac.uk/entry/A0A0M0X576.

50. Loscha, K. V. *et al.* A novel zinc-binding fold in the helicase interaction domain of the Bacillus subtilis DnaI helicase loader. *Nucleic Acids Research* **37**, 2395–2404 (2009).

51. Tsai, K.-L., Lo, Y.-H., Sun, Y.-J. & Hsiao, C.-D. Molecular interplay between the replicative helicase DnaC and its loader protein DnaI from Geobacillus kaustophilus. *Journal of Molecular Biology* **393**, 1056–1069 (2009).

52. AlphaFoldProteinStructureDatabase. Bacillus subtilis Primosomal protein DnaI. https://alphafold.ebi.ac.uk/entry/P06567.

53. Mueser, T. C., Jones, C. E., Nossal, N. G. & Hyde, C. C. Bacteriophage T4 gene 59 helicase assembly protein binds replication fork DNA. The 1.45 Å resolution crystal structure reveals a novel α-helical two-domain fold11Edited by P. E. Wright. *J. Mol. Biol.* **296**, 597–612 (2000).

54. Chan-Yao-Chong, M., Marsin, S., Quevillon-Cheruel, S., Durand, D. & Ha-Duong, T. Structural ensemble and biological activity of DciA intrinsically disordered region. *J Struct Biol* **212**, 107573 (2020).

55. O'Shea, V. L. & Berger, J. M. Loading strategies of ring-shaped nucleic acid translocases and helicases. *Current Opinion in Structural Biology* **25**, 16–24 (2014).

56. Davey, M. J. & O'Donnell, M. Replicative helicase loaders: ring breakers and ring makers. *Curr Biol* **13**, R594–R596 (2003).

57. Chao, M. C. *et al.* High-resolution definition of the Vibrio cholerae essential gene set with hidden Markov model–based analyses of transposon-insertion sequencing data. *Nucleic Acids Res.* **41**, 9033–9048 (2013).

58. Mann, K. M. *et al.* Rv0004 is a new essential member of the mycobacterial DNA replication machinery. *PLOS Genetics* **13**, e1007115 (2017).

59. Quevillon-Cheruel, S. *et al.* Dcia, the Bacterial Replicative Helicase Loader, is a DNA Condenser. (2024) doi:10.2139/ssrn.4880687.

60. Davey, M. J., Fang, L., McInerney, P., Georgescu, R. E. & O'Donnell, M. The DnaC helicase loader is a dual ATP/ADP switch protein. *The EMBO journal* **21**, 3148–3159 (2002).

61. Biswas, T. & Tsodikov, O. V. Hexameric ring structure of the N-terminal domain of Mycobacterium tuberculosis DnaB helicase. *The FEBS journal* **275**, 3064–3071 (2008).

62. Oakley, A. J. & Xu, Z. Q. E. coli DnaB bound to ssDNA and AMPPNP. (2022) doi:10.2210/pdb7t20/pdb.

63. Mesa, P., Alonso, J. C. & Ayora, S. Bacillus subtilis Bacteriophage SPP1 G40P Helicase Lacking the N-terminal Domain Unwinds DNA Bidirectionally. *J. Mol. Biol.* **357**, 1077–1088 (2006).

64. Reha-Krantz, L. J. & Hurwitz, J. The dnaB gene product of Escherichia coli. I. Purification, homogeneity, and physical properties. *J. Biol. Chem.* **253**, 4043–4050 (1978).

65. Yu, X., Jezewska, M. J., Bujalowski, W. & Egelman, E. H. The hexameric E. coli DnaB helicase can exist in different Quaternary states. *Journal of Molecular Biology* **259**, 7–14 (1996).

66. Bujalowski, W., Klonowska, M. M. & Jezewska, M. J. Oligomeric structure of Escherichia coli primary replicative helicase DnaB protein. *J. Biol. Chem.* **269**, 31350–31358 (2001).

67. Nakayama, N., Arai, N., Kaziro, Y. & Arai, K. Structural and functional studies of the dnaB protein using limited proteolysis. Characterization of domains for DNA-dependent ATP hydrolysis and for protein association in the primosome. *J. Biol. Chem.* **259**, 88–96 (1984).

68. Günther, E., Mikolajczyk, M. & Schuster, H. Stabilization by ATP and ADP of Escherichia coli dnaB protein activity. *J. Biol. Chem.* **256**, 11970–11973 (1981).

69. Kaplan, D. L. & Steitz, T. A. DnaB from Thermus aquaticus Unwinds Forked Duplex DNA with an Asymmetric Tail Length Dependence*. *J Biol Chem* **274**, 6889–6897 (1999).

70. Schlierf, M., Wang, G., Chen, X. S. & Ha, T. Hexameric helicase G40P unwinds DNA in single base pair steps. *eLife* **8**, e42001 (2019).

71. Notarnicola, S. M. & Richardson, C. C. The nucleotide binding site of the helicase/primase of bacteriophage T7. Interaction of mutant and wild-type proteins. *J. Biol. Chem.* **268**, 27198–27207 (1993).

72. Patel, S. S., Hingorani, M. M. & Ng, W. M. The K318A Mutant of Bacteriophage T7 DNA Primase-Helicase Protein Is Deficient in Helicase But Not Primase Activity and Inhibits Primase-Helicase Protein Wild-Type Activities by Heterooligomer Formation. *Biochemistry* **33**, 7857–7868 (1994).

73. Crampton, D. J., Mukherjee, S. & Richardson, C. C. DNA-induced switch from independent to sequential dTTP hydrolysis in the bacteriophage T7 DNA helicase. *Molecular Cell* **21**, 165–174 (2006).

74. Crampton, D. J., Guo, S., Johnson, D. E. & Richardson, C. C. The arginine finger of bacteriophage T7 gene 4 helicase: Role in energy coupling. *Proc. Natl. Acad. Sci.* **101**, 4373–4378 (2004).

75. Makowska-Grzyska, M. & Kaguni, J. M. Primase Directs the Release of DnaC from DnaB. *Mol Cell* **37**, 90–101 (2010).

76. Polissi, A., Goffin, L. & Georgopoulos, C. The Escherichia coli heat shock response and bacteriophage lambda development. *FEMS microbiology reviews* **17**, 159–169 (1995).

77. Zylicz, M. The Escherichia coli chaperones involved in DNA replicadon. *Philos. Trans. R. Soc. Lond. Ser. B: Biol. Sci.* **339**, 271–278 (1993).

78. Spinks, R. R. *et al.* DnaB helicase dynamics in bacterial DNA replication resolved by single-molecule studies. *Nucleic Acids Res* **49**, gkab493- (2021).

79. Green, M. R. & Sambrook, J. *Molecular Cloning: A Laboratory Manual*. (Cold Spring Harbor Laboratory Press, 2012).

80. Kelley, D. S. *et al.* Mycobacterial DnaB helicase intein as oxidative stress sensor. *Nat. Commun.* **9**, 4363 (2018).

81. Zhang, H., Zhang, Z., Yang, J. & He, Z. Functional characterization of DnaB helicase and its modulation by single-stranded DNA binding protein in Mycobacterium tuberculosis. *Febs J* **281**, 1256–1266 (2014).

82. Olinares, P. D. B. *et al.* Native Mass Spectrometry-Based Screening for Optimal Sample Preparation in Single-Particle Cryo-EM. *Structure* **29**, 186-195.e6 (2021).

83. Olinares, P. D. B. & Chait, B. T. The Eukaryotic RNA Exosome, Methods and Protocols. *Methods Mol. Biol.* **2062**, 357–382 (2019).

84. Marty, M. T. *et al.* Bayesian Deconvolution of Mass and Ion Mobility Spectra: From Binary Interactions to Polydisperse Ensembles. *Anal. Chem.* **87**, 4370–4376 (2015).

85. Reid, D. J. *et al.* MetaUniDec: High-Throughput Deconvolution of Native Mass Spectra. *J. Am. Soc. Mass Spectrom.* **30**, 118–127 (2019).

86. Lindsley, J. E. DNA Topoisomerase Protocols. *Methods Mol Biology Clifton N J* **95**, 57–64 (2000).

87. Kiianitsa, K., Solinger, J. A. & Heyer, W.-D. NADH-coupled microplate photometric assay for kinetic studies of ATP-hydrolyzing enzymes with low and high specific activities. *Analytical Biochemistry* **321**, 266–271 (2003).

88. Cheng, A. *et al.* Leginon: New features and applications. *Protein Sci.* **30**, 136–150 (2021).

89. Cheng, A. *et al.* Fully automated multi-grid cryoEM screening using Smart Leginon. *IUCrJ* **10**, 77–89 (2023).

90. Punjani, A., Rubinstein, J. L., Fleet, D. J. & Brubaker, M. A. cryoSPARC: algorithms for rapid unsupervised cryo-EM structure determination. *Nature Methods* **14**, 290–296 (2017).

91. Punjani, A., Zhang, H. & Fleet, D. J. Non-uniform refinement: adaptive regularization improves single-particle cryo-EM reconstruction. *Nat Methods* **17**, 1214–1221 (2020).

92. Punjani, A. & Fleet, D. J. 3D variability analysis: Resolving continuous flexibility and discrete heterogeneity from single particle cryo-EM. *J Struct Biol* **213**, 107702 (2021).

93. Punjani, A. & Fleet, D. J. 3DFlex: determining structure and motion of flexible proteins from cryo-EM. *Nat Methods* 1–11 (2023) doi:10.1038/s41592-023-01853-8.

94. Rubinstein, J. L. & Brubaker, M. A. Alignment of cryo-EM movies of individual particles by optimization of image translations. *J. Struct. Biol.* **192**, 188–195 (2015).

95. Stagg, S. M., Noble, A. J., Spilman, M. & Chapman, M. S. ResLog plots as an empirical metric of the quality of cryo-EM reconstructions. *J. Struct. Biol.* **185**, 418–426 (2014).

96. Zivanov, J., Nakane, T. & Scheres, S. H. W. Estimation of high-order aberrations and anisotropic magnification from cryo-EM data sets in RELION -3.1. *IUCrJ* **7**, 253–267 (2020).

97. Bell, J. M., Chen, M., Durmaz, T., Fluty, A. C. & Ludtke, S. J. New software tools in EMAN2 inspired by EMDatabank map challenge. *J. Struct. Biol.* **204**, 283–290 (2018).

98. Sanchez-Garcia, R. *et al.* DeepEMhancer: a deep learning solution for cryo-EM volume post-processing. *Commun Biology* **4**, 874 (2021).

99. Jamali, K. *et al.* Automated model building and protein identification in cryo-EM maps. *Nature* **628**, 450–457 (2024).

100. Emsley, P. & Cowtan, K. Coot: model-building tools for molecular graphics. *Acta crystallographica Section D, Biological crystallography* **60**, 2126–2132 (2004).

101. Brown, A. *et al.* Tools for macromolecular model building and refinement into electron cryo-microscopy reconstructions. *Acta crystallographica Section D, Biological crystallography* **71**, 136–153 (2015).

102. Liebschner, D. *et al.* Macromolecular structure determination using X-rays, neutrons and electrons: recent developments in Phenix. *Acta Crystallographica Section D: Structural Biology* **75**, 861–877 (2019).

103. Williams, C. J. *et al.* MolProbity: More and better reference data for improved all-atom structure validation. *Protein Sci.* **27**, 293–315 (2018).

104. Echols, N. *et al.* Automating crystallographic structure solution and refinement of protein-ligand complexes. *Acta crystallographica Section D, Biological crystallography* **70**, 144–154 (2014).

105. Zwart, P. H. *et al.* Automated structure solution with the PHENIX suite. *Methods in molecular biology (Clifton, NJ)* **426**, 419–435 (2008).

106. Afonine, P. V. *et al.* Real-space refinement in PHENIX for cryo-EM and crystallography. *Acta Crystallogr Sect D* **74**, 531–544 (2018).

107. Terwilliger, T. C. *et al.* Model morphing and sequence assignment after molecular replacement. *Acta Crystallogr. Sect. D: Biol. Crystallogr.* **69**, 2244–2250 (2013).

108. Afonine, P. V. *et al.* Towards automated crystallographic structure refinement with phenix.refine. *Acta crystallographica Section D, Biological crystallography* **68**, 352–367 (2012).

109. Adams, P. D. *et al.* PHENIX: a comprehensive Python-based system for macromolecular structure solution. *Acta crystallographica Section D, Biological crystallography* **66**, 213–221 (2010).

110. Winn, M. D. *et al.* Overview of the CCP4 suite and current developments. *Acta crystallographica Section D, Biological crystallography* **67**, 235–242 (2011).

111. Kleywegt, G., Zou, J., Kjeldgaard, M. & Jones, T. *International Tables for Crystallography, Vol. F, Edited by MG Rossmann & E. Arnold, Ch. 17.1, Pp. 353ą356, 366ą367*. (2001).

112. Sierk, M. & Kleywegt, G. Deja Vu All Over Again: Finding and Analyzing Protein Structure Similarities. *Structure (London, England : 1993)* **12**, 2103–2111 (2004).

113. Kleywegt, G. J. Quality control and validation. *Methods in molecular biology (Clifton, NJ)* **364**, 255–272 (2007).

114. Kleywegt, G. & Jones, T. Model building and refinement practice. *Macromolecular Crystallography, Pt A* **277**, 208–230 (1997).

115. Pettersen, E. F. *et al.* UCSF Chimera--a visualization system for exploratory research and analysis. *Journal of computational chemistry* **25**, 1605–1612 (2004).

116. LLC, S., ,. The PyMOL Molecular Graphics System, Version 2.1. (2017).

117. Luscombe, N. M., Laskowski, R. A. & Thornton, J. M. NUCPLOT: a program to generate schematic diagrams of protein-nucleic acid interactions. *Nucleic Acids Research* **25**, 4940–4945 (1997).

118. Morin, A. *et al.* Collaboration gets the most out of software. *eLife* **2**, e01456 (2013).

119. Núñez-Ramírez, R. *et al.* Loading a ring: structure of the Bacillus subtilis DnaB protein, a co-loader of the replicative helicase. *Journal of Molecular Biology* **367**, 764–769 (2007).

120. Oakley, A. J. & Xu, Z. Q. E. coli DnaB bound to ssDNA and ADP-AlF4. (2023) doi:10.2210/pdb7t21/pdb.

121. Oakley, A. J. & Xu, Z. Q. E. coli DnaB bound to three DnaG C-terminal domains, ssDNA, ADP and AlF4. (2023) doi:10.2210/pdb7t22/pdb.

122. Oakley, A. J. & Xu, Z. Q. E. coli DnaB bound to two DnaG C-terminal domains, ssDNA, ADP and AlF4. (2023) doi:10.2210/pdb7t23/pdb.

123. *DUF721 Domain-Containing Protein (Vc-DciA)*. https://alphafold.ebi.ac.uk/entry/A0A5C2AYF9 (2024).

124. UPF0232 protein Rv0004 (Mt-DciA). (2024).

125. Tartoff, K. D. & Hobbs, C. A. Improved Media for Growing Plasmid and Cosmid Clones. *Bethesda Research Laboratories Focus* **9**, 12 (1987).

126. Wood, W. N., Smith, K. D., Ream, J. A. & Lewis, L. K. Enhancing yields of low and single copy number plasmid DNAs from Escherichia coli cells. *J. Microbiol. Methods* **133**, 46–51 (2017).

127. Sambrook, J., Fritsch, E. F. & Maniatis, T. *Molecular Cloning*. (Cold Spring Harbor Laboratory Press, 1989).